FACULTY OF ENGINEERING
AND ARCHITECTURE

Experimental heat transfer measurements on supercritical R125 in a horizontal tube

Arthur De Meulemeester
Student number: 01307537

Supervisors: Prof. dr. ir. Michel De Paepe, Prof. dr. ir. Steven Lecompte
Counsellor: Jera Van Nieuwenhuyse

Master's dissertation submitted in order to obtain the academic degree of
Master of Science in Electromechanical Engineering

Academic year 2019-2020

GHENT
UNIVERSITY

FACULTY OF ENGINEERING
AND ARCHITECTURE

Experimental heat transfer measurements on supercritical R125 in a horizontal tube

Arthur De Meulemeester
Student number: 01307537

Supervisors: Prof. dr. ir. Michel De Paepe, Prof. dr. ir. Steven Lecompte
Counsellor: Jera Van Nieuwenhuyse

Master's dissertation submitted in order to obtain the academic degree of
Master of Science in Electromechanical Engineering

Academic year 2019-2020

GHENT
UNIVERSITY

Permission

June 2020

Addendum

Due to the outbreak of the coronavirus in the beginning of 2020, safety measures were taken by Ghent University that restricted lab access. Fortunately, some measurements could still be performed. However, these are limited in number and parameter ranges.

Preface

Making this master thesis has proven to be quite a learnful experience and would not have been possible without the following people.

I would like to thank my supervisor Jera Van Nieuwenhuyse and promotors prof. Steven Lecompte and prof. Michel De Paepe for the opportunity and guidance. Thanks for answering my questions, reading and correcting this text, helping figuring out practical issues of the setup and performing measurements in particular.

Finally, I would like to thank my family and friends for all the support and necessary distractions during this year.

Experimental heat transfer measurements on supercritical R125 in a horizontal tube

Arthur De Meulemeester

Supervisors: prof. dr. ir. Michel De Paepe, prof. dr. ir. Steven Lecompte
Counsellor: Jera Van Nieuwenhuyse

Master's dissertation submitted in order to obtain the academic degree of
Master of Science in Electromechanical Engineering

Departement of Electromechanical, Systems and Metal Engineering
Chair: prof. dr. ir. Michel De Paepe
Faculty of Engineering and Architecture
Ghent University
Academic year 2019–2020

Summary

This master thesis handles experimental heat transfer measurements on R125 at the supercritical state in a horizontal tube.

The introductory chapter explains why this research is needed and its main applications.

Chapter two provides an overview of the different supercritical heat transfer phenomena. The influences of different parameters are discussed, as well as various supercritical heat transfer correlations found in literature.

The third chapter describes the test setup used to perform the measurements. An overview of all components and measurement equipment is given.

Chapter four describes the used data reduction method and corresponding uncertainty analysis.

Chapter five handles the results obtained from the performed measurements. First, the proposed combinations of parameters and their deviations are discussed. Second, the accuracy and repeatability is checked. Third, the influences of the operating parameters are investigated. Fourth, a first attempt at correlation development is done. Finally, the experimental results are compared to existing correlations found in literature.

The next chapter, chapter six, proposes adaptations to the existing setup to make buoyancy effects measurable and to obtain more accurate results.

Finally, the closing chapter provides a summary of the research and discusses future work.

Keywords: R125, supercritical, heat transfer, convection, experimental

EXPERIMENTAL HEAT TRANSFER MEASUREMENTS ON SUPERCRITICAL R125 IN A HORIZONTAL TUBE

Arthur De Meulemeester, Jera Van Nieuwenhuyse, Steven Lecompte and Michel De Paepe
Department of Electromechanical, Systems and Metal Engineering
Ghent University
Sint-Pietersnieuwstraat 41, B9000 Gent, Belgium
E-mail: arthur.demeulemeester@ugent.be

ABSTRACT

Utilisation of renewable and low-grade heat sources have a large potential to reduce greenhouse gas emissions, an ever growing concern. These energy sources include industrial waste heat, geothermal energy, biomass combustion and solar energy. The organic Rankine cycle (ORC), capable of converting low-temperature heat to useful work, has proved to be a suitable technology for this purpose. Its efficiency can be increased by operating at supercritical conditions, replacing the evaporator with a supercritical vapour generator. However, knowledge of the heat transfer behaviour of refrigerants at the supercritical state is limited. As only few heat transfer correlations are found in literature, more research is needed. In this paper, experimental measurements on supercritical heat transfer to supercritical R125 flowing in a horizontal tube were performed under various operating conditions. The setup consists of a counterflow tube-in-tube heat exchanger with a total length of 4 m. R125 flows in the inner tube, the heating fluid in the annulus. At 11 locations along this test section, bulk refrigerant temperatures are measured to determine the heat transfer coefficients. Influences of pressure, mass flux and heat flux were studied. Pressure levels varied between 1.04 and 1.11$\cdot p_c$, mass fluxes between 320 and 600 kg/s/m^2 and heat fluxes between 8 and 21 kW/m^2. The influences of these parameters agreed with conclusions found in literature: higher heat transfer coefficients were measured at lower pressures, higher mass fluxes and lower heat fluxes. However, no peaks in heat transfer coefficients around the pseudocritical temperature as described in literature could be detected. Future work will adapt the measurement strategy to obtain more accurate results, broaden the operating range and test other low global warming potential (GWP) refrigerants.

NOMENCLATURE

c_p	$[J/kg/K]$	Specific heat capacity
d	$[m]$	Inner tube diameter
D	$[m]$	Outer tube diameter
G	$[kg/s/m^2]$	Mass flux
h	$[W/m^2/K]$	Convective heat transfer coefficient
L	$[m]$	Test section length
$\dot{m}$	$[kg/s]$	Mass flow rate
Nu	$[-]$	Nusselt number
p	$[Pa]$	Pressure
Pr	$[-]$	Prandtl number
$\dot{q}$	$[W/m^2]$	Heat flux
$\dot{Q}$	$[W]$	Heat transfer rate
Re	$[-]$	Reynolds number
T	$[°C]$	Temperature

Special characters

μ	$[kg/m/s]$	Dynamic viscosity
λ	$[W/m/K]$	Thermal conductivity
ρ	$[kg/m^3]$	Density

Subscripts

b	Bulk
c	Critical
hf	Heating fluid
i	Inner
in	Inlet
o	Outer
out	Outlet
pc	Pseudocritical
w	Wall
wf	Working fluid

INTRODUCTION

Supercritical operation of heat-to-power and heat-to-heat cycles can have a positive influence on the cycle efficiencies compared to subcritical ones [1]. In the case of an ORC, the refrigerant in pressurized to a supercritical pressure before heat addition, so the two-phase region is bypassed to get a so-called transcritical ORC. Designing the vapour generator of a transcritical ORC requires accurate knowledge of the supercritical heat transfer behaviour of the working fluid. Today, many correlations can be found for water and/or

CO_2. However, studies on supercritical heat transfer on refrigerants are often not found. This gap in knowledge causes oversized heat exchanger designs and consequently higher costs. This research attempts to further close this gap by performing supercritical heat transfer measurements to supercritical R125 flowing in a horizontal tube.

SUPERCRITICAL HEAT TRANSFER

Heat transfer to supercritical fluids has been studied in the past. These studies showed that this type of heat transfer is heavily influenced by the rapid changes in thermophysical properties of the fluid. This leads to unusual heat transfer behaviour around the pseudo-critical temperature T_{pc}, defined as the temperature where the specific heat capacity has a peak for a certain supercritical pressure [2]. Figure 1 shows variations of the specific heat capacity c_p, density ρ, thermal conductivity λ and dynamic viscosity μ of R125 at a pressure 5% above p_c. The vertical black lines represents the critical temperature T_c, the dotted lines T_{pc}. Unlike at subcritical pressures, no discontinuities can be seen.

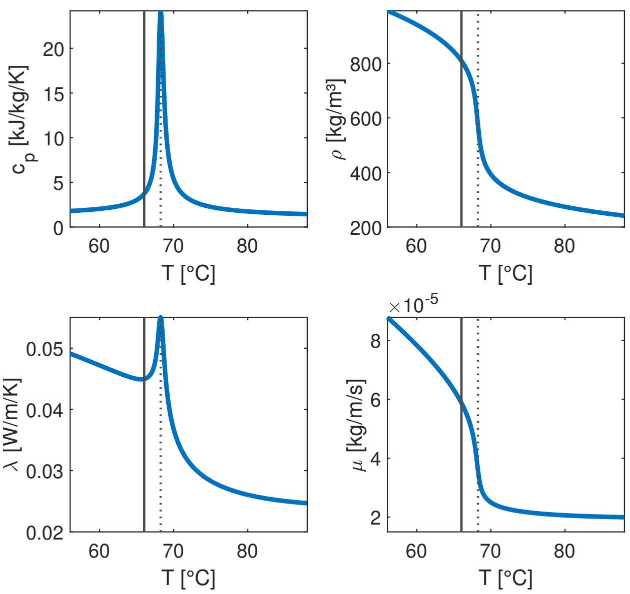

Figure 1: Thermophysical properties of R125 at supercritical conditions

Influences on heat transfer behaviour

Supercritical fluids flowing in a horizontal tube are subject to buoyancy effects due to rapid density variations in the fluid, see Figure 1. Hotter and thus less dense fluid will rise to the top of the tube while heavier colder fluid will remain at the bottom. This natural convection leads to variable wall temperatures around the tube circumference and decreases the heat transfer coefficient at the top while the heat transfer coefficient at the bottom increases. This buoyancy effect is present when low mass fluxes and/or high heat fluxes are used [3].

Apart from buoyancy effects, the pressure, mass flux and heat flux will influence the heat transfer behaviour. Higher convection coefficients are caused by decreased pressure, increased mass flux and decreased heat flux. In addition, the combination of thermophysical properties at and around T_{pc} causes peaks in convection coefficients at these temperatures.

Heat transfer correlations

Most supercritical heat transfer correlations found in literature are designed for water and/or CO_2 [4]. Some results are found for refrigerants, such as R134a [5, 6], R125 [7] and R410a and R404a [8]. In these works, the influences of pressure, mass flux and heat flux were investigated.

TEST SETUP DESCRIPTION

Setup overview

The test setup simulates the heat transfer of the vapour generator in a transcritical ORC. The expander, which is normally present in an ORC to extract work, is replaced by an expansion valve. The setup was designed by Lazova et al. [7]. A schematic overview of the setup can be seen in Figure 2. It consists of three main loops: the heating, working fluid and cooling loop.

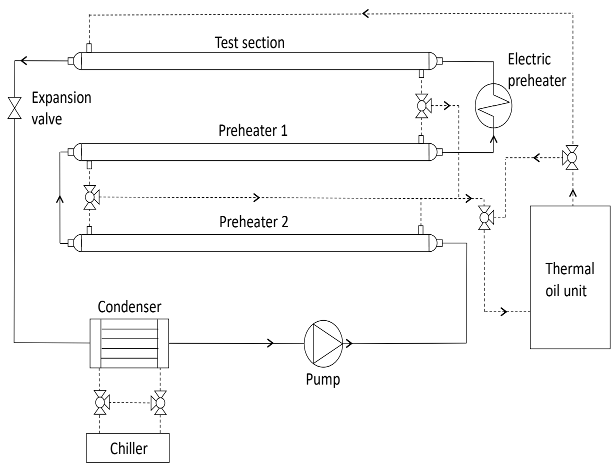

Figure 2: Schematic overview of test setup

The working fluid loop containing R125 is the main part of the setup. R125 (C_2HF_5) is an organic fluid with a critical pressure of 3.6 MPa and a critical temperature of 66°C, which makes it a suitable working fluid for low temperature waste heat recovery at the supercritical state. First, the working fluid is pressurized by the pump to a pressure above the critical pressure. The speed of the motor driving the pump is inverter controlled. After pressurization, the refrigerant is preheated using two tube-in-tube preheaters and a 10 kW electric in-line preheater. By using these preheaters the refrigerant can be conditioned to the right temperature at the test section inlet. The use of the tube-in-tube preheaters is optional so either no, one or two preheaters are used. The electric preheater allows for a PID controlled temperature of the refrigerant at the test section inlet. After preheating, the refrigerant enters the test section. Next, the refrigerant flows through an electronically controlled expansion valve. After expansion, the refrigerant passes the condenser, which is a plate heat exchanger. The condenser is connected to the cooling loop which acts as a heat sink.

The geometry and materials of the test section are shown in Table 1. It is a horizontal counterflow tube-in-tube heat exchanger with the refrigerant flowing in the inner tube and the heating fluid in the annulus. In the heating loop, Therminol ADX-10

Table 1: Test section specifications

	Length	4 m
Inner tube	Material	Copper
	λ_w	260 W/m/K
	d_i	0.02477 m
	d_o	0.02857 m
Outer tube	Material	Galvanised steel
	D_i	0.0530 m
	D_o	0.0603 m

thermal oil is used. After heating in the thermal oil unit it passes the test section and tube-in-tube preheaters. The thermal oil unit controls the oil temperature and has a heating capacity of 20 kW. The mass flow rate through the test section is controlled by a three way valve.

At the condenser, the refrigerant is cooled down by the cooling loop. It contains a mixture of water/glycol (70/30%) and is connected to a 900 l buffer vessel. This vessel is cooled by a 37 kW chiller unit located at the outside of the building. Just as in the heating loop, a three way valve allows for mass flow rate control through the condenser.

Test section measurement equipment

At the oil side of the test section, Pt100 temperature sensors are placed at inlet and outlet. In between, three K-type thermocouples are spaced evenly throughout the test section at distances of 1 m. Similarly, at the refrigerant side Pt100 sensors are placed at inlet and outlet. Between these, 11 T-type thermocouples are spaced evenly at distances of 0.33 m. In addition, pressure transducers are placed at inlet and outlet. Figure 3 shows a schematic overview of the test section including all temperature measurements. Red arrows indicate the thermal oil, blue arrows the refrigerant flow. During test measurements it became

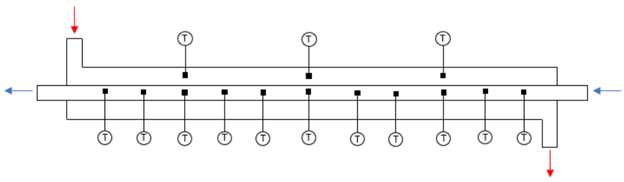

Figure 3: Test section thermocouple placements

clear that not all measurement equipment provided reliable results. The thermocouple measurements at the oil side of the test section proved to be unreliable. The opposite is true at the refrigerant side, where the Pt100 sensors did not function properly. In addition, four thermocouples at the refrigerant side of the test section could not be used. The measured temperatures by these thermocouples were too high, a possible explanation being that they were not located at the exact tube centre, but closer to the tube wall. While the malfunctioning measurement equipment described above did influence the control strategy and the data reduction method, reliable measurements could still be performed.

DATA REDUCTION METHOD AND UNCERTAINTY ANALYSIS

Data reduction method

Starting from the heat exchanger geometry and measured data, the convection coefficients at the refrigerant side can be determined. First, the heat transfer rate $\dot{Q}$ and heat flux $\dot{q}_{hf}$ in the test section is determined at the oil side.

$$\dot{Q} = \dot{m}_{hf} \cdot c_{p,hf} \cdot \Delta T_{hf} \tag{1}$$

$$\dot{q}_{hf} = \frac{\dot{Q}}{\pi \cdot d_o \cdot L} \tag{2}$$

As only oil temperatures at the inlet and outlet of the test section are known, the oil temperature profile is assumed to be linear. The consequence of this is the assumption of a constant heat flux over the test section. In addition, heat losses to the environment are neglected.

The outer wall temperature $T_{w,o}$ can be found as a function of the measured bulk oil temperature $T_{hf,b}$, heat flux $\dot{q}_{hf}$ and oil side convection coefficient h_{hf}, determined using the Dittus-Boelter correlation [9].

$$T_{w,o} = T_{hf,b} - \frac{\dot{q}_{hf}}{h_{hf}} \tag{3}$$

$$Nu_{hf} = \frac{h_{hf} \cdot (D_i - d_o)}{\lambda_{hf}} = 0.023 \cdot Re_{hf}^{0.8} \cdot Pr_{hf}^{0.3} \tag{4}$$

In the next step, the inner wall temperature $T_{w,i}$ is calculated by determining the conductive temperature drop over the inner tube wall.

$$T_{w,i} = T_{w,o} - \frac{\dot{Q} \cdot ln(d_o/d_i)}{2\pi \cdot \lambda_w \cdot L} \quad (5)$$

Finally, the convection coefficient at the refrigerant side h_{wf} and corresponding Nusselt number Nu_{wf} can be calculated.

$$\dot{q}_{wf} = \frac{\dot{Q}}{\pi \cdot d_i \cdot L} \quad (6)$$

$$h_{wf} = \frac{\dot{q}_{wf}}{T_{w,i} - T_{wf,b}} \quad (7)$$

$$Nu_{wf} = \frac{h_{wf} \cdot d_i}{\lambda_{wf}} \quad (8)$$

Uncertainty analysis and accuracy of results

Errors on the measured quantities and the used thermophysical properties in the data reduction method will propagate through the results. The calculation of these propagations is determined by the method described by Moffat [10]. Table 2 shows the needed accuracies. It is clear from Equation 1 that a higher heat flux will cause a larger temperature difference over the test section for both the heating and working fluid. Another consequence of this is an improved accuracy of the calculated convection coefficients. As $\dot{m}_{hf}$ is fixed, a larger ΔT_{hf} corresponds to a smaller uncertainty of $\dot{Q}$. The error on the final results are mostly due to the uncertainty of ΔT_{hf} and the accuracy of the Dittus-Boelter correlation. The latter is assumed constant under all operating conditions.

Table 2: Accuracies of sensors and thermophysical properties

Thermocouples	0.1 K
Pt100	0.1 K
Pressure transducers	6000 Pa
Mass flow meters	1%
$c_{p,hf}$	1 J/kg/K
μ_{hf}	0.00001 Pa·s
λ_{hf}	0.0001 W/m/K
λ_{wf}	3% [11]

It is important that the results found under certain operating conditions are reproducible. Figure 4 shows three separate measurements performed under approximately equal operating conditions. First of all it is clear that obtaining the exact same heat flux is more difficult than obtaining the same pressure and mass flux. Second, it shows that the results are indeed reproducible, the deviations between the different measurements are much smaller than their error bars. Even though the measured datasets are limited in temperature range and accuracy, general trends can still be seen, which will be discussed in the next section.

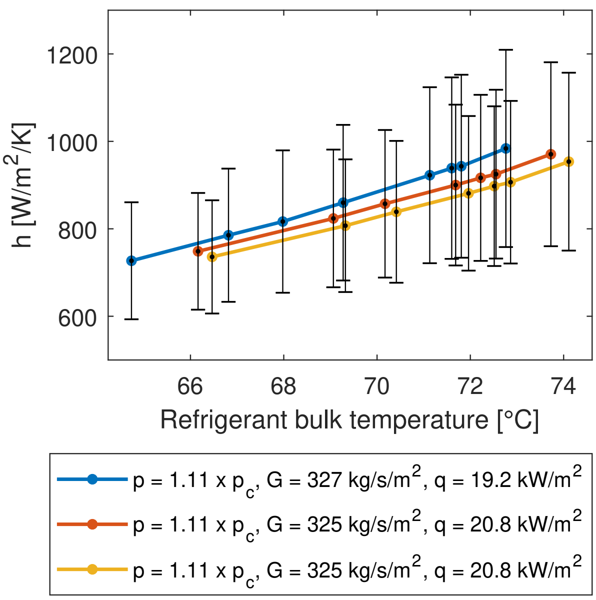

Figure 4: Repeatability check

EXPERIMENTAL RESULTS

Operating conditions

Two pressure levels corresponding to 5 and 10% above the critical pressure p_c were tested with pseudocritical temperatures of 68.3 and 70.4°C respectively. Heat fluxes of 10 and 20 kW/m^2 were chosen, corresponding to heat transfer rates of 3.11 and 6.23 kW. Four different mass fluxes between 300 and 600 kg/s/m^2 were investigated, corresponding to refrigerant mass flow rates between 0.145 and 0.289 kg/s. Combining these parameters results in 16 different operating conditions.

The refrigerant pressure p_{wf} is controlled by the expansion valve position. Higher pressures are reached when it is closed more and vice versa. The refrigerant mass flux G_{wf} is controlled by the rotational speed of the pump. Higher mass fluxes are reached at increased rotational speeds and vice versa. The heat flux $\dot{q}_{wf}$ could not be controlled directly. For a given p_{wf} and G_{wf}, $\dot{q}_{wf}$ depends on the refrigerant inlet temperature $T_{wf,in}$, thermal oil inlet temperature $T_{hf,in}$ and the thermal oil mass flow rate $\dot{m}_{hf}$. From Equation 4 it is clear that an increase in $\dot{m}_{hf}$ and $T_{hf,in}$ result in a larger h_{hf} and thus an increase in heat flux. For this reason, $\dot{m}_{hf}$ was chosen to be fixed at 2 kg/s during all measurements while $T_{hf,in}$ was varied to reach the desired heat flux. $T_{wf,in}$ was chosen such that the pseudocritical temperature was reached around the middle of the test section.

Reaching the exact proposed operating conditions was not possible. For the desired pressure of $1.05 \cdot p_c$, pressures between $1.04 \cdot p_c$ and $1.06 \cdot p_c$ were reached. Likewise, for the desired pressure of $1.10 \cdot p_c$, pressures between $1.09 \cdot p_c$ and $1.11 \cdot p_c$ were obtained.

Mass fluxes of 320, 430, 510 and 600 kg/s/m^2 were obtained. Using the method described above to control $\dot{q}_{wf}$, deviations from the setpoints are in the order of 0.5 to 1 kW/m^2. Apart from the proposed measurement conditions, some measurements were also performed with heat fluxes of about 16 to 18 kW/m^2.

The tube diameter, heat flux, mass flux and pressure will have effects on the results. As the tube dimensions do not change, the influence of the other three parameters can be studied. In the next section, one example is shown for each influence. In these graphs, the dotted vertical lines indicate the pseudocritical temperature of the dataset of the same colour. A consequence of the limited measurement accuracy is the overlap of all compared data. Nevertheless, general trends in the measured convection coefficients can still be observed. The error bars are not shown in the graphs for clarity reasons.

Influence of pressure

Figure 5 shows the measured convection coefficients as a function of the bulk refrigerant temperature for different pressures at the same mass and heat flux. As expected, an increase in pressure results in a decrease in heat transfer coefficients. Due to the limited measurement accuracy, the two measurements for a pressure of $1.09 \cdot p_c$ show varying results. Still, the expected influence of the pressure holds.

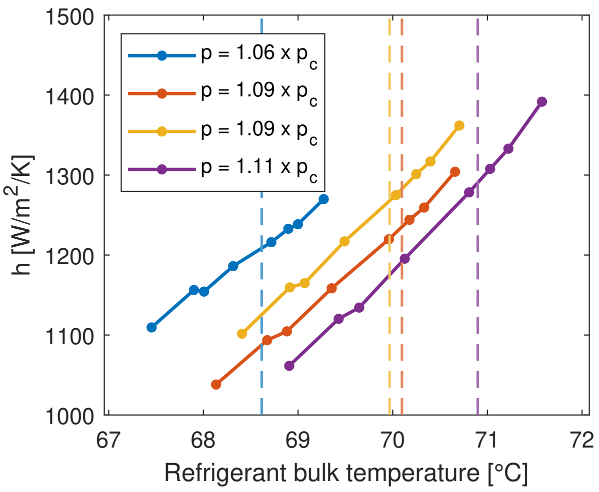

Figure 5: Influence of pressure at G_{wf}=320 kg/s/m^2 and $\dot{q}_{wf}$=10 kW/m^2

Comparisons of convection coefficients at other combinations of mass and heat fluxes show similar results. In one case, the influence of the pressure level is not very clear. This is presumably caused by the limited accuracy of the setup.

Influence of mass flux

Figure 6 shows the measured convection coefficients as a function of the bulk refrigerant temperature for different mass fluxes at the same pressure and heat flux. The results meet the expectation, a higher mass flux and thus a higher Reynolds number causes increased convection coefficients.

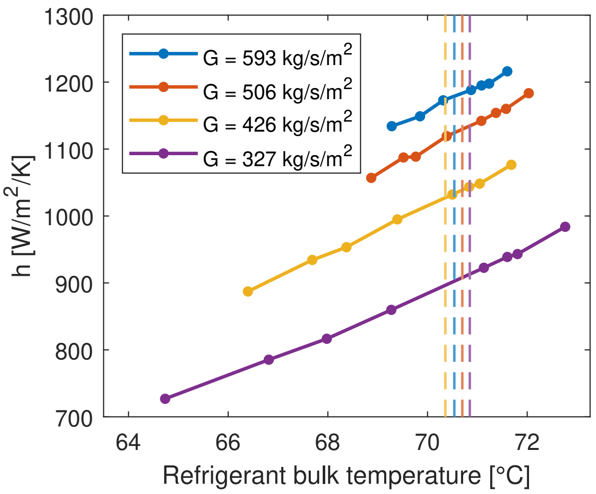

Figure 6: Influence of mass flux at p_{wf}=1.10 x p_c and $\dot{q}_{wf}$=20 kW/m^2

In all other comparisons, large deviations in mass flux result in clear differences in convection coefficients. However, if the difference is smaller (comparison between 600 and 510 kg/s/m^2 for example), the difference can be very small or zero. Again, this could be explained by the limited measurement accuracy.

Influence of heat flux

Figure 7 shows the measured convection coefficients as a function of the bulk refrigerant temperature for different heat fluxes at the same pressure and mass flux. Also in this case the results are as expected, higher heat fluxes lead to decreased convection coefficients.
In all other comparisons, heat fluxes of 10 kW/m^2 clearly result in higher convection coefficients compared to 20 kW/m^2. In some cases, no clear difference can be seen when comparing datasets of 17-18 and 20 kW/m^2. Again, this could be explained by the limited measurement accuracy.

Wilson plots

A first step to develop a new correlation can be made using the Wilson plot method [12]. Figure 8 shows all data points from the measurement matrix together with a linear fitting. Red dots represent the data for a heat flux of 20 kW/m^2, blue dots for a heat flux of 10 kW/m^2. Note that only a limited range of Reynolds numbers is present in the dataset, ranging from about $130 \cdot 10^3$ to $630 \cdot 10^3$. Still, larger Reynolds

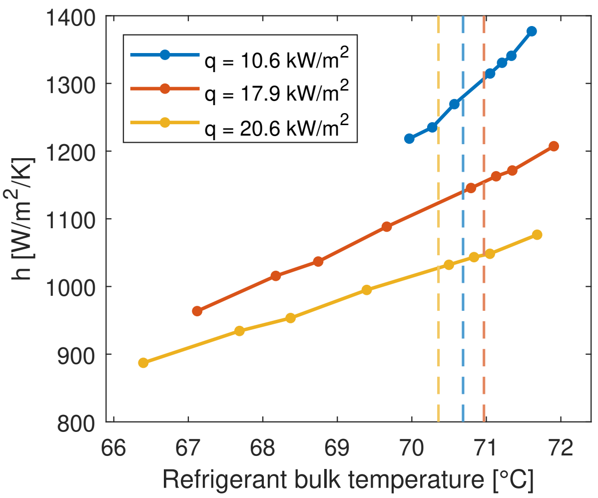

Figure 7: Influence of heat flux at p_{wf}=1.10 x p$_c$ and $\dot{G}_{wf}$=430 kg/s/m^2

numbers correspond to higher Nusselt numbers generally. The fitted curve for the whole dataset results in $Nu_b = 10.186 \cdot Re_b^{0.329}$.

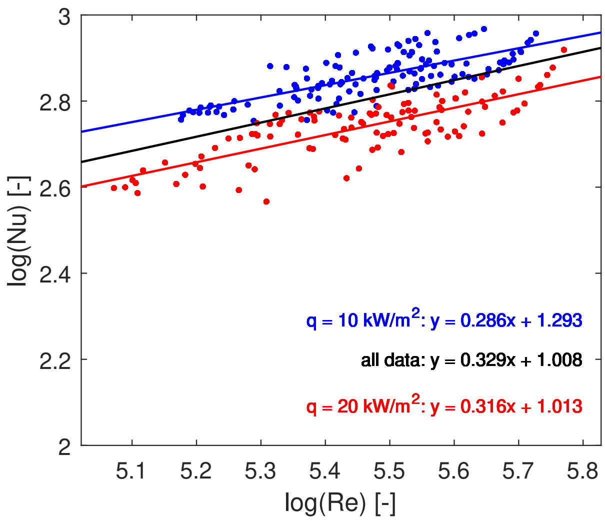

Figure 8: Wilson plots

In addition, this dataset can be split up according to the heat flux. As explained above, increasing the heat flux results in lower convection coefficients. The fitted curves are almost parallel for this range of Reynolds number. This leads to the conclusion that the influence of the heat flux on the obtained convection coefficients is more or less independent of the refrigerant Reynolds number. In addition, the fitted curve for all data in the measurement matrix lies between the red and blue curves as expected.

Heat transfer coefficient peaks

In all measurements, no peaks in heat transfer coefficients were seen at or around the pseudocritical temperature. This is opposed to different results found in literature. This is presumably caused by two factors. First, no wall temperature measurements are incorporated in the measurement setup. Buoyancy effects are to be expected as the test section is placed horizontally, causing higher convection coefficients at the bottom of the tube. Because no variation in wall temperature is assumed in the data reduction, these effects could not be measured in any way. Second, $\dot{Q}$ was assumed to be constant over the test section length because of the malfunctioning thermocouples at the thermal oil side. As $\dot{q}_{hf}$ and $\dot{Q}$ are needed to determine the temperature drops due to convection at the oil side and conduction through the inner tube wall, the resulting values for $T_{w,i}$ do not vary much over the test section length and presumably deviate from the actual inner wall temperatures. According to Equation 7, this heavily influences the obtained values for h_{wf}.

CONCLUSION AND FUTURE WORK

Measurements on supercritical R125 flowing in a horizontal tube were performed at pressures between $1.04 \cdot p_c$ and $1.11 \cdot p_c$, refrigerant mass fluxes between 320 and 600 kg/s/m^2 and heat fluxes between 9 and 22 kW/m^2. The influences of the pressure, mass flux and heat flux could be investigated. In general, lower pressures, higher mass fluxes and lower heat fluxes result in higher convection coefficients. These results agree with expected results found in literature.

While the accuracy on the convection coefficients proved to be quite low, a first step to develop a new correlation could be done. Using the Wilson plot method, a linear trend could be seen for $log(Nu_b)$ as a function of $log(Re_b)$. Higher bulk Reynolds numbers correspond to larger Nusselt numbers and thus larger convection coefficients. When the data was split up according to low and high heat flux, a clear difference could be seen. The lower heat flux resulted in approximately a fixed increase in $log(Nu_b)$ for the range of tested Reynolds numbers.

Future work includes broadening the bulk refrigerant temperature, pressure, mass flux and heat flux ranges. In addition, the setup will be adapted such that wall temperature measurements are included. This leads to the detection of variable wall temperatures over the inner tube circumference due to buoyancy effects. In addition, this would greatly improve the accuracy on the obtained convection coefficients since the Dittus-Boelter correlation would not be needed in the data reduction. Finally, the setup can be adapted for testing other low GWP working fluids suitable for heat recovery applications at the supercritical state.

REFERENCES

[1] S. Lecompte, E. Ntavou, B. Tchanche, G. Kosmadakis, A. Pillai, D. Manolakos, and M. de Paepe, "Review of experimental research on supercritical and transcritical thermodynamic cycles designed for heat recovery application," *Applied Sciences*, vol. 9, no. 12, pp. 1–26, 2019.

[2] K. Yamagata, K. Nishikawa, S. Hasegawa, T. Fujii, and S. Yoshia, "Forced convective heat transfer to supercritical water flowing in tubes," *International Journal of Heat and Mass Transfer*, vol. 15, no. 12, pp. 2575–2593, 1972.

[3] S. Yu, H. Li, X. Lei, Y. Feng, Y. Zhang, H. He, and T. Wang, "Influence of buoyancy on heat transfer to water flowing in horizontal tubes under supercritical pressure," *Applied Thermal Engineering*, vol. 59, no. 1-2, pp. 380–388, 2013.

[4] M. Bazargan, *Forced convection heat transfer to turbulent flow of supercritical water in a round horizontal tube.* PhD thesis, 2001.

[5] C. R. Zhao and P. X. Jiang, "Experimental study of in-tube cooling heat transfer and pressure drop characteristics of R134a at supercritical pressures," *Experimental Thermal and Fluid Science*, vol. 35, no. 7, pp. 1293–1303, 2011.

[6] R. Tian, D. Wang, Y. Zhang, Y. Ma, H. Li, and L. Shi, "Experimental study of the heat transfer characteristics of supercritical pressure R134a in a horizontal tube," *Experimental Thermal and Fluid Science*, vol. 100, pp. 49–61, 2019.

[7] M. Lazova, A. Kaya, S. Lecompte, and M. De Paepe, "Presentation of a test-rig for heat transfer measurements of a fluid at supercritical state for organic Rankine cycle application," in *Proceedings of the 16th International Heat Transfer Conference*, pp. 8389–8396, 2018.

[8] S. Garimella, "Near-critical/supercritical heat transfer measurements of R-410a is small diameter tube," tech. rep., Georgia Institute Of Technology, 2008.

[9] F. Dittus and L. Boelter, "Heat Transfer in Automobile Radiators of the Tubular Type," *Publications in Engineering, University of California, Berkeley*, vol. 2, no. 13, pp. 443–461, 1930.

[10] R. J. Moffat, "Describing the uncertainties in experimental results," *Experimental Thermal and Fluid Science*, vol. 1, no. 1, pp. 3–17, 1988.

[11] R. A. Perkins and M. L. Huber, "Measurement and correlation of the thermal conductivity of pentafluoroethane (R125) from 190 K to 512 K at pressures to 70 MPa," *Journal of Chemical and Engineering Data*, vol. 51, no. 3, pp. 898–904, 2006.

[12] J. Fernández-Seara, F. J. Uhía, J. Sieres, and A. Campo, "Experimental apparatus for measuring heat transfer coefficients by the Wilson plot method," *European Journal of Physics*, vol. 26, no. 3, 2005.

Contents

List of Figures

List of Tables

Nomenclature

Abbreviations

DHT	Deteriorated heat transfer
GWP	Global warming potential
HTC	Heat transfer coefficient
IHT	Improved heat transfer
LMTD	Logarithmic mean temperature difference
NHT	Normal heat transfer
ODP	Ozone depletion potential
ORC	Organic Rankine cycle

Symbols

β	Thermal expansion coefficient	K^{-1}
$\dot{m}$	Mass flow rate	kg/s
$\dot{Q}$	Heat transfer rate	W
$\dot{q}$	Heat flux	W/m^2
λ	Thermal conductivity	$W/(m \cdot K)$
μ	Dynamic viscosity	$kg/(m \cdot s)$
ν	Kinematic viscosity	m^2/s
ρ	Mass density	kg/m^3
A	Surface area	m^2
c_{p}	Specific heat capacity	$J/(kg \cdot K)$
D	Diameter outer tube	m
d	Diameter inner tube	m
G	Mass flux	$kg/(m^2 \cdot s)$
Gr	Grashof number	$-$
h	Convection coefficient	$W/(m^2 \cdot K)$
h	Specific enthalpy	J/kg
L	Length	m
Nu	Nusselt number	$-$

p	Pressure	Pa
Pr	Prandtl number	$-$
Re	Reynolds number	$-$
s	Specific entropy	$J/(kg \cdot K)$
T	Temperature	K
v	Velocity	m/s
W	Power	W

Subscripts

b	Bulk
c	Critical
hf	Heating fluid
i	Inner
in	Inlet
o	Outer
out	Outlet
pc	Pseudocritical
w	Wall
wf	Working fluid

Chapter 1

Introduction

One of the largest challenges facing the energy sector today is providing increasing amounts of energy while reducing its environmental impact. Finding sustainable ways to meet our energy demand is not only needed to lower greenhouse gas emissions and reduce global warming effects, but also because fossil fuels are exhaustible [1]. Up until now, large-scale electricity production is mostly done by combustion of fossil fuels such as gas, oil and coal or by nuclear power plants. Many power plants based on these fuels use a water/steam Rankine cycle, explained in Section 1.1. The main problem is that all of these sources (oil, gas, coal and nuclear) are non-renewable. On top of that, gas, oil and coal based power plants emit large amounts of CO_2 and other pollutants into the atmosphere.

A different approach could be the use of other (renewable) heat sources such as solar and geothermal energy, in which heat is typically available at a lower temperature compared to conventional power plants [2]. The organic Rankine cycle (ORC), explained in section 1.2, has proven to be suitable technology for heat-to-power applications. For heat-to-heat systems, heat pumps are starting to replace classical gas boilers nowadays to provide heat to buildings. They are based on the vapour compression refrigeration cycle.

In practice, the cycles mentioned above have mostly evolved from subcritical to supercritical operation [3]. Thermodynamic cycles operating under supercritical conditions have proven to be a good way to increase efficiencies compared to subcritical cycles [4]. A fluid is at the supercritical state when its temperature and pressure are above its critical temperature and pressure, explained further in this chapter. Thermodynamic cycles of interest include heat-to-power (Rankine, Brayton) and heat-to-heat (heat pump) cycles. The importance for improved efficiencies is clear in heat-to-power cycles: for the same amount of work provided, less energy is needed as an input.

As is the case for the water/steam Rankine cycle, operation under supercritical conditions can benefit the efficiency of an ORC or heat pump cycle. Today, research is still needed to study supercritical heat transfer behaviour and its impact on the cycle components [4]. Knowledge of this heat transfer behaviour is beneficial for heat exchanger design used in these technologies as the lack of accurate correlations often lead to oversized heat exchangers.

At Ghent University, a transcritical ORC setup to determine supercritical heat transfer behaviour was built in the previous years. The evaporator of this setup is a horizontal tube-in-tube counterflow heat exchanger and is rigged with measurement equipment to determine local convection coefficients of the working fluid. The focus of this thesis lies on the supercritical heat transfer behaviour at transcritical ORC conditions. In the introductory chapter, the ORC is introduced. In the next chapter, an overview of supercritical heat transfer and the main goal of this thesis are given.

1.1 The water/steam Rankine cycle

To convert heat into useful work, the water/steam Rankine cycle can be used. The cycle consists of four main components and is depicted in Figure 1.1.

First, in an ideal cycle, saturated liquid is isentropically compressed to a higher pressure using a pump. Second, heat is added at a constant pressure in a boiler until the compressed liquid has become saturated or superheated vapour. Third, it is expanded isentropically to a lower pressure in an expander. This is where work is extracted. Finally, heat is rejected in the condenser at a constant pressure until the saturated liquid state is reached again, closing the cycle [3]. Figure 1.1 shows the ideal Rankine cycle, where in reality compression and expansion are not perfectly isentropic and pressure losses exist during evaporation and condensation.

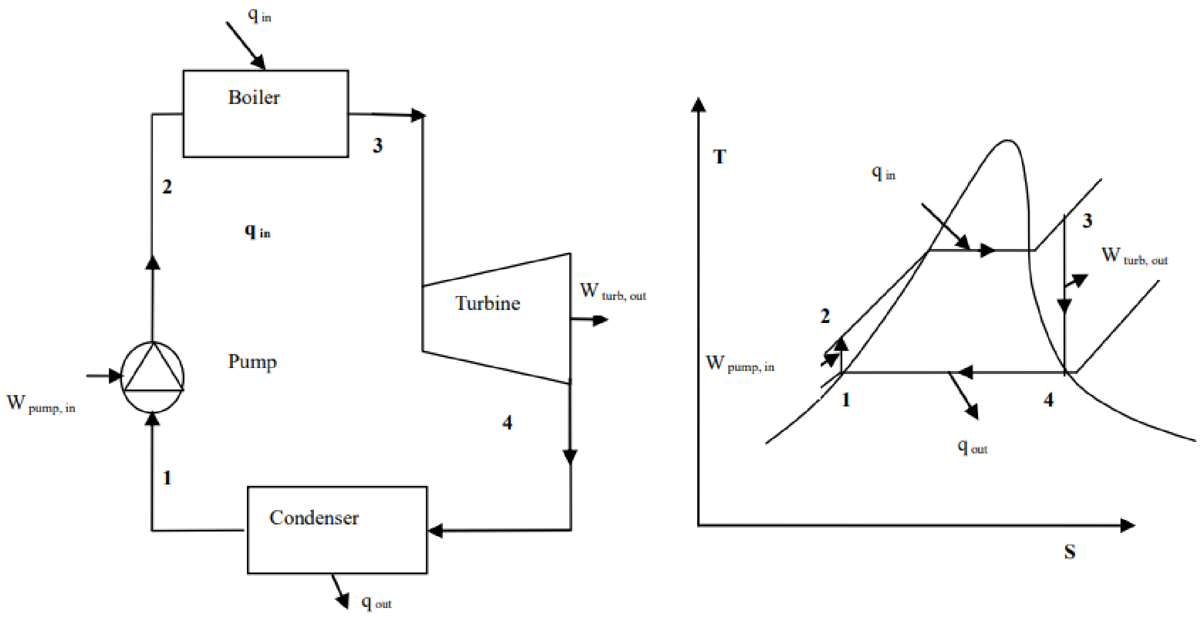

Figure 1.1: Ideal Rankine cycle layout with corresponding T-s diagram [5]

1.2 The organic Rankine cycle

On the level of the cycle components, an ORC does not differ significantly from a classic water/steam Rankine cycle. The main difference lies in the working fluid and applications. Instead of water/steam, an organic fluid is used that is able to evaporate at lower temperatures, making them more suitable for converting heat from low-temperature heat sources into power. Such heat sources include industrial waste heat, geothermal heat, biomass combustion and solar heat [4].

1.2.1 ORC classification

Multiple different ORC architectures exist which can be classified into three categories depending on the pressures and temperatures used [4]: subcritical, transcritical and supercritical. Important for this characterization are the critical temperature T_c and critical pressure p_c. The critical temperature is the highest temperature at which liquid and vapour phases can coexist in equilibrium, the pressure at this so-called critical point is the critical pressure [3]. In a T-s diagram, this is the point where the saturated liquid and saturated vapour lines meet.

First, an ORC is called subcritical when both the evaporator and condenser pressures are below the critical pressure of the working fluid. This means that the cycle passes the two-phase region twice, during evaporation and condensation. The T-s diagram is identical to the one in Figure 1.1. Second, the transcritical ORC has an evaporation pressure that exceeds the critical pressure of the working fluid and a condensation pressure below the critical pressure. The result is that the two-phase region is avoided during evaporation so no discontinuity is present in the temperature profile during evaporation. Third, in the supercritical ORC, evaporation and condensation both take place at supercritical pressures. The cycle never passes the two-phase region. In literature, the term supercritical is also often used for a transcritical ORC [4]. In this work, the definitions as stated above will be followed. The typical T-s diagrams of the supercritical and transcritical ORC are shown in Figure 1.2.

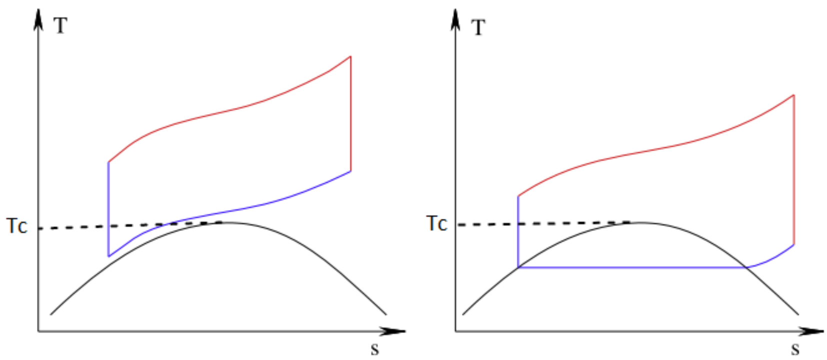

Figure 1.2: T-s diagram of the supercritical (left) and transcritical (right) ORC [6]

1.2.2 The transcritical ORC

When using a heat source with a finite heat capacity, heat transfer will not take place at a constant heat source temperature. If the evaporation process of a subcritical and transcritical ORC are compared, a better temperature match is found for the transcritical cycle. The temperature profiles can be seen in Figure 1.3. In the transcritical case, no discontinuity in the temperature profile is seen during evaporation. This causes smaller temperature differences to exist in the evaporator, compared to the subcritical cycle. This can lower the irreversibilities in the heat exchanger, lower exergy destruction and improve the efficiency of the cycle because of these smaller temperature differences [7, 8]. This efficiency η is defined as the ratio of the net work extracted to the total heat input of the cycle:

$$\eta = \frac{\dot{W}_{net}}{\dot{Q}_{in}} = \frac{\dot{W}_{extr} - \dot{W}_{pump}}{\dot{Q}_{in}} \tag{1.1}$$

Where $\dot{Q}_{in}$ is the heat added to the working fluid by the heat source, $\dot{W}_{extr}$ is the power extracted during expansion and $\dot{W}_{pump}$ is the power consumed by the pump. The theoretical maximum for this efficiency is given by the Carnot efficiency and only depends on the temperatures $\mathrm{T_L}$ and $\mathrm{T_H}$ at which the heat is transferred:

$$\eta_{max} = 1 - \frac{T_L}{T_H} \tag{1.2}$$

Where $\mathrm{T_L}$ is the temperature of the cold source and $\mathrm{T_H}$ the temperature of the heating source. It is clear that this maximum efficiency will always be smaller than one and lowers when the temperature difference between $\mathrm{T_L}$ and $\mathrm{T_H}$ decreases.

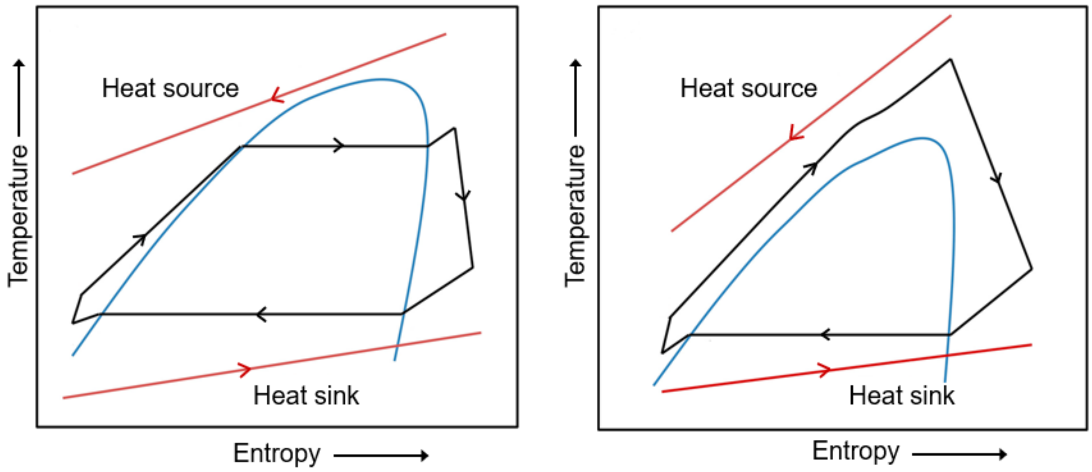

Figure 1.3: Temperature profiles of the subcritical (left) and transcritical (right) ORC [9]

1.3 Working fluid selection

When selecting the working fluid for a certain application, multiple factors should be taken into account [10–12]:

- **General properties**: Preferably a chemically stable, non-fouling and non-corrosive working fluid.
- **Safety**: Preferably a non-toxic and non-flammable working fluid.
- **Saturation curve shape**: Depending on the slope of the saturation curve (dT/ds) at the vapour side in the T-s diagram, a working fluid can be either dry, isentropic or wet. This is defined by the factor ξ = ds/dT, the inverse of that slope. ξ>0 holds for a dry fluid, ξ=0 holds for an isentropic fluid and ξ<0 holds for a wet fluid. The difference can be seen in Figure 1.4. This naming is easily explained: when the working fluid is a saturated vapour, a wet working fluid will expand to the two-phase region. Likewise a dry working fluid will expand to the superheated vapour region and an isentropic working fluid to a saturated vapour again. In general, dry and isentropic fluids are preferred since no superheating is required to avoid liquid droplets forming in the turbine or other expansion device.
- **ODP and GWP**: The ozone depletion potential (ODP) is the amount of degradation a refrigerant causes to the ozone layer, compared to R-11 (CCl_3F). Since the international Montreal protocol was signed in 1987, refrigerants with a ODP over

zero were phased out and are forbidden nowadays. The global warming potential (GWP) indicates how large the greenhouse effect is of a refrigerant, compared to CO_2. It is preferably low.

- **Critical parameters**: The critical temperature T_c should not exceed the temperature of the heat source in a transcritical cycle. The critical pressure p_c is preferably not too high, since higher pressures lead to potential dangerous situations and higher pumping power, lowering the net work extracted.

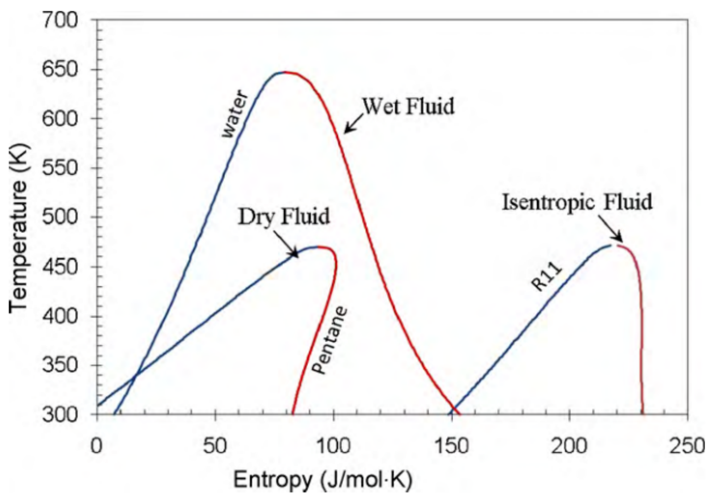

Figure 1.4: T-s diagrams of wet, dry and isentropic fluids [7]

For the case of a transcritical ORC, the critical parameters of the working fluid should match the heat source. This implies a critical temperature below the heat source temperature and a limited critical pressure. In addition, low GWP refrigerants are preferred to limit its environmental impact. As in any thermodynamic cycle, the general and safety properties should be satisfied as well.

In the vapour generator of a transcritical ORC, heat is added to the working fluid supercritically. The next chapter gives an overview of the knowledge on this type of heat transfer. The main focus lies on heat transfer occurring in horizontal tubes because the test setup, described in the third chapter, is of this type and is prone to certain specific phenomena.

Chapter 2

An overview of supercritical heat transfer

Heat transfer to supercritical fluids has been studied in the past. These studies show that this heat transfer is heavily influenced by the rapid changes in thermophysical properties of the fluid. This leads to unusual heat transfer behaviour around the pseudocritical temperature T_{pc}, defined as the temperature where the specific heat capacity has a peak for a certain supercritical pressure [13]. Three expressions are used for describing the heat transfer phenomena at supercritical conditions: normal heat transfer (NHT), improved heat transfer (IHT) and deteriorated heat transfer (DHT) [14]. In the case of NHT, heat transfer coefficients are similar to subcritical convective heat transfer coefficients, determined by the single-phase Dittus-Boelter type correlations. IHT provides higher values compared to NHT and is associated with lower (local) wall temperatures. For DHT, lower heat transfer coefficients compared to NHT are present, resulting in higher (local) wall temperatures.

2.1 Thermophysical properties at supercritical conditions

In Figure 2.1 variations of the specific heat capacity c_p, density ρ, thermal conductivity λ and dynamic viscosity μ can be seen for R125, which has a critical temperature of 66°C (black vertical line) and a critical pressure of 36 bar [15]. For these properties, three isobars are shown corresponding to pressures of 5, 10 and 15% above the critical pressure. Figure 2.1 was made using the CoolProp library [15]. It is immediately clear that these properties do not show discontinuities at supercritical pressures as opposed to the discontinuities present at the phase transitions at subcritical conditions.

For the specific heat capacity, a peak is visible for each pressure at their pseudocritical temperatures (black vertical dotted lines). It is also clear that T_{pc} increases with the pressure and the peak in specific heat capacity decreases with the pressure. For the density, thermal conductivity and viscosity a sudden decrease is visible at the pseudocritical temperature. For higher pressures, these effects become less distinct. In general, the thermophysical properties of the fluid will change most rapidly around the pseudocritical temperature and the fluid will be more liquid-like at temperatures lower than T_{pc} and more gas-like when its temperature exceeds T_{pc}.

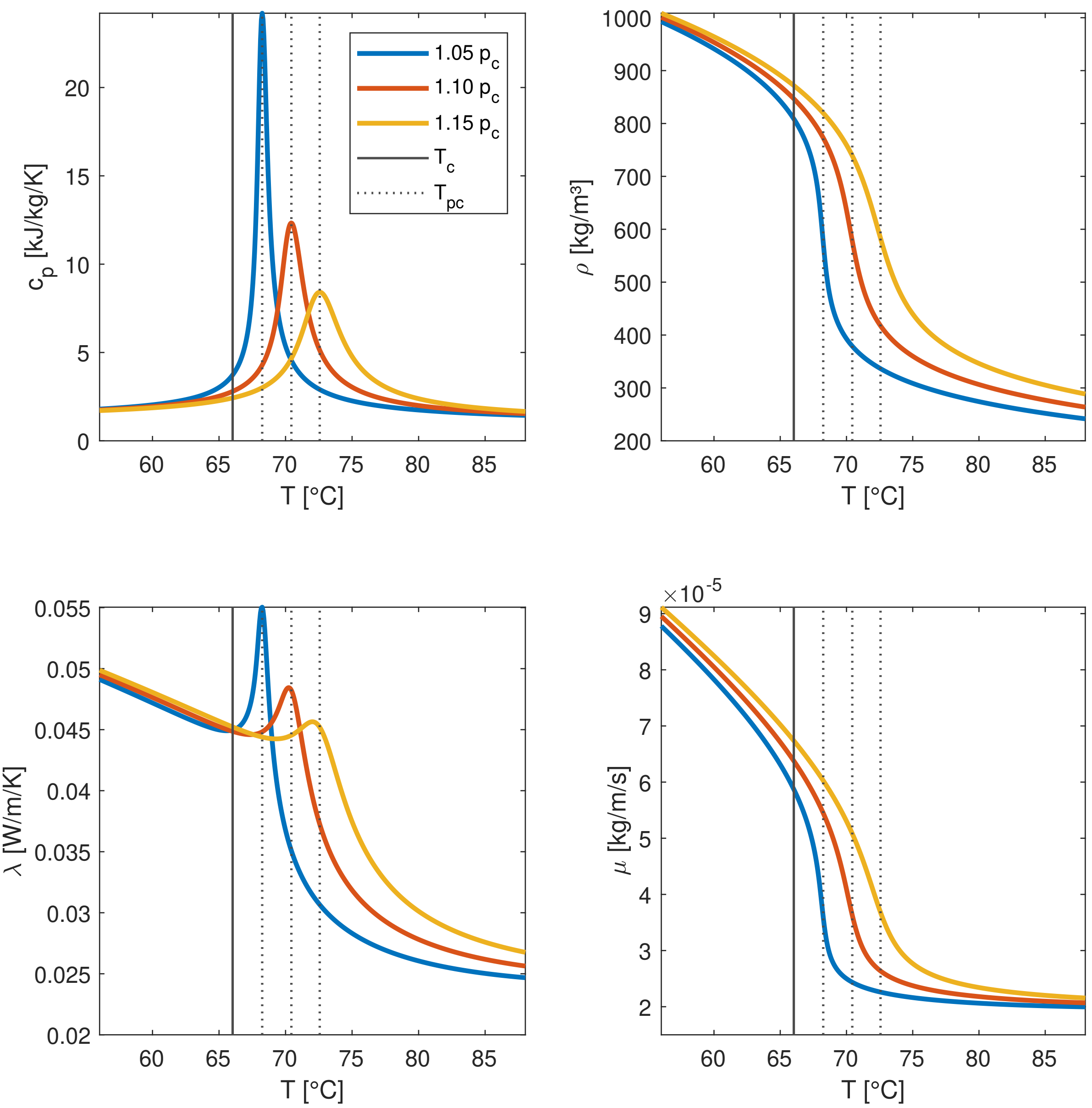

Figure 2.1: Variation of specific heat capacity, density, thermal conductivity and viscosity at supercritical conditions for R125

2.2 Influences on heat transfer behaviour

Often disagreements between existing heat transfer correlations and experimental data of supercritical fluids are found. This is caused by the rapid variation of thermophysical properties in the supercritical region [16]. In general, the heat transfer behaviour at supercritical conditions is influenced by the pressure, mass flux, heat flux and tube diameter. Depending on these variables, buoyancy effects may take place which can influence local temperatures and heat transfer coefficients significantly.

2.2.1 Buoyancy effects

Supercritical fluids flowing in a horizontal tube are subject to buoyancy effects due to rapid density variations in the fluid, see Figure 2.1. Hotter and thus less dense fluid will rise to the top of the tube while heavier colder fluid will remain at the bottom. This natural convection leads to variable wall temperatures around the tube circumference and decreases the heat transfer coefficient at the top while the heat transfer coefficient at the bottom increases. This buoyancy effect is present when low mass fluxes and/or high heat fluxes are used [16, 17]. Research on this effect in horizontal tubes was first done in the 1960s by Krasyakova et al. [18] and Shitsman [19] on supercritical water who observed these temperature differences.

More recently, Yu et al. [17] performed experimental research on the buoyancy effect on supercritical water in horizontal tubes. Inner tube diameters were 26 and 43 mm, pressure 25 MPa, mass flux 300 to 1000 kg/(m^{2}s) and heat fluxes up to 400 kW/m^2. In Figures 2.2 and 2.3 wall temperatures and heat transfer coefficients can be seen as a function of the bulk enthalpy for a mass flux of 600 kg/(m^{2}s) and a heat flux of 300 kW/m^2. It is clear that the wall temperatures at the top are higher than at the bottom of the tube, with a temperature difference of up to 80°C. However, at higher bulk enthalpies (and thus higher bulk temperatures, so further away from the pseudocritical temperature) this temperature difference seems to disappear. This is because the thermophysical properties do not vary rapidly any more in this region, so buoyancy effects driven by density differences will be less significant. When looking at the heat transfer coefficients, it is clear that IHT takes place near and before the pseudocritical point for the bottom surface of the tube while heat transfer at the top remains more constant, but has lower values. Also, it can be seen that for high enthalpies the heat transfer coefficients are almost equal which is caused by the nearly equal wall temperatures as described above.

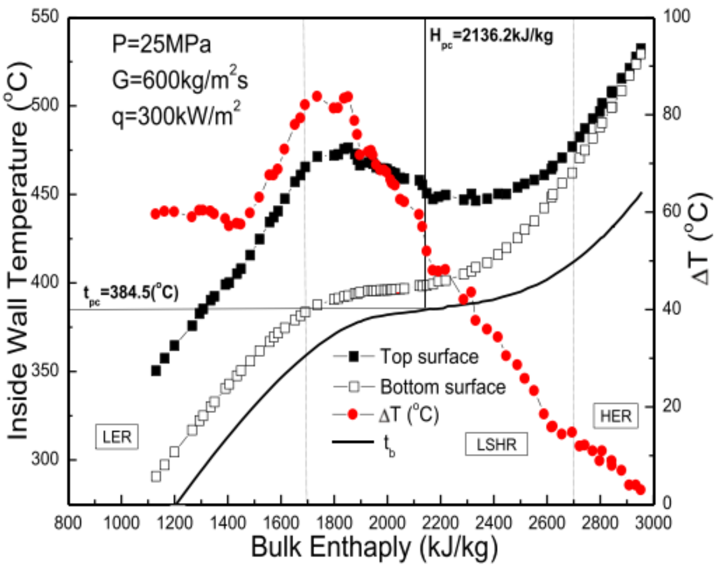

Figure 2.2: Buoyancy influence on wall temperatures [17]

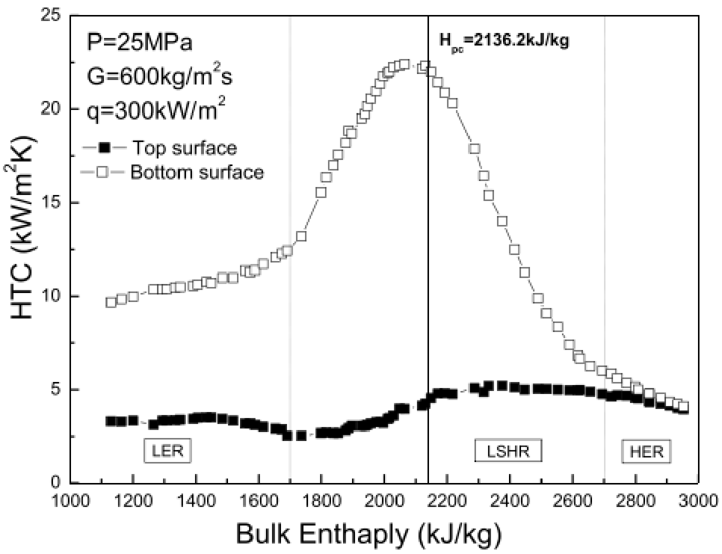

Figure 2.3: Buoyancy influence on heat transfer coefficients [17]

Wang et al. [20] have performed numerical simulations for supercritical CO_2 in large horizontal tube diameters. An inlet temperature of 15.4°C, pressure of 7.59 MPa and heat flux of 15.1 kW/m^2 was used as input. The variation of temperatures can be seen in Figure 2.4. It is clear that a radial temperature profile is present, with strong variations near the tube walls. Further downstream in the tube, at higher bulk temperatures, the temperature difference between top and bottom increases. This agrees with the results of Yu et al. described above, since the shown temperatures are below the pseudocritical temperature of 32°C in this simulation.

The velocity profile along two sections can be seen in Figure 2.5. Clearly, natural convection takes place in the tube as seen by the circulation near the sides of the tube. This causes a layered structure that is more distinct further in the tube. Fluid velocities appear to be higher at the lower half of the tube, which in this work is explained by a thicker boundary layer at the top of the tube. This thicker boundary layer is caused by the secondary flow that takes the near-wall fluid upward, causing the low-momentum flow to accumulate near the top of the tube [20].

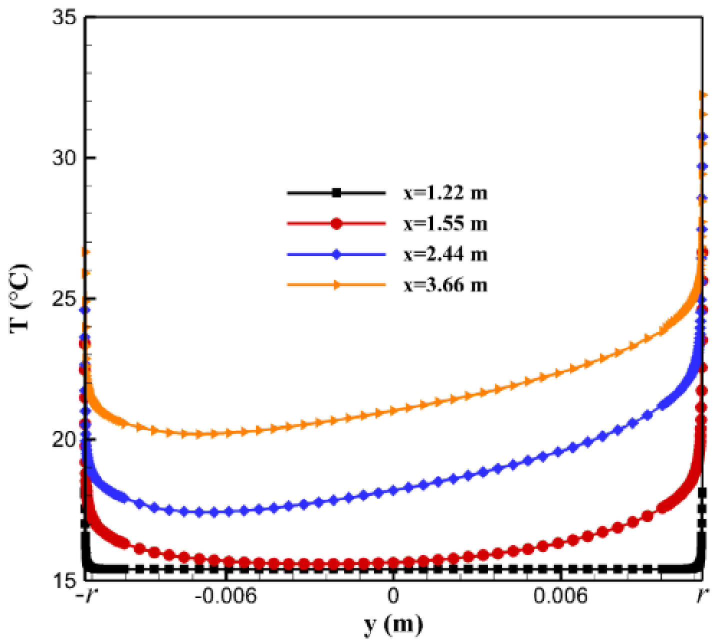

Figure 2.4: Temperature profiles along radius by Wang et al. [20]

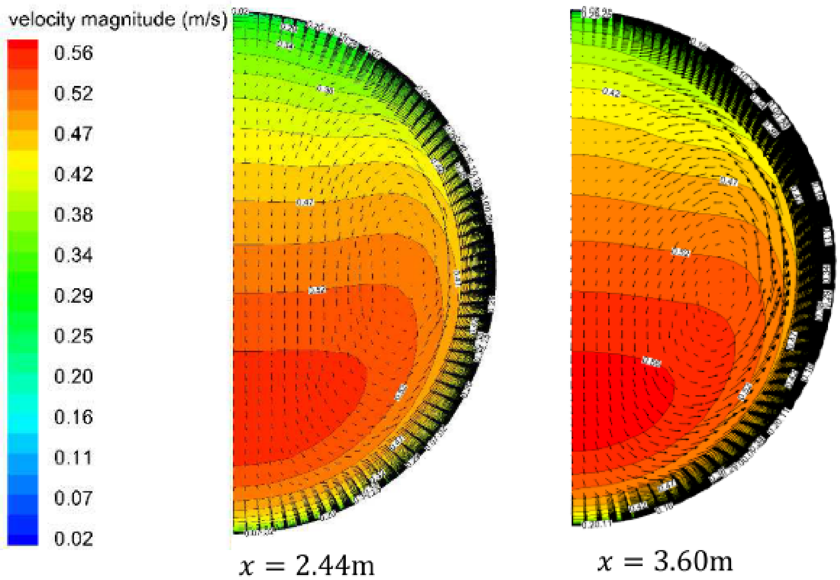

Figure 2.5: Velocity profile of supercritical CO_2 in a horizontal tube by Wang et al. [20]

In general, the buoyancy effect can have a large influence on wall temperatures and heat transfer coefficients. Different criteria were developed in the past to determine whether buoyancy effects will be present [21]. A widely used criterion developed by Jackson and Hall [22] stated that the value of Gr/Re^2 (also called the Richardson number) could be used to evaluate the buoyancy effects in supercritical flows [17]. Re is the Reynolds number of the fluid and Gr is the Grashof number, defined for tubular flow as:

$$Re = \frac{v \cdot D}{\nu} \tag{2.1}$$

$$Gr = \frac{g \cdot \beta \cdot (T_{\mathrm{w}} - T_{\mathrm{b}}) \cdot D^3}{\nu^2} \tag{2.2}$$

With v the velocity of the fluid, D the inner diameter of the tube, ν the kinematic viscosity, β the thermal expansion coefficient and g the gravitational acceleration. So, the Grashof number is a measure for the ratio of buoyancy to viscous forces. Jackson and Hall stated that if $Gr/Re^{2.7} < 10^{-5}$ the buoyancy effects are negligible for vertical flows. Zhang et al. [23] numerically investigated heat transfer to supercritical water in horizontal circular tubes with an inner diameter of 7.5 mm and found this criterion to be fairly accurate, even though it was developed for vertical flows. However, the results of Bazargan et al. [16] disagreed with this criterion for supercritical water flowing in a horizontal round tube with an inner diameter of 6.3 mm. They found the criterion of Petukhov and Polyakov [24], which uses alternative definitions for the Grashof number, to be a better predictor for the onset of buoyancy effects. So it can be concluded that, up until now, no single criterion is capable of accurately predicting whether buoyancy effects will emerge.

2.2.2 Influence of heat flux

Yamagata et al. [13] experimentally investigated the influence of the heat flux for heat transfer to supercritical water in horizontal and vertical tubes. In Figures 2.6 and 2.7 wall temperatures and heat transfer coefficients can be seen for the horizontal tubes case. Heat fluxes of 233, 465, 698 and 930 kW/m^2 were tested at a pressure of 245 bar, mass flux of 1260 and 1830 kg/(m^{2}s) and tube diameter of 7.5 mm. For the two lowest heat fluxes, virtually no temperature difference can be seen between top and bottom of the tube. However, for the highest two heat fluxes temperature differences can be clearly seen which seem to increase with the heat flux. For the heat transfer coefficients, peaks around the pseudocritical temperature can be seen again. This peak occurs at a bulk temperature slightly below T_{pc} while the corresponding wall temperature is higher than T_{pc}. The maximum value of the heat transfer coefficients increases with lower heat fluxes. These results indicate that buoyancy effects are more pronounced at higher heat fluxes.

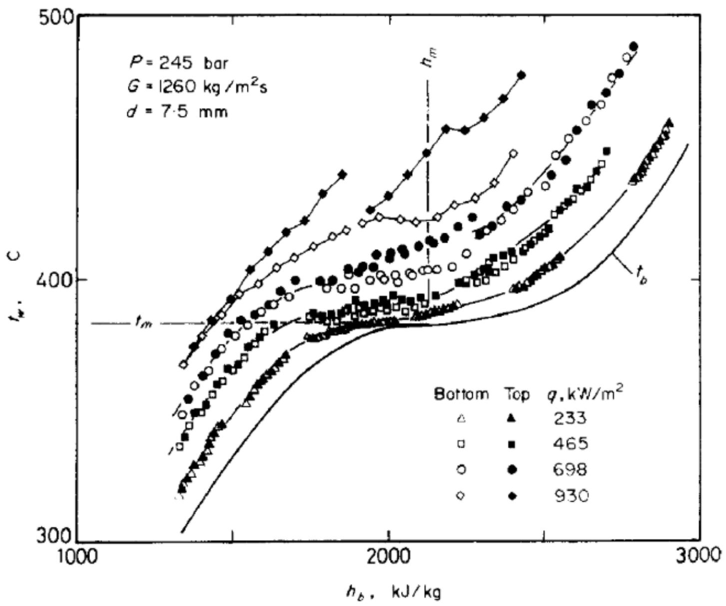

Figure 2.6: Wall temperatures as a function of bulk enthalpy for different heat fluxes [13]

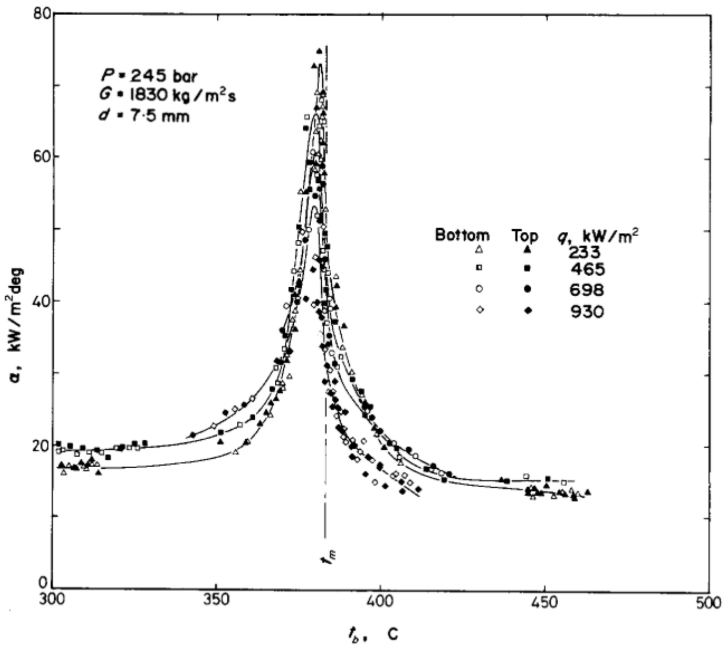

Figure 2.7: Heat transfer coefficients as a function of bulk temperatures for different heat fluxes [13]

2.2.3 Influence of mass flux

The influence of mass flux was also studied in the research of Yu et al. [17], which was on water flowing in a horizontal tube. In Figures 2.8 and 2.9 wall temperatures and heat transfer coefficients can be seen. A pressure of 25 MPa and a heat flux of 200 kW/m^2 was used, while the mass flux was set to 300 and 600 kg/(m^{2}s). It is clear that for a lower mass flux a greater temperature difference is present between the top and bottom of the tube. At a mass flux of 600 kg/(m^{2}s), only very little temperature differences exist between top and bottom. This leads to the conclusion that buoyancy effects are less dominant when using larger mass fluxes. When looking at the heat transfer coefficients, it is clear that for both heat fluxes IHT is visible at the bottom of the tube. However, the ratio in heat transfer coefficients between top and bottom is smaller for higher mass fluxes. Due to a higher mass flux, velocities will be higher and so the flow becomes more turbulent, leading to higher forced convective heat transfer. So it can be concluded that higher mass fluxes improve heat transfer both at top and bottom.

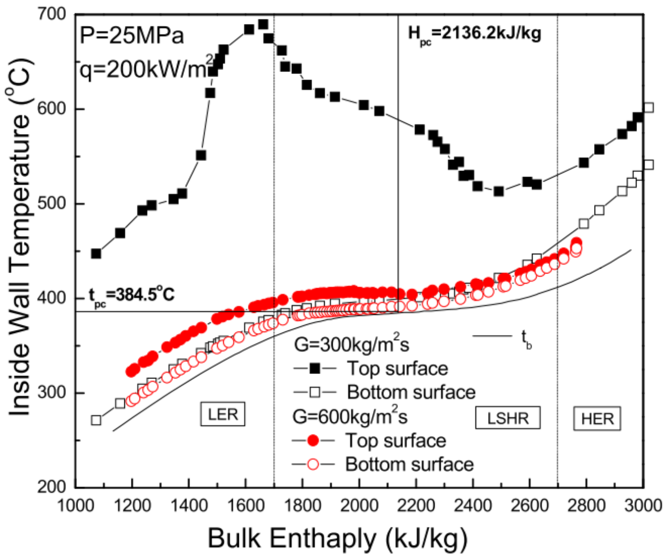

Figure 2.8: Wall temperatures as a function of bulk enthalpy for different mass fluxes [17]

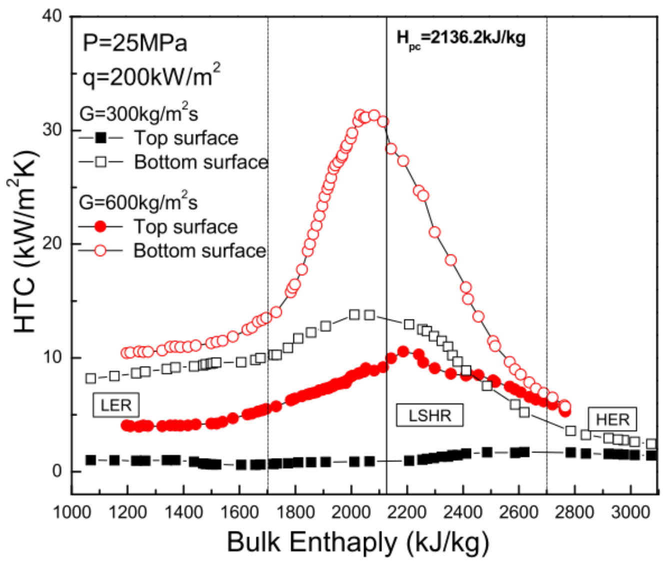

Figure 2.9: Heat transfer coefficients as a function of bulk enthalpy for different mass fluxes [17]

Different criteria for determining the onset of deteriorated heat transfer were proposed in the past, based on a critical value for the heat flux as a function of the mass flux [21]. Figure 2.10 shows some examples compared to experimental data from different working fluids under different operating conditions. For the data is this figure, correlations for predicting onset of DHT based on the heat transfer properties of water are good predictors for supercritical heat transfer to water only. They all overpredict the experimental values for CO_2 significantly. The opposite holds true for correlations based on CO_2, which tend to underestimate empirical data for supercritical water flow. This leads to the conclusion that these available criteria for one working fluid cannot be directly applied for any other working fluid.

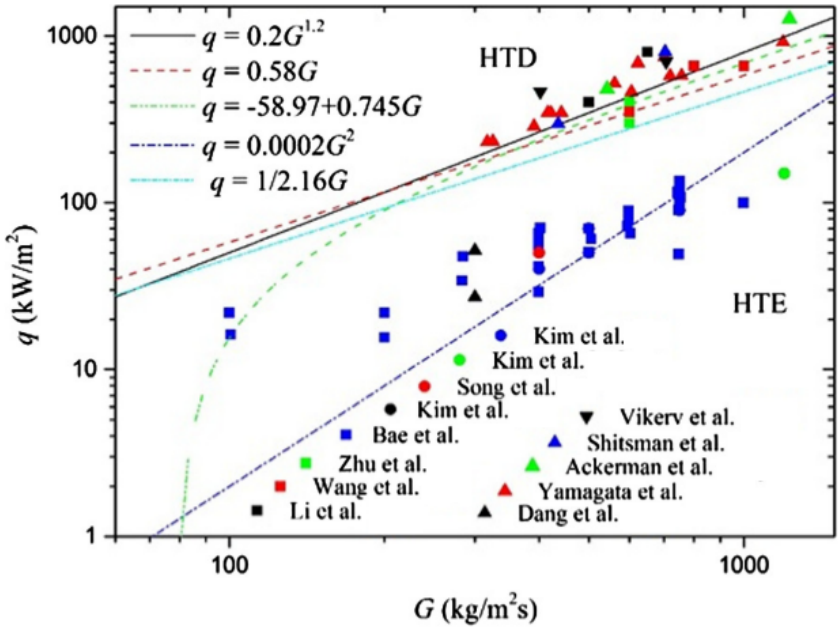

Figure 2.10: Various DHT criteria versus experimental data [21]

2.2.4 Influence of tube diameter

Bazargan et al. [16] also performed research on supercritical water in horizontal tubes with pressures of 23 to 27 MPa, heat fluxes up to 310 kW/m^2, mass fluxes ranging from 330 to 1230 kg/(m^{2}s) and an inner tube diameter of 6.3 mm. They found similar results as Yu et al. [17] (who performed experiments with inner tube diameters of 26 and 43 mm), which can be seen in Figures 2.11 and 2.12. The heat transfer coefficients are again highest at the bottom side around the pseudocritical temperature, so IHT is visible at the bottom while DHT is present at the top. Also, these temperature differences between top and bottom disappear at higher bulk enthalpies/temperatures.

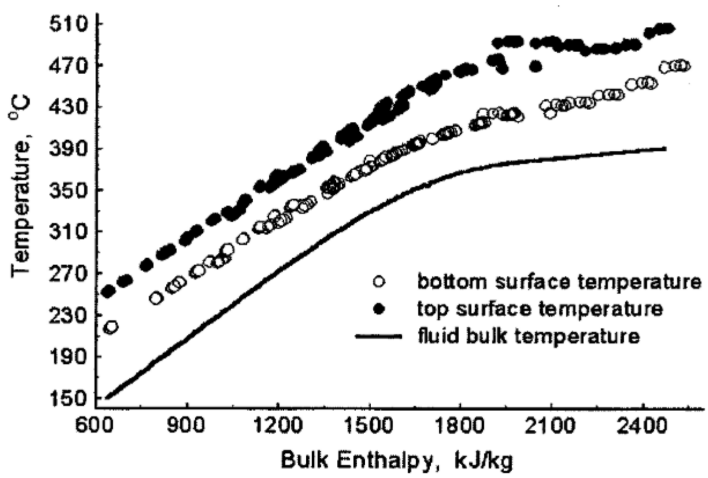

Figure 2.11: Top, bottom and bulk temperatures measured by Bazargan et al. [16]

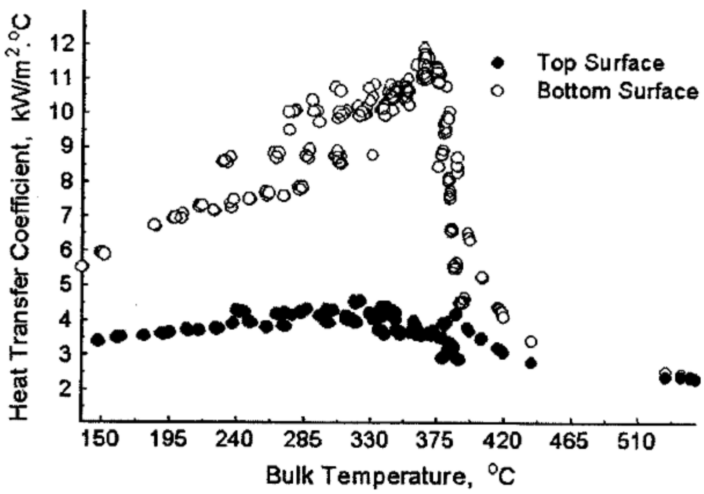

Figure 2.12: Heat transfer coefficients measured by Bazargan et al. [16]

For a pressure of 24.4 MPa, a mass flux of 340 kg/(m^{2}s) and a heat flux of 297 kW/m^2, temperature differences between top and bottom are only 30°C. This is much lower than the differences in Figure 2.2. When considering the similar testing conditions (except for the mass flux, which is lower in this case), this leads to the conclusion that the buoyancy effect is more effective in larger tube diameters. If this would not be the case, higher temperature differences would be observed in the research of Bazargan et al. since the mass flux is lower. However, the opposite is true.

Research by Tian et al. [25] investigated the effects of tube size on the heat transfer to supercritical R134a in ORC applications for diameters of 10.3 and 16 mm. It was concluded that for small ratios of the heat flux to the mass flux $\dot{q}/G$, the tube diameter hardly influences the wall temperatures and heat transfer coefficients. However, when $\dot{q}/G$ has higher values a larger tube diameter leads to larger temperature differences between top and bottom of the tube. This leads to the conclusion that larger tube diameters are more susceptible to buoyancy effects, given that the value of $\dot{q}/G$ is high enough. The reason for this $\dot{q}/G$ factor can be explained by the influence of heat and mass flux as described above. When $\dot{q}$ is large or G is small (and thus $\dot{q}/G$ is large), larger buoyancy effects are observed and vice versa.

2.2.5 Overview of influences

Provided all the information above, buoyancy effects become more dominant at low mass fluxes, high heat fluxes and large tube diameters for heat transfer to supercritical fluids in horizontal tubes. When no significant buoyancy effects are observed, only forced convection takes place. Otherwise, both forced and natural convection are present [21, 26]. An overview of the different influences is given in Table 2.1.

When buoyancy effects are negligible, increased heat transfer coefficients around T_{pc} are due to the favourable combination of thermophysical properties such as the peak in specific heat capacity. As these properties show less strong variations for higher pressures, these effects become less strong at supercritical pressures further away from p_c.

When buoyancy effects are not negligible, mass flux, heat flux, tube diameter and pressure have a large influence on the heat transfer coefficients. In this case, heat transfer behaviour is much more complex. For higher values of $\dot{q}/G$, differences in temperature and heat transfer coefficients between top and bottom of the tube can be seen. This leads to DHT at the top and IHT at the bottom. When using high heat fluxes, heat transfer coefficients tend to increase as the mass flux increases. At lower heat fluxes, increased mass fluxes do not always provide better heat transfer behaviour. Smaller tube diameters are less susceptible to buoyancy effects than larger diameter tubes. Comparing different experimental results on the influence of pressure can lead to contradictory results.

Table 2.1: Overview of HTC influences

tube	mass and heat flux	pressure	buoyancy effects
small	HTC increases with G and decreases with $\dot{q}$.	IHT at and around T_{pc}, peaks becomes smaller for larger pressures. NHT away from T_{pc}.	Not present, negligible or small.
large	HTC differences observed between top and bottom, difference bepending on value of $\dot{q}/G$.	Still IHT at and around T_{pc} but contradictory results. However, HTC peaks seem to also decrease for higher pressures mostly.	Heavily influence T_w and HTC differences over circumference. DHT at top of tube and IHT at bottom.

2.3 Heat transfer correlations

In the previous century, many forced convection heat transfer correlations were developed. Most empirical correlations for supercritical heat transfer were developed with water, CO_2 or helium as a fluid [14]. Many are variations on the Dittus-Boelter or Gnielinski correlations [27–29].

The Dittus-Boelter correlation [30] was developed in 1930 and expresses the bulk Nusselt number as a function of the bulk Reynolds number and bulk Prandtl number:

$$Nu_b = 0.023 \cdot Re_b^{0.8} \cdot Pr_b^n \tag{2.3}$$

Where n=0.4 when the flow is heated and 0.3 when cooled. It was developed for single-phase subcritical heat transfer and is supposed to be valid in the range $0.6 \leq Pr_b \leq 160$, $Re_b \geq 10^4$ and $L/D \geq 10$.

The correlation proposed by Gnielinski [31] in 1976 also depends on the bulk Reynolds and bulk Prandtl number and is supposed to be valid in the range $10^4 \leq Re_b \leq 5 \cdot 10^6$ and $0.5 \leq Pr_b \leq 2000$:

$$Nu_b = \frac{(f/8)(Re_b - 1000)Pr_b}{1 + 12.7(f/8)^{0.5}(Pr_b^{2/3} - 1)} \tag{2.4}$$

$$f = (0.79 \cdot ln(Re_b) - 1.64)^{-2} \tag{2.5}$$

This is an adaptation of the correlation of Petukhov and Kirillov developed in 1958 [32] to cover a wider range of flow conditions with equal or better accuracies [33]. The Gnielinski correlation was also not developed for supercritical conditions specifically.

Often, correlations of these types include one or more correction factors to account for the temperature difference between the fluid at the walls and the bulk fluid. An example is the correlation of Sieder and Tate [34] from 1936 which is a Dittus-Boelter type correlation multiplied with a factor $(\frac{\mu_b}{\mu_w})^{0.14}$, the ratio of dynamic viscosity at the bulk and wall temperatures. Other correlations may use ratios of density, temperature, Prandtl number, specific heat capacity, thermal conductivity etc. as correction factors. Note that when using these type of corrections, determining the Nusselt number/heat transfer coefficient becomes iterative.

2.3.1 Supercritical heat transfer correlations

In this section, some heat transfer correlations developed for use under supercritical conditions will be given. This overview is based on the work by Pioro and Duffey [14], Chen et al. [27], Pioro et al. [28] and Bazargan [33].

In 1957, Bringer and Smith [35] were among the first to investigate heat transfer to supercritical water and CO_2 in circular tubes. They concluded that existing empirical correlations were inadequate for use under supercritical conditions and developed their own Dittus-Boelter type correlation with a different factor for water and CO_2. In the same year, Miropolski and Shitsman [36] investigated supercritical heat transfer to water and CO_2 in vertical tubes and developed the following correlation, with $\mathrm{Pr_{min}}$ the smaller value of $\mathrm{Pr_b}$ and $\mathrm{Pr_w}$:

$$Nu_b = 0.023 \cdot Re_b^{0.8} \cdot Pr_{min}^{0.8} \tag{2.6}$$

The main difference with other Dittus-Boelter type correlations is that not necessarily the bulk Prandtl number is used. Also, this correlation is only supposed to be valid for Prandtl numbers around one.

In 1959, Krasnoshchekov and Protopopov [37] proposed a new correlation for supercritical water and CO_2. They extended the correlation of Petukhov and Kirillov [32] to include ratios of the viscosity, thermal conductivity and specific heat capacity. It leads to good predictions with accuracies up to ±15% for 85% of their available data [38]. In this correlation, $\bar{c}_p$ is the average heat capacity between wall and bulk temperatures.

$$Nu_b = Nu_{0,b} \left(\frac{\mu_w}{\mu_b}\right)^{0.11} \left(\frac{\lambda_b}{\lambda_w}\right)^{-0.33} \left(\frac{\bar{c}_p}{c_{p,b}}\right)^{0.35} \tag{2.7}$$

$$\bar{c}_p = \frac{h_w - h_b}{T_w - T_b} \tag{2.8}$$

In the 1960s, buoyancy effects were first studied by Shitsman [19] in supercritical water flowing in a horizontal tube. Top and bottom temperatures were measured, and differences up to 250°C were observed. A criterion for the influence of buoyancy was proposed, but no other empirical data was available for verification.

In the beginning of the 1970s, Belyakov et al. [39] compared vertical and horizontal flows under similar conditions. As expected, in the horizontal tube, IHT was present at the bottom and DHT at the top. For the vertical flow, heat transfer coefficients were between the values for horizontal flow. Later, these results were confirmed by Yamagata et al. [13].

In 1976, Adebiyi and Hall [40] studied heat transfer to CO_2 in a horizontal tube with a large tube diameter and focused on the buoyancy effects. Temperature differences were measured between top and bottom of the tube for a wide range of mass flows and heat fluxes. They compared existing criteria for negligible buoyancy effects to their experimental data and found that they were not accurate.

Starting in the late 1970s, Jackson et al. [41] combined experimental results with theoretical results. Available correlations were compared to the empirical data. They proposed new correlations of the Dittus-Boelter type with a correction factor based on the density difference between wall and bulk fluid.

In the 1980s and later, many more new correlations were developed for water and CO_2 with increasing complexity for the correction terms. The definition of these terms can include T_w, T_{pc}, T_b, Prandtl numbers based on average wall and bulk temperatures, Grashof numbers, numerical constants and various adjusted friction factors. Still, most of them resemble the Dittus-Boelter or Gnielinski form. In addition, these newer correlations are often developed for use of a specific fluid under certain (narrow) boundary conditions (flow geometry, Reynolds number, heat flux, mass flux, Prandtl number, pressures and temperatures) only. Research on the supercritical heat transfer phenomena to organic fluids is only found in the last decade.

2.4 Heat transfer to supercritical refrigerants

As previously mentioned, less research is available in literature for supercritical heat transfer in refrigerants compared to water and CO_2. The research found is discussed in this section.

2.4.1 R134a

Experimental research by Zhao and Jiang [42] was done on supercritical in-tube cooling heat transfer of R134a (T_c=101°C and p_c=4.06 MPa [15]). A horizontal tube with an inner diameter of 4.01 mm was used. Mass fluxes varied between 70 and 405 kg/(m^2s) and pressures varied between 4.5 and 5.5 MPa. Results of the heat transfer coefficients can be seen in Figure 2.13.

Wall temperatures and pressures were measured to obtain these results. Using the LMTD method and expressions of heat transfer resistances, a value for the convective heat transfer coefficient of the refrigerant was obtained. As expected, higher mass fluxes result in higher heat transfer coefficients, especially around the pseudocritical temperature. Also the effect of pressure can be seen. When the bulk temperature is far from T_{pc} only small variations in heat transfer coefficients are seen, which can be explained by the fact that the thermophysical properties do not vary much between different pressures. The opposite holds when the bulk temperature is near T_{pc}. Then the pressure has a clear effect on the heat transfer coefficients: lower pressures lead to higher values. This can be explained by the fact that the peak in specific heat capacity is greater for lower pressures (and correspondingly for lower pseudocritical temperatures).

The results were compared to existing heat transfer correlations of the Dittus-Boelter and Gnielinski type with correction terms based on physical properties. No correlation for R134a was available, so correlations based on other fluids had to be used. An example is shown in Figure 2.14. Most correlations predict the convection coefficients fairly good if the bulk temperature is below T_{pc} while at larger temperatures they deviate more. Based on all the data, the correlation of Gnielinski predicted the heat transfer coefficients best although it was developed for subcritical single-phase heat transfer. In most cases, measured values lied within ±25% of the predicted values. The other correlations, based on CO_2, overestimated the experimental values.

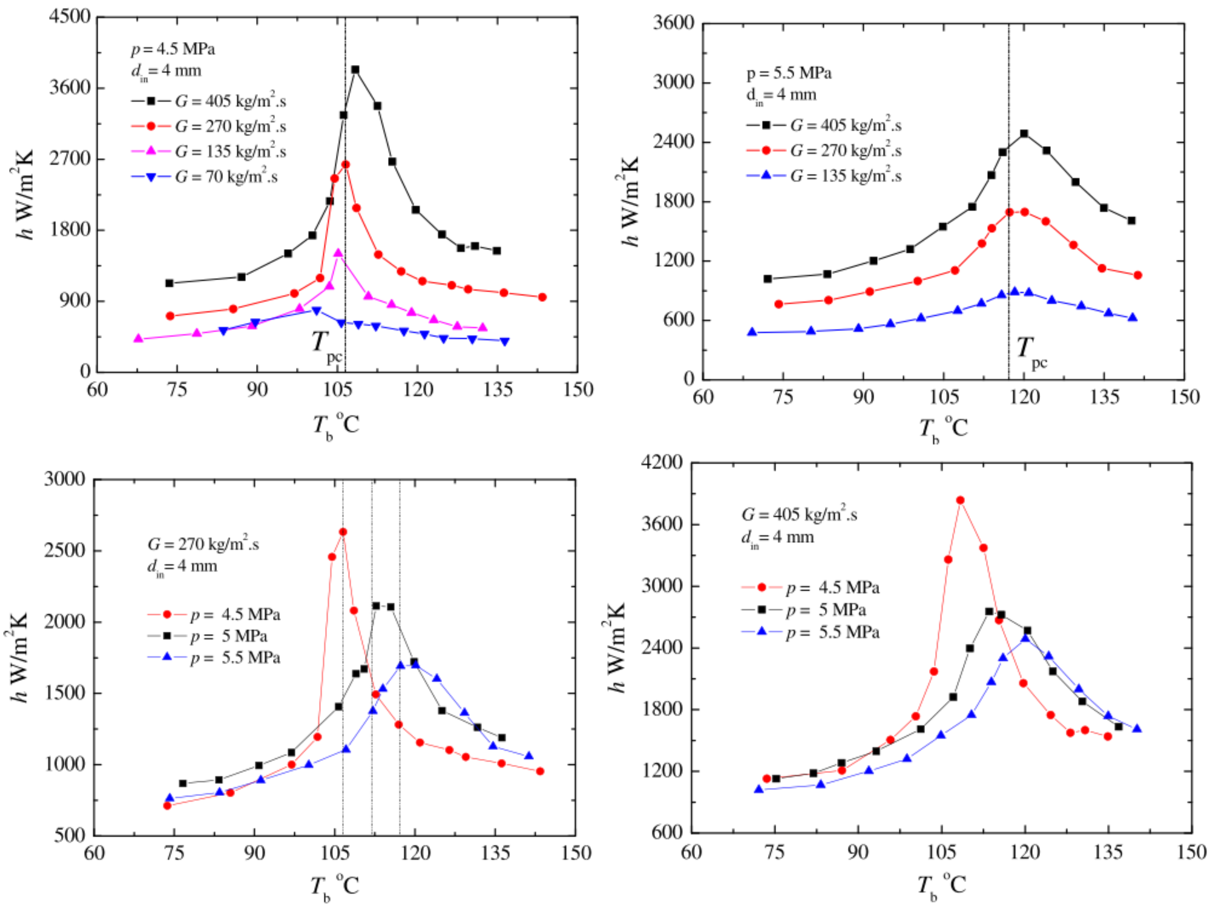

Figure 2.13: Heat transfer coefficients measured by Zhao and Jiang [42]

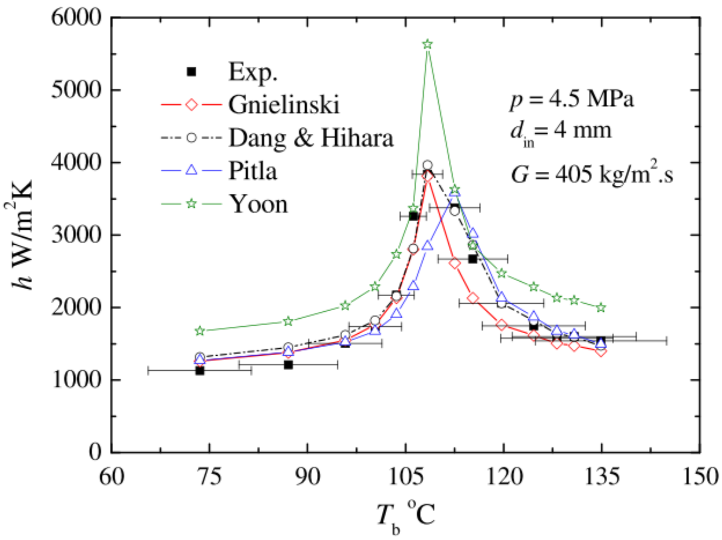

Figure 2.14: Comparison of measured heat transfer coefficients and different correlations [42]

A new correlation was developed based on the experimental work. It is based on the Gnielinski correlation and includes correction terms:

$$Nu_0 = \frac{(f/8)(Re_b - 1000)Pr}{1.07 + 12.7(f/8)^{0.5}(Pr^{2/3} - 1)} \left(1 + \left(\frac{d}{L}\right)^{2/3}\right) \tag{2.9}$$

$$f = (1.82 \cdot log(Re_b) - 1.64)^{-2} \tag{2.10}$$

$$Nu = Nu_0 \cdot 0.93 \left(\frac{Pr_w}{Pr_b}\right)^{-0.11} \left(\frac{\bar{c}_p}{c_{p,b}}\right)^{0.96} \left(\frac{\rho_w}{\rho_b}\right)^{1.06} \text{for } T_b \leq T_{pc} \tag{2.11}$$

$$Nu = Nu_0 \cdot 1.07 \left(\frac{T_w}{T_b}\right)^{-0.45} \left(\frac{\bar{c}_p}{c_{p,b}}\right)^{0.61} \left(\frac{\rho_w}{\rho_b}\right)^{-0.18} \text{for } T_b > T_{pc} \tag{2.12}$$

Over 90% of the measured data lies within ±15% of this correlation. It is supposed to be valid for the cooling of supercritical R134a under the tested conditions only.

Heat transfer to supercritical R134a was also investigated by Wang et al. and Tian et al. [43–46]. In a first study [43] the supercritical heat transfer characteristics were studied in a horizontal tube with a diameter of 10.3 mm. Pressures ranged between 1.02 x p_c and 1.2 x p_c, mass flux between 400 and 1500 kg/(m^{2}s) and heat flux between 20 and 100 kW/m^2. They observed DHT at the top of the tube for values of $\dot{q}/G$ above a certain threshold while IHT was always present at the bottom of the tube. The pressure only influenced heat transfer coefficients at the bottom of the tube, not at the top. The experimental results were compared to various existing heat transfer correlations but none of them predicted the results accurately. Two new Dittus-Boelter type correlations were proposed, one for the top of the tube and one for the bottom. In these correlations, the bulk Nusselt number is a function of the bulk Reynolds number, Prandtl number evaluated at the average wall and bulk temperatures and ratio of density at wall and bulk conditions.

Wang et al. [44] also performed experimental measurements on supercritical heat transfer to R134a in a horizontal microfin tube. This tube had a heated length of 2.5 m and a hydraulic diameter of 7.85 mm. Wall temperatures were measured at multiple locations along the test section. At some places, six thermocouples were placed along the whole tube circumference while only four were used in other locations only on one side of the tube. Pressures varied between 1.05 x p_c and 1.23 x p_c, mass flux between 100 and 700 kg/(m^{2}s) and heat flux between 10 and 70 kW/m^2. Increased heat flux resulted in lower heat transfer coefficients at the same pressure and mass flux. However, the magnitude of the reduction depended on the heat fluxes: increasing $\dot{q}$ from 40 to 50 kW/m^2 decreased the heat transfer coefficients much more than increasing the heat flux from 50 to 60 kW/m^2. The effect of pressure was the same as expected in smooth tubes: heat transfer coefficient peaks decrease for higher pressures. Again, new heat transfer correlations were developed for top and bottom side of the tube. In these correlations, the bulk Nusselt number is a function of the bulk Reynolds number, Prandtl number evaluated at the average wall and bulk temperatures, heat flux, mass flux, thermal expansion coefficient, hydraulic diameter, axial tube location and the ratio of density and specific heat capacity at wall and bulk conditions. Average deviations for the Nusselt number between measurements and the proposed correlation at the top of the tube were 10.3% and 17.8% for the bottom. Deviations between correlation and experiments smaller than 30% were present in 96.1% of the measurements for the top of the tube and 83.8% for the bottom.

Later, the results of the smooth and microfin tube were compared [45]. In Figure 2.15 the differences between wall temperatures and heat transfer coefficients can be seen for the smooth tube (labelled ST) and microfin tube (labelled MFT) for two different heat fluxes. In both cases, temperature differences increase at higher heat fluxes. Also, wall temperatures and temperature differences between top and bottom are significantly lower in the microfin tube, leading to higher heat transfer coefficients. In addition, the peak in heat transfer coefficients is more pronounced for the microfin tube, even for lower heat fluxes.

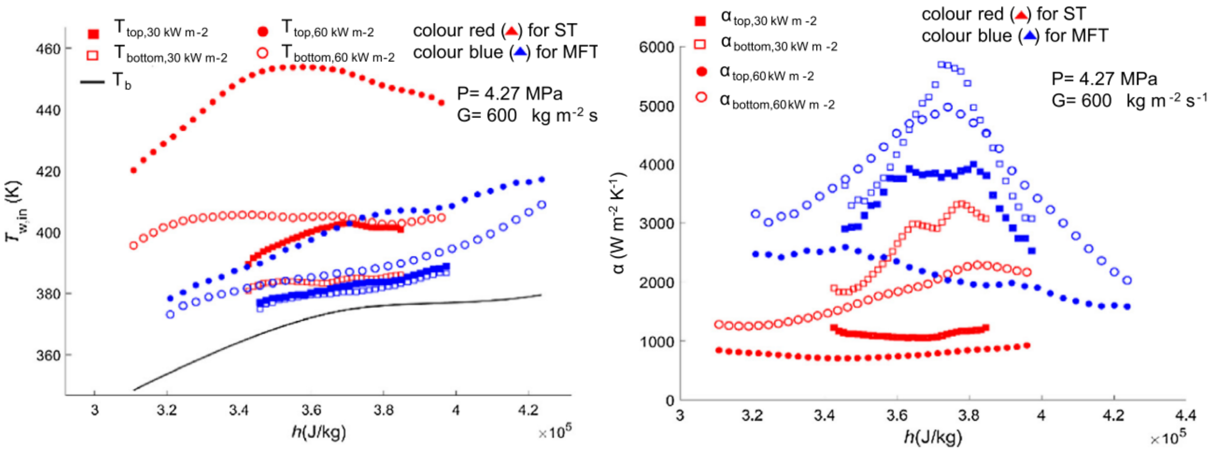

Figure 2.15: Wall temperatures (left) and heat transfer coefficients (right) for different heat fluxes in a smooth and microfin tube by Wang et al. [45]

Figure 2.16 shows the same plot, but for variable pressure and a constant heat flux. For the microfin tube, wall temperatures increase slightly with an increased pressure. This is not the case for the smooth tube, where temperatures remain more or less constant. When looking at the heat transfer coefficients, again the values are higher for the microfin tube. Even the lowest measurements of the HTCs at the top of the microfin tube are in the same range of the maximum values at the bottom of the smooth tube. Differences in heat transfer coefficients for the smooth tube are almost non-existent for both pressures while the peak increases significantly for the microfin tube. This concludes that microfin tubes are preferred since they are less susceptible to detrimental buoyancy effects.

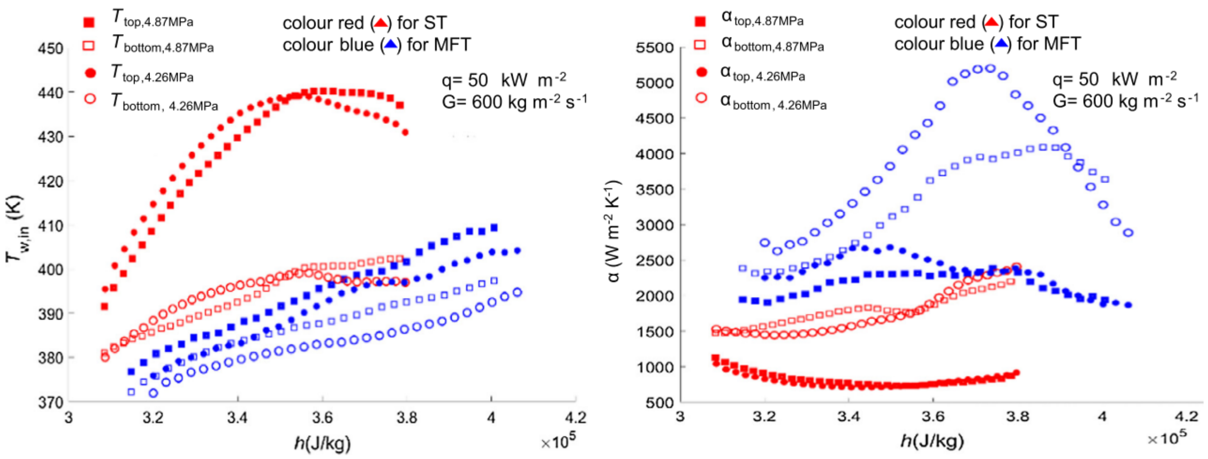

Figure 2.16: Wall temperatures (left) and heat transfer coefficients (right) for different pressures in a smooth and microfin tube by Wang et al. [45]

2.4.2 R410a and R404a

Garimella [47] and Garimella et al. [48] investigated sub- and supercritical cooling of R410a (a mixture of R32 and R125, T_c=71°C and p_c=4.9 MPa [15]) and R404a (a mixture of R125, R143a and R134a, T_c=72°C and p_c=3.7 MPa [15]). Experimental measurements were done using tubes with an inner diameter of 0.76, 1.52, 3.05, 6.2 and 9.4 mm for R410a while only one inner diameter of 9.4 mm for R404a was tested. Mass fluxes varied between 200 and 800 kg/(m^2s). Supercritical pressures were chosen to be p_c, 1.1 x p_c and 1.2 x p_c. Local heat transfer coefficients and pressure drops were measured. In this work three regions are defined: the liquid-like, pseudocritical and gas-like. For all three pressures and both refrigerants, temperatures were chosen to determine the boundaries between these regimes.

For the heat transfer coefficients of R410a, peaks were clearly visible around the pseudocritical temperature, as expected. Some results are presented in Figure 2.17. For the three tube diameters shown, this peak was highest for the lowest pressure p_c and lowest for the highest pressure 1.2 x p_c. Also, the smaller the tube diameter the higher this peak in heat transfer coefficients for all mass fluxes. Larger peaks were seen for higher mass fluxes, caused by larger Reynolds numbers. For the heat transfer coefficients of R404a, measurements were only done on the largest tube diameter. Results also showed higher heat transfer coefficients for higher mass fluxes and lower values for higher pressures.

In Figure 2.18, the experimental Nusselt numbers as a function of the bulk Reynolds number are presented. It can be seen that for lower temperatures and Reynolds numbers, Nusselt numbers are strongly dependent on the tube diameter and even show a peak for the smallest tube diameter. Garimella et al. presume this is because gravitational effects are less significant in smaller tube diameters so denser fluid surrounds the bulk flow (as this is cooling heat transfer). This increases the heat transfer because of the higher thermal conductivity at lower temperatures, see also Figure 2.1. Larger tube diameters would lose this effect. For higher temperatures, the Nusselt number varies much less between tube diameters.

A new correlation was proposed based on the Nusselt number correlation by Churchill [49], including the bulk Reynolds number, bulk Prandtl number and modified friction factor. In addition, to account for the higher Nusselt number at small diameters and lower Reynolds numbers an extra factor based on the bulk Reynolds number was included.

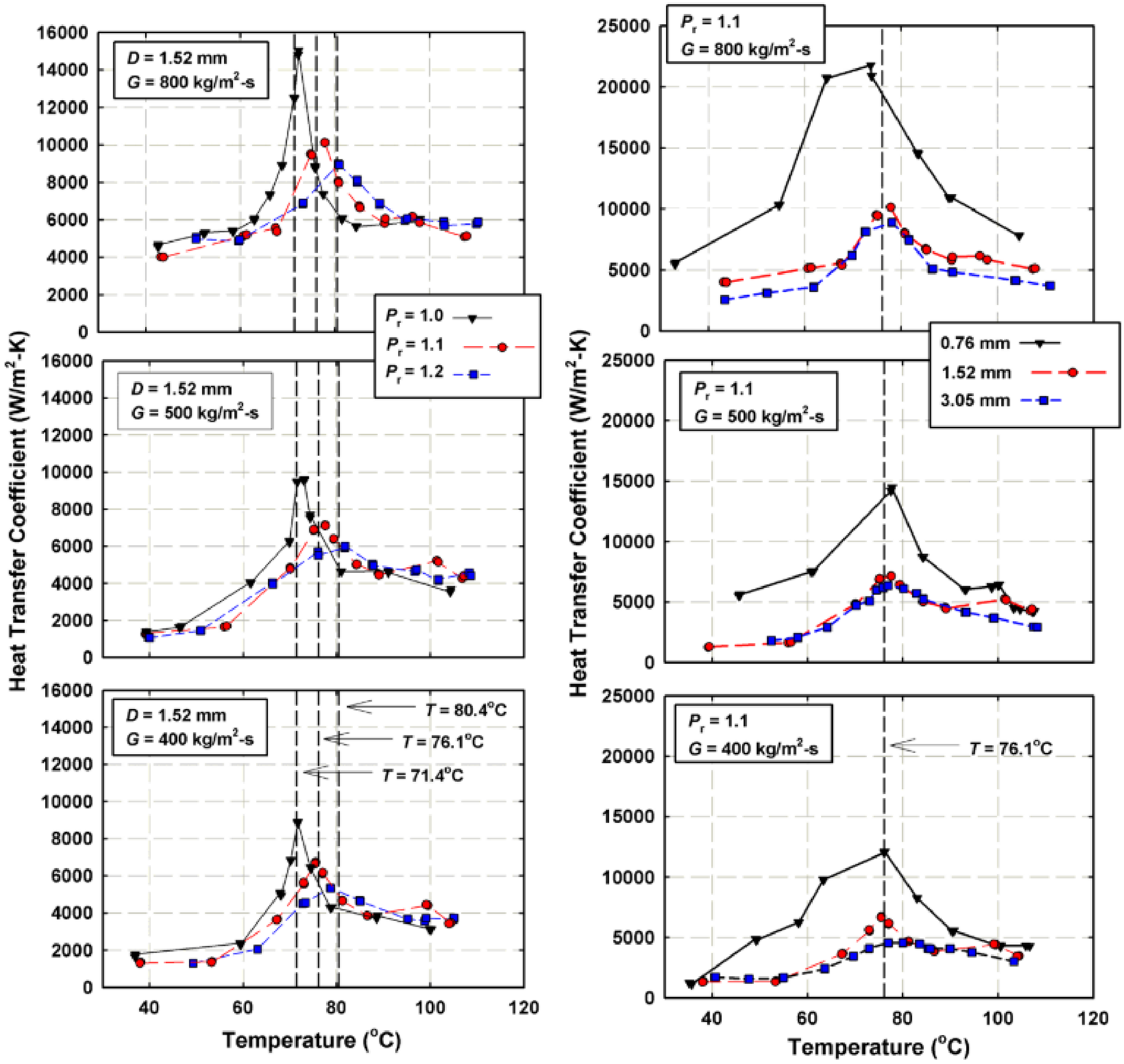

Figure 2.17: Effect of pressure (left) and diameter (right) on heat transfer coefficients for different mass fluxes by Garimella [47]

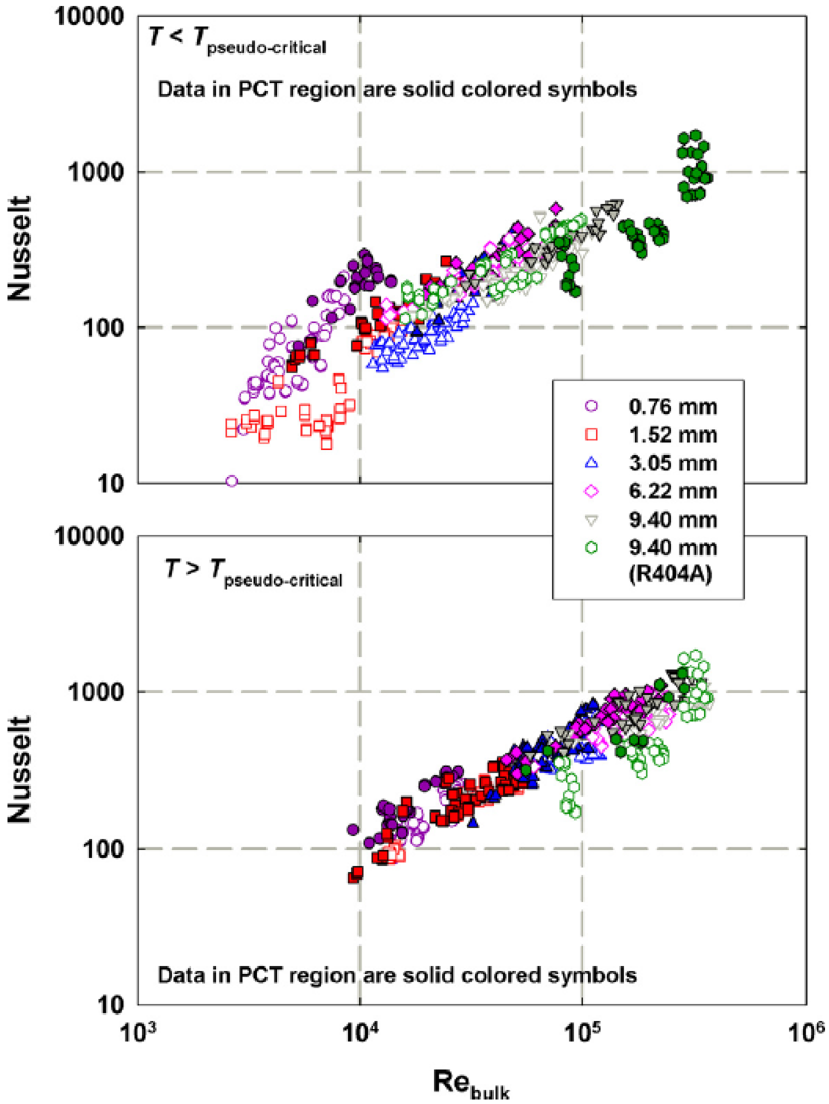

Figure 2.18: Experimental Nusselt numbers as a function of bulk Reynolds number by Garimella [48]

2.4.3 R125

Lazova et al. [50, 51] investigated supercritical heat transfer to R125 (T_c=66°C and p_c=3.6 MPa [15]) in a horizontal tube with a large tube diameter under supercritical ORC conditions. A tube-in-tube heat exchanger with a length of 4 m was used, with thermal heating oil in the annulus and refrigerant in the inner tube. Refrigerant temperatures were measured at 11 equally spaced locations in the inner tube in order to obtain local heat transfer measurements. Results are presented in Figure 2.19. For these measurements the inlet temperature of R125 was set to 60°C, the inlet temperature of the heat source (thermal oil) to 100°C, heating fluid mass flow rate to 2 kg/s and refrigerant mass flow rate to 0.19, 0.25 and 0.30 kg/s. Experiments were performed in steady-state operation various supercritical pressures.

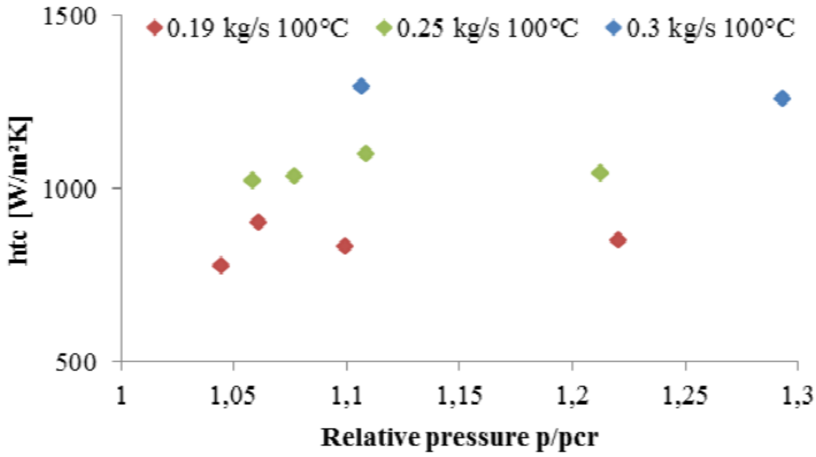

Figure 2.19: Heat transfer coefficient measurements by Lazova et al. [51]

The data presented in this graph are the convection coefficients at the refrigerant side over the whole tube-in-tube heat exchanger length. The influence of the refrigerant pressure is not clear from the data. However, higher refrigerant mass flow rates result in larger convection coefficients. The latter is in accordance with the conclusion of section 2.2.3.

2.5 Goal of this thesis

Only a limited amount of heat transfer correlations for heat transfer to refrigerants flowing in horizontal tubes at the supercritical state are found in literature. In addition, these correlations are often only valid under the same conditions as tested by the authors and can lead to contradictory results. Therefore, additional research is required. In this thesis, supercritical heat transfer to R125 will be studied experimentally. This is done on a transcritical ORC setup at Ghent University built in the previous years. The work by Lazova et al. [50, 51], described in section 2.4.3, was performed on this setup. The component of interest is the vapour generator, a counterflow tube-in-tube heat exchanger, which is rigged with measurement equipment to determine local heat transfer coefficients to R125 at multiple locations in the tube. An adapted version of the setup will also be proposed to obtain more accurate results in the future and to have the ability of testing other low GWP refrigerants, as the research found in literature is often for high GWP refrigerants.

Chapter 3

Setup description

This chapter handles the description of the measurement setup iSCORe and all measuring equipment. The setup was designed by Lazova et al. [50]. A schematic overview of the setup can be seen in Figure 3.1 and the setup itself in Figure 3.2. It consists of three main loops: the heating, refrigerant and cooling loop.

3.1 Working fluid loop

The working fluid loop containing R125 is the main part of the setup and is depicted centrally in Figure 3.1. This loop simulates the heat transfer to the working fluid in a transcritical ORC. The expander, which is normally present in an ORC to extract work, is replaced by an expansion valve. This is because the heat transfer phenomenon in the vapour generator is studied so other components are of less interest. R125 (C_2HF_5) is an organic fluid with a critical pressure of 3.6 MPa and a critical temperature of 66°C, which makes it a suitable working fluid for low temperature waste heat recovery at the supercritical state.

3.1.1 Components

First, the working fluid is pressurized by the pump to a pressure above the critical pressure. A Hydra-Cell G15 diaphragm pump is used which is a volumetric pump. However, it has five diaphragms to ensure a steady mass flow rate and outlet pressure and is equipped with an oil cooler. The pressure at the pump inlet is limited to 35 bar maximum and the cooling oil temperature limited to 80°C maximum. The speed of the motor driving the pump is inverter controlled.

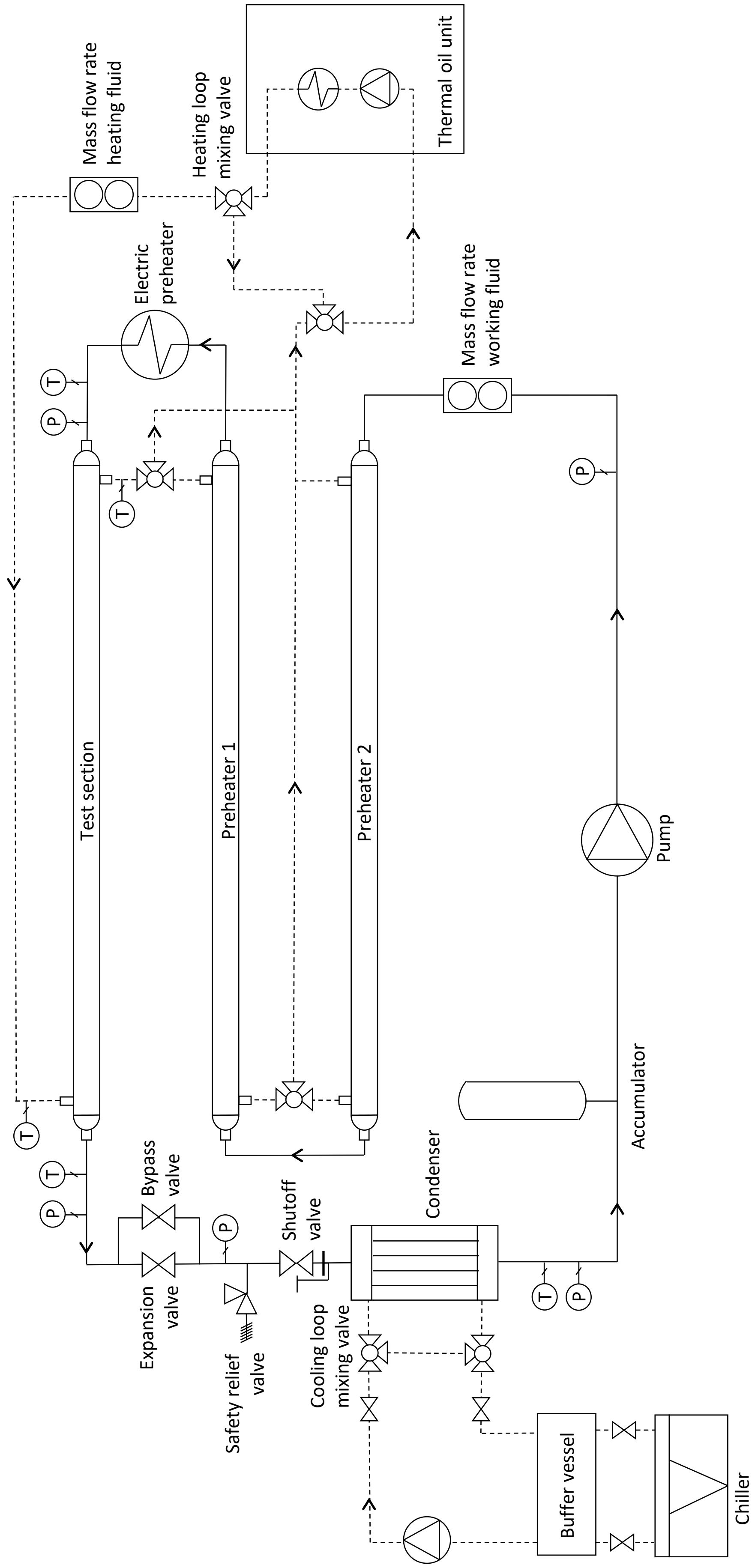

Figure 3.1: Schematic overview of test setup

Figure 3.2: Test setup

After pressurization, the refrigerant is preheated using two tube-in-tube preheaters and a Vulcanic electric in-line preheater. By using these preheaters the refrigerant can be conditioned to the right temperature at the test section inlet, so that heat transfer coefficients can be measured at temperatures of interest. The tube-in-tube preheaters are counterflow heat exchangers with the refrigerant flowing in the inner tube and the thermal oil (part of the heating loop) flowing in the annulus. Their use is optional so either no, one or two preheaters are used. The electric preheater is included in the setup because it allows for a PID controlled temperature of the refrigerant at the electric preheater outlet. This makes controlling the temperature of the refrigerant at the inlet of the test section possible.

The geometry and materials of the test section are shown in Table 3.1. It is a horizontal counterflow tube-in-tube heat exchanger with the refrigerant flowing in the inner tube and the thermal oil in the annulus. The layout is the same as the tube-in-tube preheaters except for the fact that the test section is equipped with measurement equipment. The outer tube walls are sufficiently insulated to ensure minimal heat losses to the environment. Before the inlet, fully developed flow is ensured by a horizontal piece of tubing of length 1 m which is not heated.

After the test section, the refrigerant passes an expansion valve. This Danfoss valve causes a pressure drop in the refrigerant circuit. The opening of the valve can be controlled electronically. A bypass valve, which is on/off controlled, is placed in parallel with the expansion valve. After this section,, a pressure relief valve and shut-off valve are placed. The bypass valve, safety relief valve and shut-off valve are all needed for safety reasons.

After expansion, the refrigerant passes the condenser, which is an Alfa-Laval plate heat

Table 3.1: Test section specifications

	Length	4 m
Inner tube	Material	Copper
	λ_w	260 W/m/K
	d_i	0.02477 m
	d_o	0.02857 m
Outer tube	Material	Galvanised steel
	D_i	0.0530 m
	D_o	0.0603 m

exchanger. The condenser is connected to the cooling loop which acts as a heat sink.

Finally, before the refrigerant returns to the inlet of the pump to close the cycle, an accumulator is included. As the working fluid loop is filled with a fixed amount of refrigerant, volumetric expansion or contraction will be present when changing operating conditions. This is accounted for by the accumulator which consists of pressurized nitrogen and the working fluid separated by a diaphragm.

3.1.2 Limitations

All components and measurement devices have limits on the operating pressures and temperatures. In the high pressure part, from pump outlet until expansion valve, pressures cannot exceed 50 bar and temperatures are limited to 120°C. In the low pressure part, from expansion valve until pump inlet, pressures cannot exceed 35 bar and temperatures are limited to 80°C.

3.2 Heating loop

The heating loop contains Therminol ADX10 thermal oil which acts as the heat source for the cycle. In Figure 3.1 it is represented with dotted lines.

3.2.1 Components

First, the thermal oil is heated in the electric Vulcanic thermal heater. It has a capacity of 20 kW and allows outlet oil temperatures of up to 180°C. It also includes a circulation pump for the heating loop with a fixed flow rate. The oil leaving the thermal heater passes a three way valve (heating loop mixing valve) controlled by the user. It bypasses some of the oil and brings it back to the thermal oil unit. Oil that is not bypassed enters the test section. This allows for easy flow rate control through the test section. After the test section the oil either flows back to the thermal oil unit or passes the preheaters, depending on how many tube-in-tube preheaters are used.

3.2.2 Limitations

The maximum oil temperature is limited by the heating loop mixing valve to a maximum of 130°C. A maximum pressure is of no importance since the oil is just circulated in the heating loop.

3.3 Cooling loop

The cooling loop contains a water/glycol (70/30%) mixture and is represented by dotted lines in Figure 3.1. Temperatures below 0°C can be reached and the cooling loop acts as a heat sink for the cycle by passing through the condenser.

3.3.1 Components

A circulation pump provides a fixed mass flow rate through the loop. Just as in the heating loop, a three way valve (cooling loop mixing valve) allows for mass flow rate control through the condenser. Bypassed fluid and fluid returning from the condenser are pumped back to a 900 l buffer vessel. The temperature of the water/glycol mixture is controlled at the buffer vessel. When cooling is needed, a 37 kW chiller located at the outside provides cooling of the buffer vessel.

3.4 Measurement equipment

Pressures, temperatures and mass flow rates are measured to obtain data to calculate the refrigerant side convection coefficients. Table 3.2 provides an overview of all sensor measurements and Table 3.3 shows the accuracies of all sensor types. It is important to note that only bulk temperatures are measured.

3.4.1 Test section measurement equipment

At the oil side, Pt100 temperature sensors are placed at inlet and outlet. In between, three K-type thermocouples are spaced evenly throughout the test section at distances of 1 m. Similarly, at the refrigerant side Pt100 sensors are placed at inlet and outlet. Between these, 11 T-type thermocouples are spaced evenly at distances of 0.33 m. In addition, pressure transducers are placed at inlet and outlet. The position of the four Pt100 sensors and pressure transducers can be seen in Figure 3.1. Figure 3.3 shows a schematic overview of the test section including all temperature measurements. Red arrows indicate the thermal oil, blue arrows the refrigerant flow.

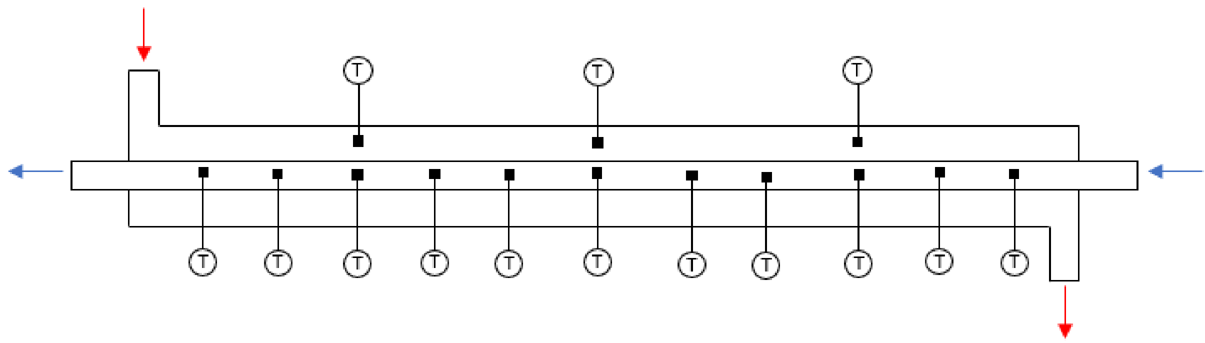

Figure 3.3: Thermocouple placement in test section

3.4.2 Other measurement equipment

The data reduction method, discussed in the next chapter, requires other measurements to be performed as well. First of all, the thermal oil mass flow rate through the test section is measured. This is done by a Rheonik RHM20 coriolis mass flow meter located at the inlet of the test section. In the working fluid loop a Rheonik RHM12 coriolis mass flow meter is placed at the outlet of the pump.

In addition to measuring mass flow rates, some pressure and temperature measurements are present in the setup. These are not required for data reduction but are needed for safety monitoring and controlling valves. Extra pressure transducers are located at the outlet of the pump, after the expansion valve and after the condenser. The latter is used to monitor the inlet pressure of the pump, which cannot exceed 35 bar. A Pt100 sensor is included at this location as well to measure subcooling at the pump inlet to ensure that the refrigerant enters the pump in the liquid state only, avoiding cavitation. This temperature should be below the refrigerant saturation temperature. Depending on this temperature difference, the cooling loop mixing valve can be opened or closed to change the cooling loop mass flow rate through the condenser, and thus to regulate the amount of subcooling.

3.4.3 Data acquisition systems

All thermocouples are connected to a Tektronix Keithley 2700 series data acquisition system. A measurement time step of 10 seconds was chosen, which is about the minimum time step size since not all input contacts can be closed simultaneously. All other measurement devices (pressure transducers, mass flow meters and Pt100 sensors) are connected to NI CompactRIO modules. These modules allow for a smaller measurement time step size which was chosen to be 1 second.

Both the Keithley and CompactRIO systems are connected to a computer where they can be read by a LabVIEW program. For the temperature measurements, calibration curves are included in LabVIEW such that the output values need no corrections. Next to starting, stopping and saving measured data the program also can control the pump speed and valve positions. These controls are connected to separate CompactRIO modules. The LabVIEW program also serves as a monitoring device when the setup is running. All

Table 3.2: Overview of sensor measurements

Loop	What	Type	Name	Location
Heating	Temperature	Pt100	Pt100 #4	Outlet test section
		Pt100	Pt100 #5	Inlet test section
		TC	TC hf #1	Test section
		TC	TC hf #2	Test section
		TC	TC hf #3	Test section
	Mass flow rate	Coriolis	$\dot{m}_{hf}$	After heating loop mixing valve
Working fluid	Temperature	Pt100	Pt100 #1	Outlet test section
		Pt100	Pt100 #2	After condenser
		Pt100	Pt100 #3	Inlet test section
		TC	TC wf #1	Test section
		TC	TC wf #2	Test section
		TC	TC wf #3	Test section
		TC	TC wf #4	Test section
		TC	TC wf #5	Test section
		TC	TC wf #6	Test section
		TC	TC wf #7	Test section
		TC	TC wf #8	Test section
		TC	TC wf #9	Test section
		TC	TC wf #10	Test section
		TC	TC wf #11	Test section
	Mass flow rate	Coriolis	$\dot{m}_{wf}$	After pump
	Pressure	Transducer	P1	Outlet test section
		Transducer	P2	After condenser
		Transducer	P3	Inlet test section
		Transducer	P4	After expansion valve
		Transducer	P5	After pump

Table 3.3: Accuracies of measurement equipment

Sensor/value	Accuracy
TC T-type	0.1 K
TC K-type	0.1 K
Pt100	0.1 K
Pressure transducer	6000 Pa
Mass flow meters	1%

sensors connected to the CompactRIO modules are monitored in real time and shown on-screen.

3.4.4 Measurement testing

During test measurements it became clear that not all measurement equipment provided reliable results. The thermocouple measurements at the oil side of the test section proved to be unrealistic. An example is shown in Figure 3.4. It shows the measured values of the oil temperatures as a function of time. The inlet and outlet temperatures measured by Pt100 sensors #5 and #4 are plotted in black lines. Normally, the thermocouple measurements should lie within these boundaries and show how the temperature varies over the test section length. In Figure 3.4 it is clear that the temperatures measured by the thermocouples hardly differ from each other, which cannot be the case in reality. For this reason they were never used in the data reduction.

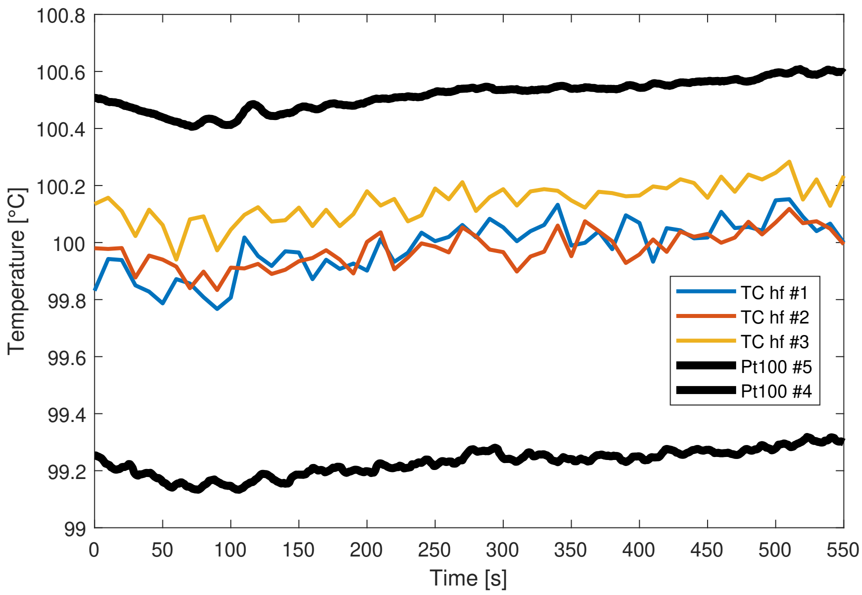

Figure 3.4: Oil temperature measurements example

The opposite is true at the refrigerant side. The Pt100 sensor measurements seem to be too low compared to the values measured by the thermocouples. This can be seen in Figure 3.5. The deviation of the temperatures measured by the Pt100 sensors can be explained by their position, shown in Figure 3.6. They are not measuring the refrigerant temperature in the bulk fluid flow but at some distance above it. Lack of sufficient insulation could explain why the measured temperatures are too low. In addition, some thermocouples provided unrealistic results. As the bulk fluid temperature is measured, the temperature should only increase along the length of the test section. However, thermocouples #3, #6 and #7 measure temperatures higher than the next thermocouples. This could be explained by their placement in the inner tube: if they are not located at the centre of the tube a higher temperature reading is to be expected since the wall temperatures are higher than the bulk refrigerant temperatures. Therefore, these measurements were never used in the data reduction. This was also the case for TC wf #2 in some measurements.

In these cases, TC wf #2 was also excluded.

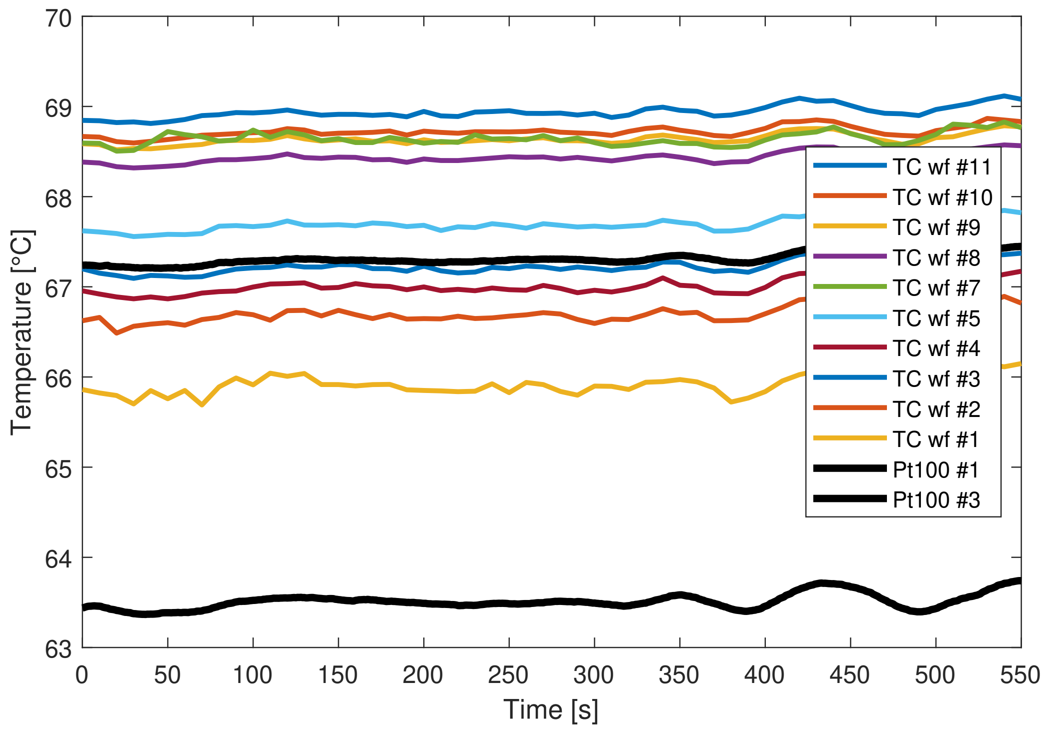

Figure 3.5: Refrigerant temperature measurements example

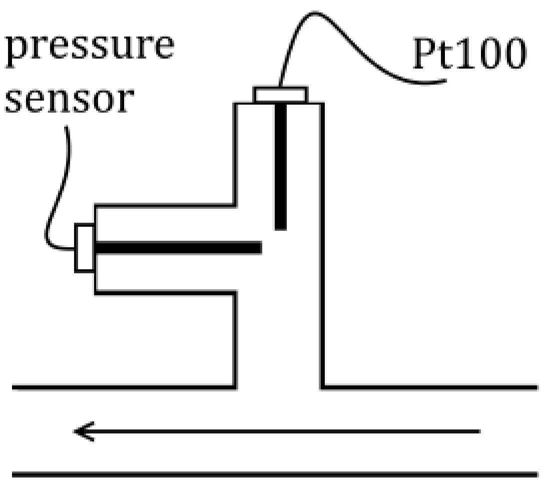

Figure 3.6: Positioning of Pt100 sensors and pressure transducers at refrigerant side

From the measurement equipment outside of the test section, Pt100 #2 (temperature refrigerant at condenser outlet) was not functioning properly. Its output showed a lag compared to the other sensors and sometimes unrealistic values. It is not clear why Pt100 #2 did not function properly.

While the malfunctioning measurement equipment described above did influence the control strategy and the data reduction method, reliable measurements could still be performed. The consequences are described in the next chapter.

Chapter 4

Data reduction and uncertainty analysis

This chapter first handles the data reduction method, starting from measured data to obtain values for the convection coefficients and Nusselt numbers at the refrigerant side. Secondly, a method for determining steady-state operation is discussed. Finally, error propagation in the data reduction is discussed.

4.1 Data reduction method

4.1.1 Determining heat transfer coefficients and Nusselt numbers

Starting from the heat exchanger geometry and measured data, the convection coefficients at the refrigerant side can be determined. First, the heat transfer rate $\dot{Q}$ and heat flux $\dot{q}_{hf}$ in the test section is determined at the oil side.

$$\dot{Q} = \dot{m}_{hf} \cdot c_{p,hf} \cdot \Delta T_{hf} \tag{4.1}$$

$$\dot{q}_{hf} = \frac{\dot{Q}}{\pi \cdot d_o \cdot L} \tag{4.2}$$

The value for the specific heat capacity $c_{p,hf}$ is given as a function of temperature by the supplier of the oil. Oil mass flow rate $\dot{m}_{hf}$ and temperature drop ΔT_{hf} are measured quantities. d_o is the outer diameter of the inner tube and L is the test section length that is heated. Note that no heat losses to the environment are taken into account. This is because an early estimation of these losses determined them to be negligible, certainly when comparing them to the uncertainties of all calculated values described further in this chapter.

As described in the previous chapter, the thermocouple measurements at the oil side of the test section proved to measure unreliable results. For this reason, the heat transfer rate $\dot{Q}$ and heat flux $\dot{q}_{hf}$ can only be determined over the whole length of the test section without any variations in between.

The outer wall temperature $T_{w,o}$ can be found as a function of the bulk oil temperature $T_{hf,b}$, heat flux $\dot{q}_{hf}$ and oil side convection coefficient h_{hf}:

$$T_{w,o} = T_{hf,b} - \frac{\dot{q}_{hf}}{h_{hf}} \tag{4.3}$$

The bulk oil temperature is measured and the heat flux is calculated in Equation 4.2. As only oil temperatures at the inlet and outlet of the test section are known, the oil temperature profile is assumed to be linear. To calculate the convection coefficient at the oil side h_{hf}, the Dittus-Boelter correlation is used, see Equation 4.4. The Reynolds number of the heating fluid Re_{hf} is calculated using the hydraulic diameter D_h, which is defined as four times the cross-sectional area of the fluid flow divided by the wetted perimeter of the cross section. Using this definition and knowing that the oil flows in the annulus of the test section results in $D_h = D_i - d_o$. D_i is the inner diameter of the outer tube and d_o is the outer diameter of the inner tube.

$$Nu_{hf} = \frac{h_{hf} \cdot D_h}{\lambda_{hf}} = 0.023 \cdot Re_{hf}^{0.8} \cdot Pr_{hf}^{0.3} \tag{4.4}$$

$$Re_{hf} = \frac{v_{hf} \cdot D_h}{\nu_{hf}} = \frac{4 \cdot \dot{m}_{hf}}{\pi \cdot \mu_{hf} \cdot (D_i + d_o)} \tag{4.5}$$

$$Pr_{hf} = \frac{\mu_{hf} \cdot c_{p,hf}}{\lambda_{hf}} \tag{4.6}$$

Values for μ, c_p and λ in the previous equations can also be found as a function of temperature in the data sheet provided by the oil supplier. They are all evaluated at bulk temperatures. Based on Equations 4.1-4.6, h_{hf} and thus $T_{w,o}$ can be determined.

In the next step, the inner wall temperature $T_{w,i}$ is calculated:

$$T_{w,i} = T_{w,o} - \frac{\dot{Q} \cdot ln(d_o/d_i)}{2\pi \cdot \lambda_w \cdot L} \tag{4.7}$$

Where the thermal conductivity of the inner tube material λ_w is given by the manufacturer. All other quantities are known.

Finally, the convection coefficient at the refrigerant side h_{wf} and corresponding Nusselt number Nu_{wf} can be calculated:

$$\dot{q}_{wf} = \frac{\dot{Q}}{\pi \cdot d_i \cdot L} \tag{4.8}$$

$$h_{wf} = \frac{\dot{q}_{wf}}{T_{w,i} - T_{wf,b}} \tag{4.9}$$

$$Nu_{wf} = \frac{h_{wf} \cdot d_h}{\lambda_{wf}} \tag{4.10}$$

In the previous equations, the bulk refrigerant temperature $T_{wf,b}$ is measured and the hydraulic diameter $d_h = d_i$ by definition. The values for λ_{wf} are obtained from the CoolProp library using the refrigerant bulk temperature and mean pressure in the test section as inputs.

4.1.2 Determining steady-state operation

To obtain reliable results, the setup should work in steady-state operation. This implies that all variables, such as mass flow rates, pressures and temperatures, have a time derivative of zero. Because all measurements are subject to uncertainties this cannot be verified directly. Therefore a procedure described by Lecompte et al. [52] is used. It consists of the following steps:

1. Manually identify a zone that represents steady-state operation. These results will be used as reference values.
2. Calculate the standard deviation σ_{ref} of these reference values. In this case $T_{wf,in}$, $p_{wf,in}$, $\dot{m}_{wf}$, $T_{hf,in}$ and $\dot{m}_{hf}$ were chosen as parameters of interest because these values determine the heat transfer behaviour in the test section. The standard deviations are based on 600 measurements with a time interval of one second.
3. Determine the forward-moving standard deviation σ of the parameters of interest for each point in the data that is analysed using a certain time window size.
4. Identify the steady state zones based on the following criterion:
$$\sigma \leq 2 \cdot \sigma_{ref} \tag{4.11}$$
A sample is only considered to be measured in steady-state operation if this holds for all parameters of interest.
5. Calculate the average of all points that are considered steady-state.

4.2 Uncertainty analysis

When performing measurements, the accuracy should always be taken into account. Generally speaking, a property x is measured to be x_{best} by a sensor which has an accuracy of δx. This implies that the actual value is determined to be in an interval:

$$x = x_{best} \pm \delta x \tag{4.12}$$

The propagation of these errors in the data reduction method described above can also be generalized. If a variable q is a function of variables x, y, z... with their respective errors δx, δy, δz..., the error on q can be determined by the following formula [53]:

$$\delta q = \sqrt{\left(\frac{\partial q}{\partial x}\delta x\right)^2 + \left(\frac{\partial q}{\partial y}\delta y\right)^2 + \left(\frac{\partial q}{\partial z}\delta z\right)^2 + ...} \tag{4.13}$$

Knowing the data reduction method and the way different errors propagate, the uncertainty on the calculated convection coefficients and Nusselt numbers can be determined. In the remainder of this section, all errors on the calculated values are shown.

The accuracies of the different types of sensor measurements is shown in Table 3.3. The accuracies of the different thermophysical properties used in the data reduction can be found in Table 4.1.

Table 4.1: Accuracies of thermophysical properties

$c_{p,hf}$	1 J/kg/K
μ_{hf}	0.00001 Pa·s
λ_{hf}	0.0001 W/m/K
λ_{wf}	3% [54]

Heat transfer rate

The heat transfer rate $\dot{Q}$ is shown in Equation 4.1 and its uncertainty depends on the errors of $\dot{m}_{hf}$, $c_{p,hf}$ and T_{hf}.

$$\delta\dot{Q} = \sqrt{\left(\frac{\partial\dot{Q}}{\partial\dot{m}_{hf}}\delta\dot{m}_{hf}\right)^2 + \left(\frac{\partial\dot{Q}}{\partial c_{p,hf}}\delta c_{p,hf}\right)^2 + \left(\frac{\partial\dot{Q}}{\partial T_{hf,in}}\delta T_{hf,in}\right)^2 + \left(\frac{\partial\dot{Q}}{\partial T_{hf,out}}\delta T_{hf,out}\right)^2} \tag{4.14}$$

With partial derivatives:

$$\frac{\partial\dot{Q}}{\partial\dot{m}_{hf}} = c_{p,hf}\cdot(T_{hf,in} - T_{hf,out}) \tag{4.15}$$

$$\frac{\partial\dot{Q}}{\partial c_{p,hf}} = \dot{m}_{hf}\cdot(T_{hf,in} - T_{hf,out}) \tag{4.16}$$

$$\frac{\partial\dot{Q}}{\partial T_{hf,in}} = -\frac{\partial\dot{Q}}{\partial T_{hf,out}} = \dot{m}_{hf}\cdot c_{p,hf} \tag{4.17}$$

Because of the malfunctioning thermocouples at the oil side of the test section, $(T_{hf,in} - T_{hf,out})$ is the temperature drop over the entire test section. Therefore, no variation in $\dot{Q}$ could be measured over the test section length. Using the equations described above, it can be seen that this leads to a smaller relative error on $\dot{Q}$ compared to the case where the oil side thermocouples would work well, as the temperature difference over the entire test section is larger than over a part of the section. This can also be seen in Equation 4.18. At first sight, this seems beneficial for the errors on the final results. However, this comes at the cost of assuming $\dot{Q}$ to be constant over the test section length.

$$\frac{\delta\dot{Q}}{\dot{Q}} = \frac{\delta\dot{Q}}{\dot{m}_{hf}\cdot c_{p,hf}\cdot\Delta T_{hf}} \tag{4.18}$$

Oil side Reynolds number

Equation 4.5 shows the formula for the Reynolds number at the oil side. Its uncertainty depends on the errors of $\dot{m}_{hf}$ and μ_{hf}. The tube diameters are supposed to be exactly known.

$$\delta Re_{hf} = \sqrt{\left(\frac{\partial Re_{hf}}{\partial\dot{m}_{hf}}\delta\dot{m}_{hf}\right)^2 + \left(\frac{\partial Re_{hf}}{\partial\mu_{hf}}\delta\mu_{hf}\right)^2} \tag{4.19}$$

$$\delta Re_{hf} = \sqrt{\left(\frac{4}{\pi\cdot\mu_{hf}\cdot(D_i + d_o)}\delta\dot{m}_{hf}\right)^2 + \left(\frac{-4\cdot\dot{m}_{hf}}{\pi\cdot\mu_{hf}^2\cdot(D_i + d_o)}\delta\mu_{hf}\right)^2} \tag{4.20}$$

Oil side Prandtl number

Equation 4.6 shows the formula for the Prandtl number at the oil side. Its uncertainty depends on the errors of μ_{hf}, $c_{p,hf}$ and λ_{hf}.

$$\delta Pr_{hf} = \sqrt{\left(\frac{\partial Pr_{hf}}{\partial \mu_{hf}}\delta\mu_{hf}\right)^2 + \left(\frac{\partial Pr_{hf}}{\partial c_{p,hf}}\delta c_{p,hf}\right)^2 + \left(\frac{\partial Pr_{hf}}{\partial \lambda_{hf}}\delta\lambda_{hf}\right)^2} \tag{4.21}$$

$$\delta Pr_{hf} = \sqrt{\left(\frac{c_{p,hf}}{\lambda_{hf}}\delta\mu_{hf}\right)^2 + \left(\frac{\mu_{hf}}{\lambda_{hf}}\delta c_{p,hf}\right)^2 + \left(\frac{-\mu_{hf}\cdot c_{p,hf}}{\lambda_{hf}^2}\delta\lambda_{hf}\right)^2} \tag{4.22}$$

Oil side Nusselt number

The Nusselt number at the oil side of the test section is calculated using the Dittus-Boelter correlation as shown in Equation 4.4. Its uncertainty depends on the errors of Re_{hf} and Pr_{hf}.

$$\delta Nu_{hf} = \sqrt{\left(\frac{\partial Nu_{hf}}{\partial Re_{hf}}\delta Re_{hf}\right)^2 + \left(\frac{\partial Nu_{hf}}{\partial Pr_{hf}}\delta Pr_{hf}\right)^2} \tag{4.23}$$

$$\delta Nu_{hf} = \sqrt{\left(0.0184\cdot Re_{hf}^{-0.2}\cdot Pr_{hf}^{0.3}\cdot\delta Re_{hf}\right)^2 + \left(0.0069\cdot Re_{hf}^{0.8}\cdot Pr_{hf}^{-0.7}\cdot\delta Pr_{hf}\right)^2} \tag{4.24}$$

These formulas are only valid when calculating an exact quantity. This is not the case for the Dittus-Boelter correlation however, so an extra relative error of 25% is added to the uncertainty of Nu_{hf} to account for the correlation accuracy.

Oil side convection coefficient

The error on h_{hf} depends on the errors of Nu_{hf} and λ_{hf}.

$$\delta h_{hf} = \sqrt{\left(\frac{\partial h_{hf}}{\partial \lambda_{hf}}\delta\lambda_{hf}\right)^2 + \left(\frac{\partial h_{hf}}{\partial Nu_{hf}}\delta Nu_{hf}\right)^2} \tag{4.25}$$

$$\delta h_{hf} = \sqrt{\left(\frac{Nu_{hf}}{D_i - d_o}\delta\lambda_{hf}\right)^2 + \left(\frac{\lambda_{hf}}{D_i - d_o}\delta Nu_{hf}\right)^2} \tag{4.26}$$

Outer wall temperature

Equation 4.3 shows the calculation of the outer wall temperature. Its uncertainty depends on the errors of $T_{hf,b}$, $\dot{q}_{hf}$ and h_{hf}.

$$\delta T_{w,o} = \sqrt{\left(\frac{\partial T_{w,o}}{\partial T_{hf,b}}\delta T_{hf,b}\right)^2 + \left(\frac{\partial T_{w,o}}{\partial \dot{q}_{hf}}\delta\dot{q}_{hf}\right)^2 + \left(\frac{\partial T_{w,o}}{\partial h_{hf}}\delta h_{hf}\right)^2} \tag{4.27}$$

$$\delta T_{w,o} = \sqrt{(\delta T_{hf,b})^2 + \left(\frac{-1}{h_{hf}}\delta\dot{q}_{hf}\right)^2 + \left(\frac{\dot{q}_{hf}}{h_{hf}^2}\delta h_{hf}\right)^2} \tag{4.28}$$

Inner wall temperature

In Equation 4.7 the inner wall temperature is calculated. Its uncertainty depends on the errors of $T_{w,o}$ and $\dot{Q}$. The thermal conductivity of the inner tube and its length are assumed to be exactly known.

$$\delta T_{w,i} = \sqrt{\left(\frac{\partial T_{w,i}}{\partial T_{w,o}}\delta T_{w,o}\right)^2 + \left(\frac{\partial T_{w,i}}{\partial \dot{Q}}\delta \dot{Q}\right)^2} \tag{4.29}$$

$$\delta T_{w,i} = \sqrt{(\delta T_{w,o})^2 + \left(\frac{-ln(d_o/d_i)}{2\pi \cdot \lambda_w \cdot L}\delta \dot{Q}\right)^2} \tag{4.30}$$

Refrigerant side convection coefficient

Equation 4.9 determines the convection coefficient at the refrigerant side of the test section. Its uncertainty depends on the errors of $\dot{q}_{wf}$, $T_{w,i}$ and $T_{wf,b}$.

$$\delta h_{wf} = \sqrt{\left(\frac{\partial h_{wf}}{\partial \dot{q}_{wf}}\delta \dot{q}_{wf}\right)^2 + \left(\frac{\partial h_{wf}}{\partial T_{w,i}}\delta T_{w,i}\right)^2 + \left(\frac{\partial h_{wf}}{\partial T_{wf,b}}\delta T_{wf,b}\right)^2} \tag{4.31}$$

$$\delta h_{wf} = \sqrt{\left(\frac{1}{T_{w,i} - T_{wf,b}}\delta \dot{q}_{wf}\right)^2 + \left(\frac{-\dot{q}_{wf}}{(T_{w,i} - T_{wf,b})^2}\delta T_{w,i}\right)^2 + \left(\frac{\dot{q}_{wf}}{(T_{w,i} - T_{wf,b})^2}\delta T_{wf,b}\right)^2} \tag{4.32}$$

Refrigerant side Nusselt number

Finally, the refrigerant Nusselt number is determined by Equation 4.10. Its uncertainty depends on the errors of h_{wf} and λ_{wf}.

$$\delta Nu_{wf} = \sqrt{\left(\frac{\partial Nu_{wf}}{\partial h_{wf}}\delta h_{wf}\right)^2 + \left(\frac{\partial Nu_{wf}}{\partial \lambda_{wf}}\delta \lambda_{wf}\right)^2} \tag{4.33}$$

$$\delta Nu_{wf} = \sqrt{\left(\frac{d_i}{\lambda_{wf}}\delta h_{wf}\right)^2 + \left(\frac{-h_{wf} \cdot d_i}{\lambda_{wf}^2}\delta \lambda_{wf}\right)^2} \tag{4.34}$$

Chapter 5

Experimental investigation

Experiments were performed under different operating conditions. A detailed step by step overview of the measurement procedure of the setup can be found in Appendix A. The results are discussed and compared in this chapter.

5.1 Design of experiments

Different operating conditions will result in different heat transfer coefficients. The tube diameter, heat flux, mass flux and pressure will have effects on the results as described in the second chapter. As the tube dimensions do not change, the influence of the other three parameters can be studied.

5.1.1 Proposed experimental matrix

Table 5.1 shows the proposed operating conditions in matrix form. Two pressure levels corresponding to 5 and 10% above the critical pressure p_c were tested with corresponding pseudocritical temperatures of 68.3 and 70.4°C respectively. Heat fluxes of 10 and 20 kW/m^2 were chosen, corresponding to heat transfer rates of 3.11 and 6.23 kW. Four different mass fluxes between 300 and 600 kg/s/m^2 were investigated, corresponding to refrigerant mass flow rates between 0.145 and 0.289 kg/s. Combining these parameters results in 16 different operating conditions.

Table 5.1: Proposed experimental matrix

		Mass flux G_{wf}			
Pressure p_{wf}	Heat flux $\dot{q}_{wf}$	300 kg/s/m^2	400 kg/s/m^2	500 kg/s/m^2	600 kg/s/m^2
$1.05 \cdot p_c$	10 kW/m^2				
	20 kW/m^2				
$1.10 \cdot p_c$	10 kW/m^2				
	20 kW/m^2				

5.1.2 Reaching the desired setpoints

The refrigerant pressure p_{wf} is controlled by the expansion valve position. Higher pressures are reached when it is closed more and vice versa. The refrigerant mass flux G_{wf} is controlled by the rotational speed of the pump. Higher mass fluxes are reached at increased rotational speeds and vice versa. During testing at low pressures and temperatures, these two effects did not behave independently of each other and e.g. adjusting expansion valve position also had an influence on mass flow rate. However, at the operating conditions described in Table 5.1 this was not the case and mass flow rate and pressure could be controlled completely independently.

The heat flux $\dot{q}_{wf}$ could not be controlled directly unlike the refrigerant pressure and mass flux. For a given p_{wf} and G_{wf}, $\dot{q}_{wf}$ depends on the refrigerant inlet temperature $T_{wf,in}$, thermal oil inlet temperature $T_{hf,in}$ and the thermal oil mass flow rate $\dot{m}_{hf}$. From Equation 4.4 it is clear that an increase in $\dot{m}_{hf}$ and $T_{hf,in}$ result in a larger h_{hf} and thus an increase in heat flux. For this reason, $\dot{m}_{hf}$ was chosen to be foxed at 2 kg/s during all measurements while $T_{hf,in}$ was varied to reach the desired heat flux. $T_{wf,in}$ was chosen to ensure that the pseudocritical temperature was reached around the middle of the test section.

5.1.3 Deviations from setpoints

Reaching the exact operating conditions shown in Table 5.1 was not possible. Precise controlling of the pressure using the expansion valve proved to be difficult. For the desired pressure of $1.05 \cdot p_c$, pressures between $1.04 \cdot p_c$ and $1.06 \cdot p_c$ were reached. Likewise, for the desired pressure of $1.10 \cdot p_c$, pressures between $1.09 \cdot p_c$ and $1.11 \cdot p_c$ were obtained.

Exactly controlling the refrigerant mass flux was also not possible. Instead of the values in Table 5.1, mass fluxes of 320, 430, 510 and 600 kg/s/m^2 were obtained. This was not an issue however, since obtaining very similar mass fluxes in different operating points was no problem.

As stated in the previous section, $\dot{q}_{wf}$ was controlled by changing the thermal oil inlet temperature. Using this method, deviations from the setpoints are in the order of 0.5 to 1 kW/m^2. Apart from the proposed measurement conditions in Table 5.1, some measurements were also performed with heat fluxes of about 16 to 18 kW/m^2.

5.2 Temperature range and accuracy

It is clear that a higher heat flux will cause a larger temperature differences over the test section for both the heating and working fluid. Another consequence of this is an improved accuracy of the calculated convection coefficients. As $\dot{m}_{hf}$ is fixed, a larger ΔT_{hf} corresponds to a smaller relative uncertainty on $\dot{Q}$ as shown in Equation 4.14. The error on the final results are mostly due to the uncertainty of ΔT_{hf} and the accuracy of the Dittus-Boelter correlation. The latter is assumed constant under all operating conditions.

Two examples of measurements are shown in Figures 5.1 and 5.2, where the dotted horizontal line in the T-s diagrams represents the pseudocritical temperature. Both measurements were done at a pressure of $1.10 \cdot p_c$. The data in Figure 5.1 was obtained at G_{wf}=600 kg/s/m^2 and $\dot{q}_{wf}$=10 kW/m^2. As expected, the relative errors on the values of h_{wf} are high, about 49%. In addition, the T-s diagram shows that only a limited bulk refrigerant temperature range is covered by this measurement. The data in Figure 5.2 shows a measurement at G_{wf}=320 kg/s/m^2 and $\dot{q}_{wf}$=20 kW/m^2. The relative errors of h_{wf} are about 20% in this case, less than half compared to the previous data. The T-s diagram shows a larger, but still quite limited, bulk refrigerant temperature range.

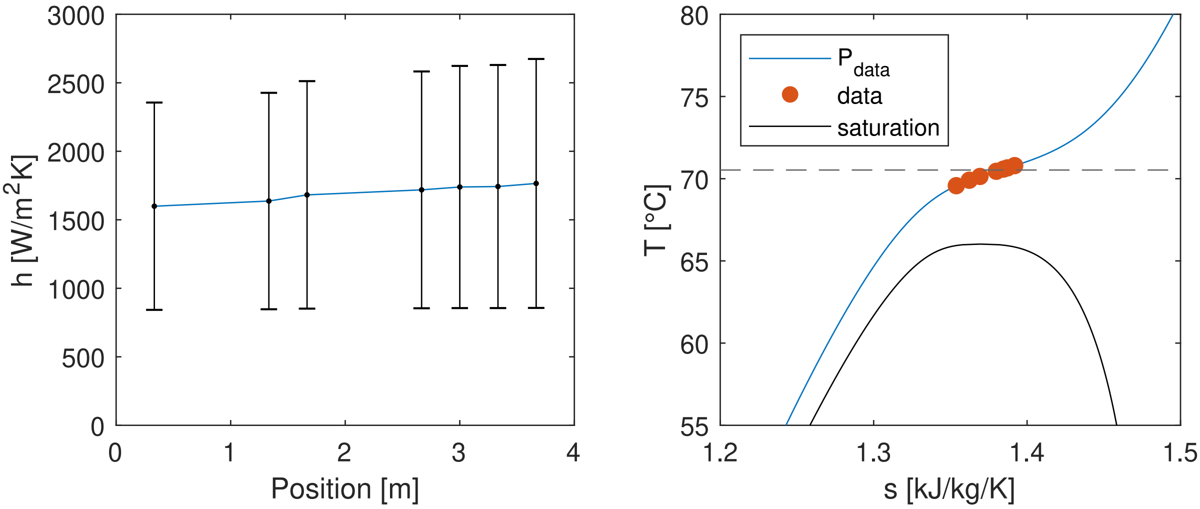

Figure 5.1: Accuracies of h_{wf} (left) and refrigerant temperature range (right) for measurements at high G_{wf} and low $\dot{q}_{wf}$

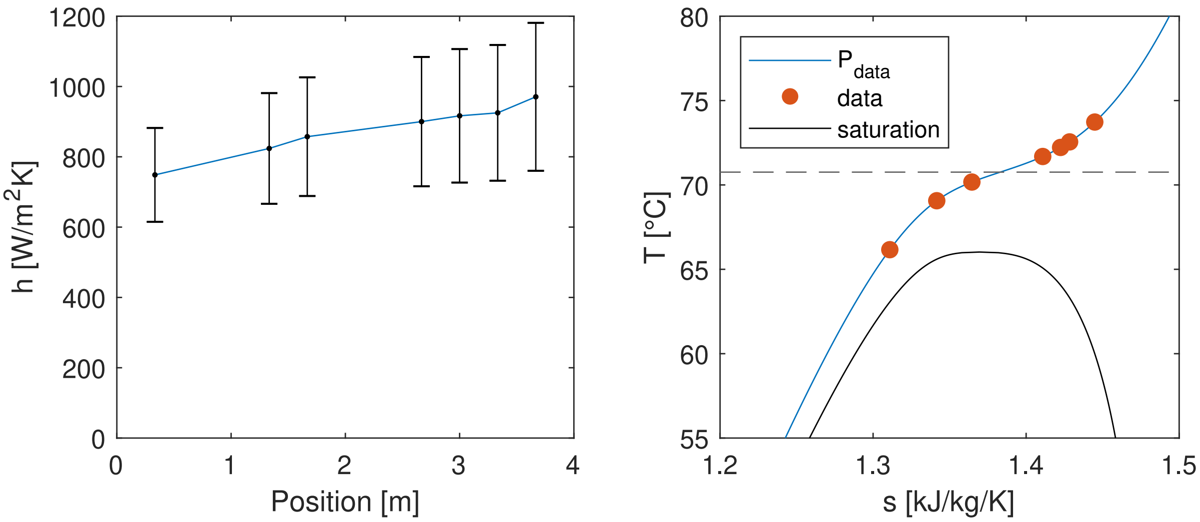

Figure 5.2: Accuracies of h_{wf} (left) and refrigerant temperature range (right) for measurements at low G_{wf} and high $\dot{q}_{wf}$

In all the performed measurements, no peaks in heat transfer coefficients were seen at or around the pseudocritical temperature. This is opposed to different results found in literature, presented in the second chapter. This is presumably caused by two factors. First, no wall temperature measurements are incorporated in the measurement setup.

Buoyancy effects are to be expected as the test section is placed horizontally, causing higher convection coefficients at the bottom of the tube. Because no variation in wall temperature is assumed in the data reduction, these effects could not be measured in any way.

Second, $\dot{Q}$ was assumed to be constant over the test section length because of the malfunctioning thermocouples at the thermal oil side. As $\dot{q}_{hf}$ and $\dot{Q}$ are needed to determine the temperature drops due to convection at the oil side and conduction through the inner tube wall, the resulting values for $T_{w,i}$ do not vary much over the test section length and presumably deviate from the actual inner wall temperatures. According to Equation 4.9, this heavily influences the obtained values for h_{wf}.

Even though the measured datasets are limited in temperature range and accuracy, general trends can still be seen which are discussed in section 5.4.

5.3 Repeatability

It is important that the results found under certain operating conditions are reproducible. Figure 5.3 shows three separate measurements performed under approximately equal operating conditions. First of all it is clear that obtaining the exact same heat flux is more difficult than obtaining the same pressure and mass flux. Second, it shows that the results are indeed reproducible as the deviations between the different measurements are much smaller than their error bars. This shows the reliability of the performed measurements. Very similar results were found for other repeated measurements.

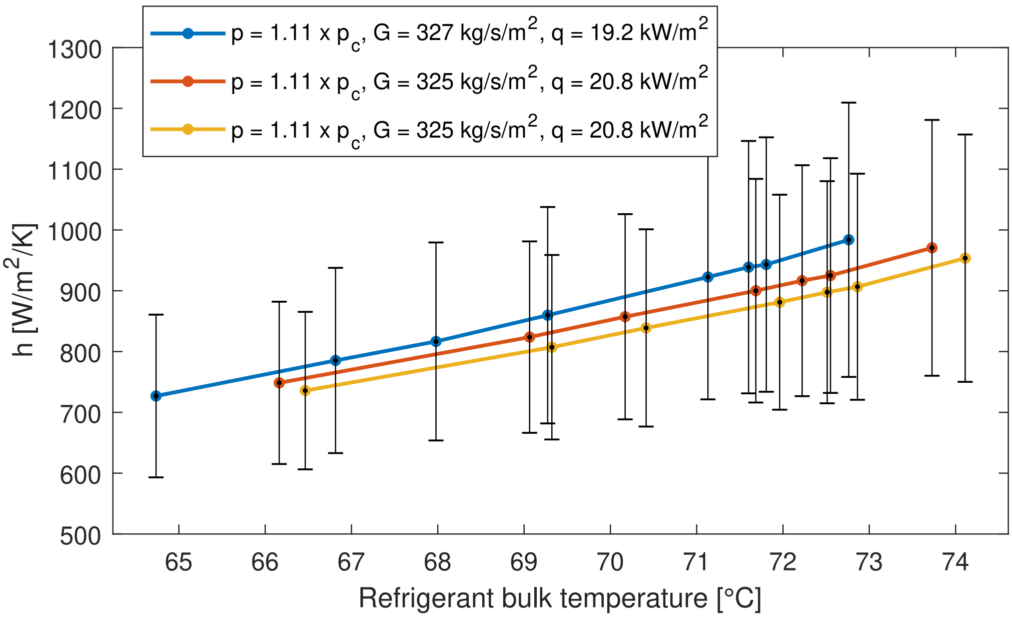

Figure 5.3: Example of repeatability check

5.4 Influences on heat transfer coefficients

In this section, the influences of p_{wf}, G_{wf} and $\dot{q}_{wf}$ on the convection coefficients h_{wf} are discussed. One example is shown for each influence, the other similar comparisons can be found in Appendix B. In these graphs, the dotted vertical lines indicate the pseudocritical temperature of the dataset of the same colour. A consequence of the limited measurement accuracy is the overlap of all compared data. Nevertheless, general trends in the measured convection coefficients can still be observed. The error bars are not shown in the graphs for clarity reasons. Appendix C contains all the experimental data in tabulated form.

5.4.1 Influence of pressure

Figure 5.4 shows the measured convection coefficients as a function of the bulk refrigerant temperature for different pressures at the same mass and heat flux. As expected from results found in literature, an increase in pressure results in a decrease in heat transfer coefficients. Due to the limited measurement accuracy, the two measurements for a pressure of $1.09 \cdot p_c$ show varying results. Still, the expected influence of the pressure holds.

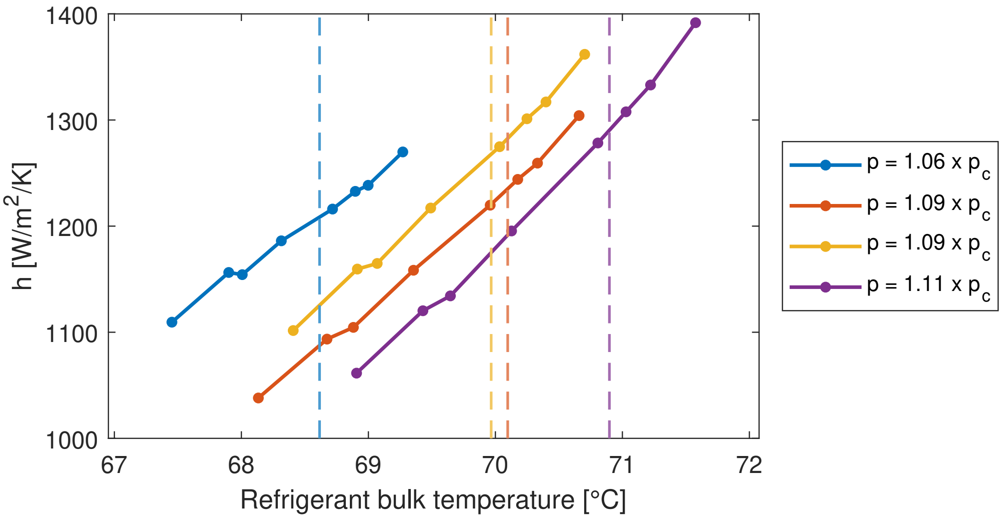

Figure 5.4: Influence of pressure at G_{wf}=320 kg/s/m^2 and $\dot{q}_{wf}$=10 kW/m^2

In Appendix B, figures B.1 through B.5 show the comparisons for other combinations of mass and heat fluxes. Since there was no overlap in refrigerant bulk temperature in some cases (in particular in the low heat flux cases), not all measurements could be compared. In all graphs, except for Figure B.1, the expected effect of an increase in pressure is visible. Figure B.1 shows three measurements at a high pressure and two measurements at a low pressure. As repeated measurements show varying results, no clear conclusion is found in this case. Still, there is no reason to assume the prediction of lower heat transfer coefficients at increased pressures is wrong since the varying results can be explained by the measurement accuracy.

5.4.2 Influence of mass flux

Figure 5.5 shows the measured convection coefficients as a function of the bulk refrigerant temperature for different mass fluxes at the same pressure and heat flux. The results meet the expectation, a higher mass flux and thus a higher Reynolds number causes increased convection coefficients.

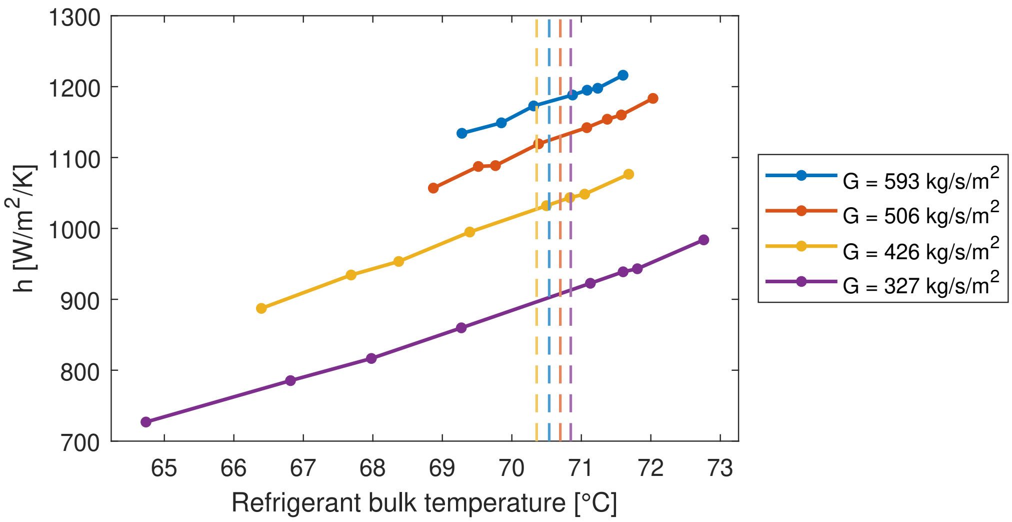

Figure 5.5: Influence of mass flux at p_{wf}=1.10·p$_c$ and $\dot{q}_{wf}$=20 kW/m^2

Figures B.6 through B.10 in Appendix B show the comparisons for other combinations of pressures and heat fluxes. In all these graphs, large deviations in mass flux result in clear differences in convection coefficients. However, if the difference is smaller (comparison between 600 and 510 kg/s/m^2 in Figure B.6 for example), the difference can be very small or zero. Again, this could be explained by the limited measurement accuracy.

5.4.3 Influence of heat flux

Figure 5.6 shows the measured convection coefficients as a function of the bulk refrigerant temperature for different heat fluxes at the same pressure and mass flux. Also in this case the results are as expected, higher heat fluxes lead to decreased convection coefficients.

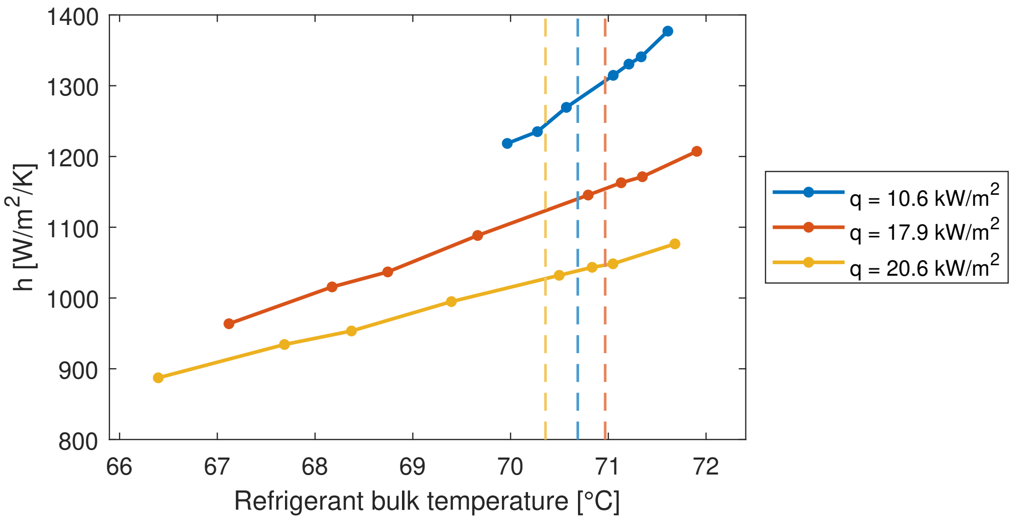

Figure 5.6: Influence of heat flux at p_{wf}=1.10·p$_c$ and G_{wf}=430 kg/s/m^2

Figures B.11 through B.17 in Appendix B show the comparisons for other combinations of pressures and mass fluxes. In all cases except for Figure B.15, measurements at lower heat fluxes show higher convection coefficients. In the case of Figure B.15, no clear difference is seen between the cases of 17 and 20 kW/m^2. Again, this could be explained by the limited measurement accuracy.

5.5 Wilson plots

A first attempt at the development of a correlation can be made based on the measured datasets using the Wilson plot method. Again, the absolute values are of less importance but general trends are visible.

5.5.1 The Wilson plot method

The Wilson plot method was developed in 1915 by Wilson [55] and was originally designed for calculating convection coefficients in shell and tube heat exchangers for shell-side condensation [56–58]. If fouling resistances are neglected, the total thermal resistance R_{tot} can be expressed as:

$$R_{tot} = \frac{1}{U \cdot A} = \frac{1}{h_i \cdot A_i} + \frac{ln(d_o/d_i)}{2\pi \cdot \lambda_w \cdot L} + \frac{1}{h_o \cdot A_o} \tag{5.1}$$

In this equation, h_i and h_o are the internal and external convection coefficients respectively. A_i and A_o are the internal and external heat transfer areas, d_i and d_o the inner and outer tube diameters, L the tube length and λ_w the thermal conductivity of the tube wall. U is the overall heat transfer coefficient. The outer convection coefficient h_o can be seen as a function of the fluid velocity (related to the Reynolds number) while all other terms in Equation 5.1 can be seen as constant. By performing experiments under different operating conditions, h_o can then be estimated as a function of the Reynolds number.

This method can also be used in a modified form to determine heat transfer correlations in any type of heat exchanger. A Dittus-Boelter type correlation of the form $Nu_b = c \cdot Re_b^m \cdot Pr_b^n$ with c, m and n constants can be derived in a similar way as described above. If a value for the Prandtl number exponent n is chosen to be zero, log(Nu) can be plotted against log(Re) for a certain dataset. The principle is shown in Figure 5.7.

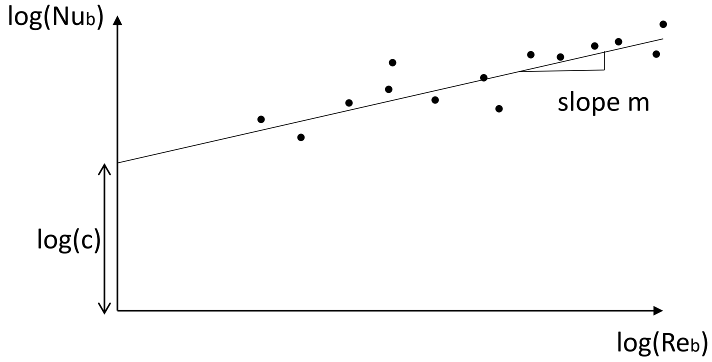

Figure 5.7: Wilson plot method

Generally speaking the data will be such that a linear relation can be fitted to this plot. According to Figure 5.7 the fitted line is of the form:

$$log(Nu_b) = m \cdot log(Re_b) + log(c) \tag{5.2}$$

Which can be rewritten as:

$$Nu_b = c \cdot Re_b^m \tag{5.3}$$

This final equation is a heat transfer correlation of the Dittus-Boelter type with an exponent of zero for the Prandtl number. This means that the slope in the modified Wilson plot is the same as the exponent of the Reynolds number in the correlation.

5.5.2 Wilson plots of measured data

Figure 5.8 shows all data points from the measurement matrix in the top left graph together with a linear fitting. Red dots represent the data for a heat flux of 20 kW/m^2, blue dots for a heat flux of 10 kW/m^2. Note that only a limited range of Reynolds numbers is present in the dataset, ranging from about $130 \cdot 10^3$ to $630 \cdot 10^3$. Still, larger Reynolds numbers correspond to higher Nusselt numbers generally. The fitted curve for the whole dataset results in $Nu_b = 10.186 \cdot Re_b^{0.329}$.

In addition, this dataset can be split up according to the heat flux. As explained above, increasing the heat flux results in lower convection coefficients. A linear fitting for the datasets containing a heat flux of 10 kW/m^2 can be found in the top right graph in Figure 5.8. The same can be found for a heat flux of 20 kW/m^2 in the bottom left graph. Directly comparing the values for m and $log(c)$ in these cases does not result in a clear conclusion. However, the fitted curves are plotted in the bottom right graph for the range of measured Reynolds numbers. As expected, the lower heat flux results in larger Nusselt numbers. Moreover, the fitted curves are almost parallel for this range of Reynolds numbers. This leads to the conclusion that the influence of the heat flux on the obtained convection coefficients is more or less independent of the refrigerant Reynolds number. In addition, the fitted curve for all data in the measurement matrix lies between the red and blue curves as expected.

Likewise, the dataset can be split up for higher and lower pressures. However, during the measurements discussed in this work the pseudocritical temperature was always chosen to be around the middle of the test section. Higher convection coefficients were measured at lower pressures for the same refrigerant bulk temperature. However, these bulk temperatures were not equal for measurements at different pressures and measured values of h_{wf} for a higher temperature and pressure could be in the same range as those for a lower temperature and pressure. Therefore, no conclusion on the influence of pressure can currently be made. Only if the dataset would contain measurements for the same range of bulk refrigerant temperatures, a reliable comparison between pressures is possible.

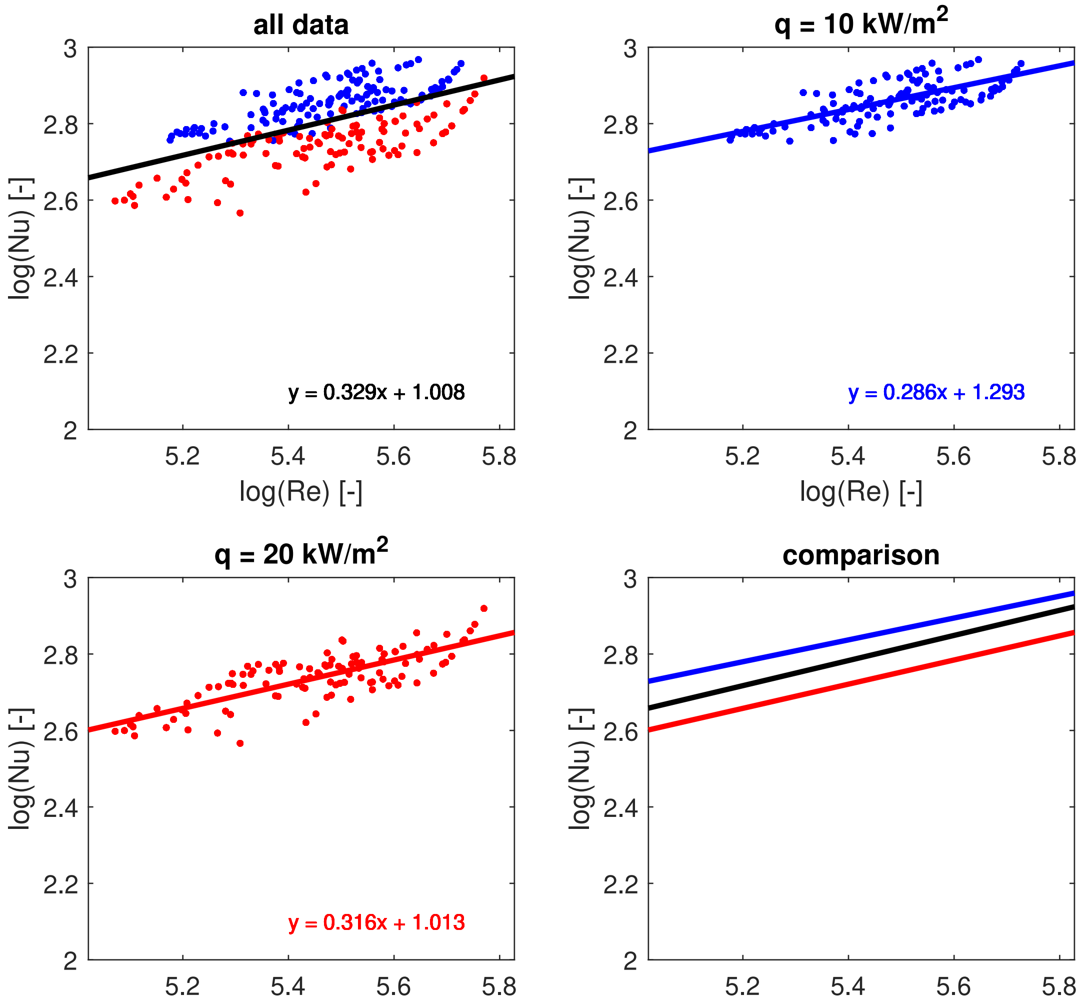

Figure 5.8: Wilson plots of experimental data with comparison between heat fluxes

5.6 Comparison to existing correlations

The results found in the experiments can be compared to existing correlations found in literature. The five correlations that predicted the results the most accurate are discussed in this section. First, some general definitions are given for the different factors in the correlations:

$$Nu_b = \frac{h \cdot d_h}{\lambda_b} \qquad (5.4) \qquad\qquad \bar{c}_p = \frac{h_w - h_b}{T_w - T_b} \qquad (5.5)$$

$$Re_b = \frac{G \cdot d_h}{\mu_b} \qquad (5.6) \qquad\qquad Re_w = \frac{G \cdot d_h}{\mu_w} \qquad (5.7)$$

$$Pr_b = \frac{c_{p,b} \cdot \mu_b}{\lambda_b} \quad (5.8) \qquad Pr_w = \frac{c_{p,w} \cdot \mu_w}{\lambda_w} \quad (5.9)$$

$$\bar{Pr}_b = \frac{\bar{c}_p \cdot \mu_b}{\lambda_b} \quad (5.10) \qquad \bar{Pr}_w = \frac{\bar{c}_p \cdot \mu_w}{\lambda_w} \quad (5.11)$$

The first correlation (Equations 5.12 and 5.13) was developed by Miropolski and Shitsman [36, 59] for supercritical water flowing in vertical tubes with inner diameters of 7.8 and 8.2 mm. No range of validity is known as the data was presented in a nondimensional form [33].

$$Nu_b = 0.023 \cdot Re_b^{0.80} \cdot Pr_{min}^{0.80} \tag{5.12}$$

$$Pr_{min} = min(Pr_w, Pr_b) \tag{5.13}$$

Krasnoshchekov and Protopopov [37] developed a correlation (Equations 5.14, 5.15 and 5.16) for water and CO_2 flowing in horizontal tubes. Data was collected for water pressures between 22.3 and 32 MPa, Reynolds numbers ranging from $2 \cdot 10^4$ to $8.6 \cdot 10^5$, $\bar{Pr}_b$ between 0.85 and 0.65, $\frac{\mu_b}{\mu_w}$ between 0.9 and 6.3, $\frac{\lambda_b}{\lambda_w}$ between 1 and 6, $\frac{\bar{c}_p}{c_{p,b}}$ between 0.07 and 4.5.

$$Nu_b = Nu_{0,b} \left(\frac{\bar{c}_p}{c_{p,b}}\right)^{0.35} \left(\frac{\lambda_b}{\lambda_w}\right)^{-0.33} \left(\frac{\mu_b}{\mu_w}\right)^{0.11} \tag{5.14}$$

$$Nu_{0,b} = \frac{(f/8) \cdot Re_b \cdot \bar{Pr}_b}{1.07 + 12.7(f/8)^{1/2} \left(\bar{Pr}_b^{2/3} - 1\right)} \tag{5.15}$$

$$f = (1.82 \cdot log_{10}(Re_b) - 1.64)^{-2} \tag{5.16}$$

The correlation by Swenson et al. [60] (Equation 5.17) was developed for water flowing in a horizontal tube with a diameter of 9.4 mm and a length of 1.83 m. Pressures varied between 23 and 41 MPa, heat fluxes between 200 and 1800 kW/m^2 and mass fluxes between 542 and 2150 kg/s/m^2.

$$Nu_b = 0.00459 \cdot Re_w^{0.923} \cdot \bar{Pr}_w^{0.613} \left(\frac{\rho_w}{\rho_b}\right)^{0.231} \left(\frac{\lambda_w}{\lambda_b}\right) \tag{5.17}$$

Jackson and Hall [61] (Equation 5.18) combined results found in literature for water and CO_2 flowing in circular tubes. No supposed range of validity could be found.

$$Nu_b = 0.0183 \cdot Re_b^{0.82} \cdot Pr_b^{0.50} \left(\frac{\rho_w}{\rho_b}\right)^{0.50} \left(\frac{\bar{c}_p}{c_{p,b}}\right)^{0.40} \tag{5.18}$$

Yu et al. [62] (Equation 5.19) studied heat transfer on supercritical water in a horizontal tube with an inner diameter of 26 mm and length of 2 m. Mass fluxes varied between 300 and 700 kg/s/m^2, heat fluxes between 200 and 400 kW/m^2 and pressures between 23 and 25 MPa. Buoyancy effects were seen and a different correlation for the top and bottom of the tube were formed. The correlation for the top of the tube proved to be the better predictor for the experimental data:

$$Nu_b = 0.000119 \cdot Re_b^{1.2} \cdot \bar{Pr}_b^{0.695} \left(\frac{\rho_w}{\rho_b}\right)^{0.398} \left(\frac{\lambda_w}{\lambda_b}\right)^{0.275} \tag{5.19}$$

Tables 5.2 through 5.6 compare the experimental data with the correlations described above for all combinations of parameters in the measurement matrix. In general, the accuracy depends on the mass flux of the refrigerant while the heat flux and pressure seem to be less of an influence.

Table 5.2: Comparison between experimental results and the correlation by Miropolski and Shitsman

		G_{wf}			
p_{wf}	$\dot{q}_{wf}$	320 kg/s/m^2	430 kg/s/m^2	510 kg/s/m^2	600 kg/s/m^2
$1.05 \cdot p_c$	10 kW/m^2	±11.6%	±25.1%	±29.5%	±58.8%
	20 kW/m^2	±16.2%	±23.6%	±29.5%	±46.6%
$1.10 \cdot p_c$	10 kW/m^2	±7.7%	±21.1%	±21.2%	±34.5%
	20 kW/m^2	±9.9%	±15.9%	±19.9%	±34.3%
Average deviation		±25.3%			

Table 5.3: Comparison between experimental results and the correlation by Krasnoshchekov and Protopopov

		G_{wf}			
p_{wf}	$\dot{q}_{wf}$	320 kg/s/m^2	430 kg/s/m^2	510 kg/s/m^2	600 kg/s/m^2
$1.05 \cdot p_c$	10 kW/m^2	±25.7%	±17.5%	±19.8%	±1.6%
	20 kW/m^2	±27.3%	±29.1%	±28.5%	±16.8%
$1.10 \cdot p_c$	10 kW/m^2	±22.9%	±10.9%	±19.9%	±23.4%
	20 kW/m^2	±27.3%	±26.1%	±17.5%	±11.9%
Average deviation		±20.4%			

Table 5.4: Comparison between experimental results and the correlation by Swenson et al.

		G_{wf}			
p_{wf}	$\dot{q}_{wf}$	320 kg/s/m^2	430 kg/s/m^2	510 kg/s/m^2	600 kg/s/m^2
$1.05 \cdot p_c$	10 kW/m^2	±12.1%	±26.2%	±50.2%	±55.1%
	20 kW/m^2	±9.8%	±18.9%	±35.4%	±44.2%
$1.10 \cdot p_c$	10 kW/m^2	±17.1%	±30.3%	±48.4%	±61.9%
	20 kW/m^2	±11.3%	±20.2%	±29.5%	±47.1%
Average deviation		±32.4%			

Table 5.5: Comparison between experimental results and the correlation by Jackson and Hall

		G_{wf}			
p_{wf}	$\dot{q}_{wf}$	320 kg/s/m^2	430 kg/s/m^2	510 kg/s/m^2	600 kg/s/m^2
$1.05 \cdot p_c$	10 kW/m^2	±9.7%	±27.6%	±38.9%	±57.5%
	20 kW/m^2	±12.1%	±19.7%	±27.3%	±47.2%
$1.10 \cdot p_c$	10 kW/m^2	±5.3%	±21.1%	±20.4%	±35.0%
	20 kW/m^2	±9.7%	±12.7%	±19.0%	±35.7%
Average deviation		±24.9%			

Table 5.6: Comparison between experimental results and the correlation by Yu et al.

		G_{wf}			
p_{wf}	$\dot{q}_{wf}$	320 kg/s/m^2	430 kg/s/m^2	510 kg/s/m^2	600 kg/s/m^2
$1.05 \cdot p_c$	10 kW/m^2	±23.9%	±2.6%	±17.3%	±45.4%
	20 kW/m^2	±31.0%	±17.9%	±6.9%	±16.0%
$1.10 \cdot p_c$	10 kW/m^2	±22.0%	±2.4%	±17.1%	±36.6%
	20 kW/m^2	±36.3%	±19.6%	±3.5%	±16.1%
Average deviation		±19.7%			

The correlation of Miropolski and Shitsman provides the most accurate predictions for the lower mass fluxes and gradually worse predictions for increasing mass fluxes. Similar results are found for the correlations of Swenson et al. and Jackson and Hall. The correlation of Krasnoshchekov and Protopopov provides better accuracy for the highest mass flux. In addition, the worst predictions deviate about 30% from the experimental results. This is less than the previous three correlations, where the deviations at the highest mass flux rises to about 50-60%. The correlation by Yu et al. (originally designed for Nusselt numbers at the top of a tube) provides the best accuracy for the mass fluxes in between. Also in this case less measurements deviate a large amount from the experimental data. However, when combining this correlation with the correlation for the bottom of a tube (not shown above), the accuracy drops to about 45%.

When looking at the total average deviations between the correlations and the experimental data, the correlations of Yu et al. and Krasnoshchekov and Protopopov provide the best accuracy, about 20%. The correlations of Jackson and Hall and Miropolski and Shitsman both result in deviations of about 25%. The correlation of Swenson et al. provides the worst prediction of these correlations with an average deviation of over 30%, caused by the large deviations at the highest mass flux.

Chapter 6

Proposed adaptation to current setup

Based on the information given in the previous chapters, adaptations to the measurement setup can be proposed for various reasons.

6.1 Incorporating wall temperature measurements

First, wall temperatures can be included at the outer wall of the inner tube. The reason is twofold: it would be possible to measure different wall temperatures at the same location in the test section and it would benefit the accuracy of the data reduction results. Figure 6.1 shows the proposed locations.

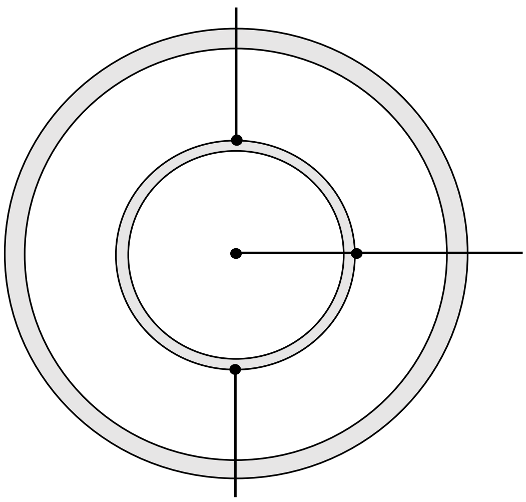

Figure 6.1: Proposed wall temperature measurement locations

The top, side and bottom positions of the tube were chosen to make the detection of variable wall temperatures possible. Only one side is chosen since the flow should show symmetry around the vertical plane containing the tube centreline. In this way, buoyancy driven temperature differences can be detected, leading to different convection coefficients along the tube circumference. Next to this, the peaks in convection coefficients at and near T_{pc} could be detected.

In addition, the accuracy of the measurements would improve drastically. As the outer wall temperatures are determined using the Dittus-Boelter correlation in the current setup, quite large errors on $T_{w,o}$ are present. A reliable estimate of the new errors of h_{wf} can be calculated based on the current measured datasets. Figures 6.2 and 6.3 show the improvements of the data shown in Figures 5.1 and 5.2. In the calculations, the error on $T_{w,o}$ was set to 0.1°C, the same as the error on the thermocouple measurements. The results show a greatly improved accuracy for both measurements. In Figure 6.2 the relative error on h_{wf} drops from 50% to 19%, less than half of the initial error. In Figure 6.3 the relative error on h_{wf} drops from 20% to 10%, halving the errors.

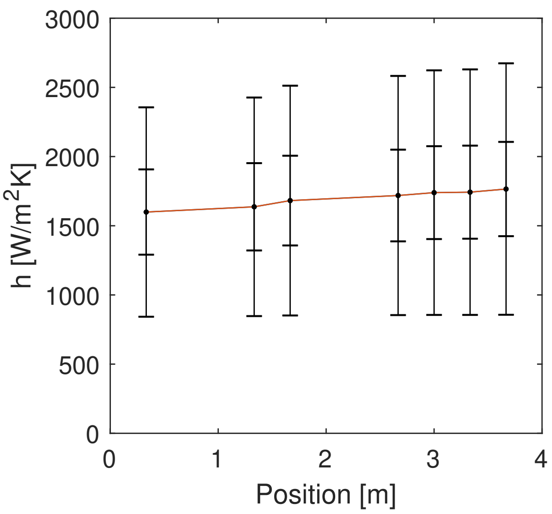

Figure 6.2: Accuracy improvement of h_{wf} for measurements at high G_{wf} and low $\dot{q}_{wf}$

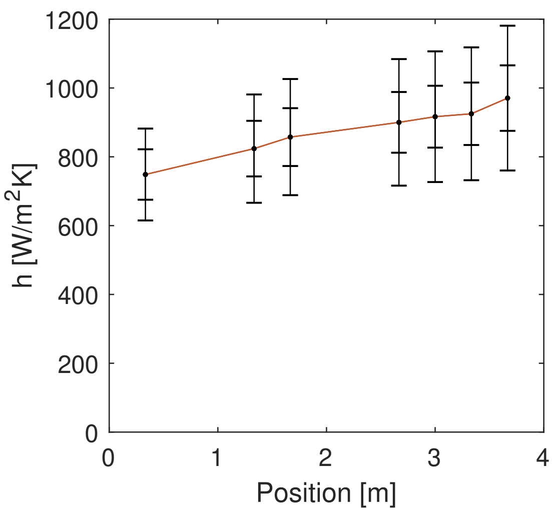

Figure 6.3: Accuracy improvement of h_{wf} for measurements at low G_{wf} and high $\dot{q}_{wf}$

The resulting errors are mainly due to the uncertainty of ΔT_{hf}, used to obtain the value for the heat transfer rate $\dot{Q}$. Lowering the thermal oil mass flow rate $\dot{m}_{hf}$ would increase ΔT_{hf} for a fixed heat flux, improving the accuracy. However, the corresponding thermal oil Reynolds number would decrease, causing a lower h_{hf}. This should then be counteracted by a higher inlet thermal oil temperature $T_{hf,in}$, but this temperature is limited to 125°C, which causes the need for higher values of $\dot{m}_{hf}$ in practice.

6.2 Testing other working fluids

The current working fluid R125 has a GWP of 3500 [63]. It can be replaced by other working fluids suitable for supercritical operation with a low GWP. In addition, the test setup should be able to handle the required pressures and temperatures corresponding to the new working fluid. Generally speaking, a working fluid has ideally both a low critical temperature and pressure. The former allows for heat recovery at low temperatures, the latter is related to practical issues. Up until now, few low GWP working fluids that have low critical parameters are available [4]. In addition, factors described in section 1.3 need to be taken into account.

Table 6.1 shows examples of working fluids with a critical pressure below 50 bar, meaning that they could be tested at supercritical pressures within operating limits of the current test setup. It is clear that the critical temperatures of these working fluids are high compared to R125. As the temperature in the working fluid loop of the test setup is limited to 125°C, no working fluids are suitable. The refrigerant in Table 6.1 with the lowest T_c (R1123) has a critical pressures of about 45 bar, meaning that only pressures just exceeding p_c could be tested. In addition, the thermal oil temperature is limited to 130°C. This maximum causes a limited temperature difference between heating fluid and working fluid and thus prohibits large heat fluxes to be tested.

Table 6.1: Examples of working fluids with a critical pressure below 50 bar and a limited GWP and T_c [64–67]

Refrigerant	T_c [°C]	p_c [bar]	GWP
R290 (propane)	96.7	42.5	20
R152a	113.26	45.2	120
R1270	91	45.6	20
R1123	58.6	45.5	3
R1234yf	94.7	33.8	<1
R1243zf	103.8	35.2	0.8
R1225zc	103.5	33.1	unknown
R1234ye(E)	109.5	37.3	2.3
R1234ze(E)	109.4	36.3	6
R1225ye(Z)	110.8	34.1	2.9
R1225ye(E)	117.7	34.2	2.9
R1234ze(Z)	150.1	35.3	1.4
R1336mzz(E)	130.2	27.7	18
R1233zd(E)	166.5	36.2	7
R1336mzz(Z)	171.4	29.0	2

As almost no working fluids are available which adhere to the restrictions of the current setup, alterations to the setup will have to be done to ensure that working fluids with higher critical temperatures and pressures can be tested. For example, changing components in the heating loop such that it can provide thermal oil at higher temperatures and adapting the working fluid loop such that refrigerant pressures above 50 bar are acceptable.

Chapter 7

Conclusion

Various thermodynamic cycles can benefit from operation at supercritical conditions. One example is the transcritical ORC, which is capable of converting low temperature heat into useful work. However, accurate correlations describing the heat transfer behaviour of refrigerants at the supercritical state, which are required to design the vapour generator in transcritical ORCs, are often lacking in literature. As a consequence, an accurate design is difficult, leading to oversizing of the vapour generator. The goal of this master thesis was to perform experimental measurements on supercritical R125 flowing in a horizontal tube in order to obtain local heat transfer coefficients.

For this purpose, a measurement setup was built in the previous years. It mimics the transcritical ORC with R125 as a working fluid. The vapour generator, a horizontal counterflow tube-in-tube heat exchanger, is the component of interest. It is rigged with measurement equipment to determine local convection coefficients of R125 at the supercritical state, which flows in the inner tube of the heat exchanger.

Measurements were performed at pressures between $1.04 \cdot p_c$ and $1.11 \cdot p_c$, refrigerant mass fluxes between 320 and 600 kg/s/m^2 and heat fluxes between 9 and 22 kW/m^2. The influences of the pressure, mass flux and heat flux could be investigated. In general, lower pressures, higher mass fluxes and lower heat fluxes result in higher convection coefficients. These results agree with expected results found in literature.

While the accuracy on the convection coefficients proved to be quite low, a first step to develop a new correlation could be done. Using the Wilson plot method, a linear trend could be seen for $log(Nu_b)$ as a function of $log(Re_b)$. Higher bulk Reynolds numbers correspond to larger Nusselt numbers and thus larger convection coefficients. When the data was split up according to low and high heat flux, a clear difference could be seen. The lower heat flux resulted in approximately a fixed increase in $log(Nu_b)$ for the range of tested Reynolds numbers.

Future work includes broadening the bulk refrigerant temperature, pressure, mass flux and heat flux ranges. In addition, the setup will be adapted such that wall temperature measurements are included. This leads to the detection of variable wall temperatures over the inner tube circumference due to buoyancy effects. Also, incorporating wall temperature measurements would greatly improve the accuracy on the obtained convection coefficients. Finally, the setup can be adapted for testing other low GWP working fluids suitable for heat recovery applications at the supercritical state.

Bibliography

[1] A. Landelle, N. Tauveron, R. Revellin, P. Haberschill, and S. Colasson, "Experimental Investigation of a Transcritical Organic Rankine Cycle with Scroll Expander for Low - Temperature Waste Heat Recovery", *Energy Procedia*, vol. 129, pp. 810–817, 2017.

[2] C. Yu, J. Xu, and Y. Sun, "Transcritical pressure Organic Rankine Cycle (ORC) analysis based on the integrated-average temperature difference in evaporators", *Applied Thermal Engineering*, vol. 88, pp. 2–13, 2015.

[3] M. J. Moran, H. N. Shapiro, D. D. Boettner, and M. B. Bailey, *Fundamentals of Engineering Thermodynamics*, 8th edition. Wiley, 2015.

[4] S. Lecompte, E. Ntavou, B. Tchanche, G. Kosmadakis, A. Pillai, D. Manolakos, and M. de Paepe, "Review of experimental research on supercritical and transcritical thermodynamic cycles designed for heat recovery application", *Applied Sciences*, vol. 9, no. 12, pp. 1–26, 2019.

[5] V. S. Reddy, S. C. Kaushik, S. K. Tyagi, and N. Panwar, "An Approach to Analyse Energy and Exergy Analysis of Thermal Power Plants: A Review", *Smart Grid and Renewable Energy*, vol. 01, no. 03, pp. 143–152, 2010.

[6] X. Li, H. Huang, and W. Zhao, "A supercritical or transcritical Rankine cycle with ejector using low-grade heat", *Energy Conversion and Management*, vol. 78, pp. 551–558, 2014.

[7] H. Chen, D. Y. Goswami, and E. Stefanakos, "A review of thermodynamic cycles and working fluids for the conversion of low-grade heat", *Renewable and Sustainable Energy Reviews*, vol. 14, no. 9, pp. 3059–3067, 2010.

[8] H. Gao, C. Liu, C. He, X. Xu, S. Wu, and Y. Li, "Performance analysis and working fluid selection of a supercritical organic rankine cycle for low grade waste heat recovery", *Energies*, vol. 5, no. 9, pp. 3233–3247, 2012.

[9] T. Gao and C. Liu, "Off-design performances of subcritical and supercritical organic rankine cycles in geothermal power systems under an optimal control strategy", *Energies*, vol. 10, no. 8, 2017.

[10] T. Guo, H. Wang, and S. Zhang, "Comparative analysis of natural and conventional working fluids for use in transcritical Rankine cycle using low-temperature geothermal source", *International journal of energy research*, vol. 35, no. 2010, pp. 530–544, 2011.

[11] D. Luo, A. Mahmoud, and F. Cogswell, "Evaluation of Low-GWP fluids for power generation with Organic Rankine Cycle", *Energy*, vol. 85, pp. 481–488, 2015.

[12] B. Saleh, G. Koglbauer, M. Wendland, and J. Fischer, "Working fluids for low-temperature organic Rankine cycles", *Energy*, vol. 32, no. 7, pp. 1210–1221, 2007.

[13] K. Yamagata, K. Nishikawa, S. Hasegawa, T. Fujii, and S. Yoshia, "Forced convective heat transfer to supercritical water flowing in tubes", *International Journal of Heat and Mass Transfer*, vol. 15, no. 12, pp. 2575–2593, 1972.

[14] I. Pioro and R. Duffey, *Heat Transfer and hydraulic resistance at supercritical pressures in power engineering applications.* ASME Press, 2007.

[15] I. H. Bell, J. Wronski, S. Quoilin, and V. Lemort, "Pure and Pseudo-pure Fluid Thermophysical Property Evaluation and the Open-Source Thermophysical Property Library CoolProp", *Industrial & Engineering Chemistry Research*, vol. 53, no. 6, pp. 2498–2508, 2014.

[16] M. Bazargan, D. Fraser, and V. Chatoorgan, "Effect of buoyancy on heat transfer in supercritical water flow in a horizontal round tube", *Journal of Heat Transfer*, vol. 127, no. 8, pp. 897–902, 2005.

[17] S. Yu, H. Li, X. Lei, Y. Feng, Y. Zhang, H. He, and T. Wang, "Influence of buoyancy on heat transfer to water flowing in horizontal tubes under supercritical pressure", *Applied Thermal Engineering*, vol. 59, no. 1-2, pp. 380–388, 2013.

[18] Krasyakova, Raykin, and Belyakov, "Investigation of temperature regime of heated tubes at supercritical pressure", *Soviet Energy Technology*, vol. 1, pp. 1–4, 1967.

[19] M. E. Shitsman, "The Effect of Natural Convection on Temperature Conditions in Horizontal Tubes at Supercritical Pressures", *Thermal Engineering (Teploenergetika)*, vol. 13, no. 7, pp. 69–75, 1966.

[20] J. Wang, Z. Guan, H. Gurgenci, K. Hooman, A. Veeraragavan, and X. Kang, "Computational investigations of heat transfer to supercritical CO2 in a large horizontal tube", *Energy Conversion and Management*, vol. 157, no. September, pp. 536–548, 2018.

[21] D. Huang, Z. Wu, B. Sunden, and W. Li, "A brief review on convection heat transfer of fluids at supercritical pressures in tubes and the recent progress", *Applied Energy*, vol. 162, pp. 494–505, 2016.

[22] J. D. Jackson and W. B. Hall, "Influences of Buoyancy on Heat Transfer to Fluids Flowing in Vertical Tubes under Turbulent Conditions", *Institution of Mechanical Engineers, Conference Publications*, vol. 2, pp. 613–640, 1979.

[23] B. Zhang, J. Shan, and J. Jiang, "Numerical analysis of supercritical water heat transfer in horizontal circular tube", *Progress in Nuclear Energy*, vol. 52, no. 7, pp. 678–684, 2010.

[24] B. S. Petukhov and A. F. Polyakov, *Heat Transfer in Mixed Turbulent Convection.* New York: Hemisphere Publishing Corporation, 1988.

[25] R. Tian, Y. Ma, D. Wang, H. Li, Y. Zhang, and L. Shi, "Tube diameter size effects on heat transfer of supercritical R134a in horizontal tubes for vapor generator design in organic rankine cycles", in *ACM International Conference Proceeding Series*, 2018, pp. 71–76.

[26] X. Lei, Q. Zhang, J. Zhang, and H. Li, "Experimental and numerical investigation of convective heat transfer of supercritical carbon dioxide at low mass fluxes", *Applied Sciences (Switzerland)*, vol. 7, no. 12, pp. 1–18, 2017.

[27] W. Chen, X. Fang, Y. Xu, and X. Su, "An assessment of correlations of forced convection heat transfer to water at supercritical pressure", *Annals of Nuclear Energy*, vol. 76, pp. 451–460, 2015.

[28] I. L. Pioro, H. F. Khartabil, and R. B. Duffey, "Heat transfer to supercritical fluids flowing in channels - Empirical correlations (survey)", *Nuclear Engineering and Design*, vol. 230, no. 1-3, pp. 69–91, 2004.

[29] Harmen, W. Adriansyah, Abdurrachim, and A. D. Pasek, "Theoretical investigation of heat transfer correlations for supercritical organic fluids", *AIP Conference Proceedings*, vol. 1984, no. July, 2018.

[30] F. Dittus and L. Boelter, "Heat Transfer in Automobile Radiators of the Tubular Type", *Publications in Engineering, University of California, Berkeley*, vol. 2, no. 13, pp. 443–461, 1930.

[31] V. Gnielinski, "New Equations for Heat and Mass Transfer in Turbulent Pipe and Channel Flow", *International Chemical Engineering*, vol. 16, no. 2, pp. 359–368, 1976.

[32] Petukhov and Kirillov, "About heat transfer at turbulent fluid flow in tubes", *Thermal Engineering (Teploenergetika)*, vol. 4, pp. 63–68, 1958.

[33] M. Bazargan, "Forced convection heat transfer to turbulent flow of supercritical water in a round horizontal tube", PhD thesis, 2001, p. 339.

[34] E. N. Sieder and G. E. Tate, "Heat Transfer and Pressure Drop of Liquids in Tubes", *Industrial and Engineering Chemistry*, vol. 28, no. 12, pp. 1429–1435, 1936.

[35] R. P. Bringer and J. M. Smith, "Heat transfer in the critical region", *AIChE Journal*, vol. 3, no. 1, pp. 49–55, 1957.

[36] L. Miropolski and M. E. Shitsman, "Heat Transfer to Water and Steam at Variable Specific Heat (In Near-Critical Region)", *Soviet Physics. Technical Physics.*, vol. 27, no. 10, pp. 2359–2372, 1957.

[37] E. Krasnoshchekov and V. Protopopov, "Heat transfer at supercritical region in flow of carbon dioxide and water in tubes", *Thermal Engineering*, vol. 12, pp. 26–30, 1959.

[38] M. Lazova, S. Daelman, A. Kaya, H. Huisseune, and M. De Paepe, "Heat Transfer in Horizontal Tubes At Supercritical Pressures for organic Rankine cycle applications", in *10th International Conference on Heat Transfer, Fluid Mechanics and Thermodynamics*, 2014, pp. 1044–1051.

[39] I. I. Belyakov, L. Y. Krasyakova, A. V. Zhukovskii, and N. D. Fefelova, "Heat Transfer in Vertical Risers and Horizontal Tubes at Supercritical Pressure", *Thermal Engineering (Teploenergetika)*, vol. 18, no. 11, pp. 39–43, 1971.

[40] G. A. Adebiyi and W. B. Hall, "Experimental investigation of heat transfer to supercritical pressure carbon dioxide in a horizontal pipe", *International Journal of Heat and Mass Transfer*, vol. 19, no. 7, pp. 715–720, 1976.

[41] J. D. Jackson and W. B. Hall, "Influences of Buoyancy on heat transfer to fluids in vertical tubes under turbulent conditions", *Turbulent Forced Convection in Channels and Bundles*, vol. 2, pp. 613–640, 1979.

[42] C. R. Zhao and P. X. Jiang, "Experimental study of in-tube cooling heat transfer and pressure drop characteristics of R134a at supercritical pressures", *Experimental Thermal and Fluid Science*, vol. 35, no. 7, pp. 1293–1303, 2011.

[43] R. Tian, D. Wang, Y. Zhang, Y. Ma, H. Li, and L. Shi, "Experimental study of the heat transfer characteristics of supercritical pressure R134a in a horizontal tube", *Experimental Thermal and Fluid Science*, vol. 100, pp. 49–61, 2019.

[44] D. Wang, X. Dai, R. Tian, and L. Shi, "Experimental investigation of the heat transfer of supercritical R134a in a horizontal micro-fin tube", *International Journal of Thermal Sciences*, vol. 138, no. December 2018, pp. 536–549, 2019.

[45] D. Wang, R. Tian, Y. Zhang, L. L. Li, and L. Shi, "Experimental comparison of the heat transfer of supercritical R134a in a micro-fin tube and a smooth tube", *International Journal of Heat and Mass Transfer*, vol. 129, pp. 1194–1205, 2019.

[46] R. Tian, M. Wei, X. Dai, P. Song, and L. Shi, "Buoyancy effect on the mixed convection flow and heat transfer of supercritical R134a in heated horizontal tubes", *International Journal of Heat and Mass Transfer*, vol. 144, p. 118 607, 2019.

[47] S. Garimella, "Near-critical/supercritical heat transfer measurements of R-410a is small diameter tube", Georgia Institute Of Technology, Tech. Rep., 2008.

[48] S. Garimella, B. Mitra, U. C. Andresen, Y. Jiang, and B. M. Fronk, "Heat transfer and pressure drop during supercritical cooling of HFC refrigerant blends", *International Journal of Heat and Mass Transfer*, vol. 91, pp. 477–493, 2015.

[49] S. W. Churchill, "Comprehensive Correlating Equations for Heat, Mass and Momentum Transfer in Fully Developed Flow in Smooth Tubes", *Industrial and Engineering Chemistry Fundamentals*, vol. 16, no. 1, pp. 109–116, 1977.

[50] M. Lazova, A. Kaya, S. Lecompte, and M. De Paepe, "Presentation of a test-rig for heat transfer measurements of a fluid at supercritical state for organic Rankine cycle application", in *Proceedings of the 16th International Heat Transfer Conference*, 2018, pp. 8389–8396.

[51] M. Lazova, S. Lecompte, and M. De Paepe, "Heat transfer of R125 at supercritical pressures tested in horizontal flow and under organic Rankine cycle conditions", in *25th IIR International Congress of Refrigeration*, 2019.

[52] S. Lecompte, S. Gusev, B. Vanslambrouck, and M. De Paepe, "Experimental results of a small-scale organic Rankine cycle: Steady state identification and application to off-design model validation", *Applied Energy*, vol. 226, no. May, pp. 82–106, 2018.

[53] R. J. Moffat, "Describing the uncertainties in experimental results", *Experimental Thermal and Fluid Science*, vol. 1, no. 1, pp. 3–17, 1988.

[54] R. A. Perkins and M. L. Huber, "Measurement and correlation of the thermal conductivity of pentafluoroethane (R125) from 190 K to 512 K at pressures to 70 MPa", *Journal of Chemical and Engineering Data*, vol. 51, no. 3, pp. 898–904, 2006.

[55] E. E. Wilson, "A basis of rational design of heat transfer apparatus", *ASME Journal of Heat Transfer*, vol. 37, pp. 47–70, 1915.

[56] J. Fernández-Seara, F. J. Uhía, J. Sieres, and A. Campo, "Experimental apparatus for measuring heat transfer coefficients by the Wilson plot method", *European Journal of Physics*, vol. 26, no. 3, 2005.

[57] J. Fernández-Seara, F. J. Uhía, J. Sieres, and A. Campo, “A general review of the Wilson plot method and its modifications to determine convection coefficients in heat exchange devices”, *Applied Thermal Engineering*, vol. 27, no. 17-18, pp. 2745–2757, 2007.

[58] J. Fernández-Seara, F. J. Uhía, and J. Sieres, “Laboratory practices with the wilson plot method”, *Experimental Heat Transfer*, vol. 20, no. 2, pp. 123–135, 2007.

[59] M. W. Shitsman, “Heat transfer to supercritical helium, carbon dioxide, and water: Analysis of thermodynamic and transport properties and experimental data”, *Cryogenics*, vol. 14, no. 2, pp. 77–83, 1974.

[60] H. S. Swenson, J. R. Carver, and C. R. Kakarala, “Heat transfer to supercritical water in smooth-bore tubes”, *Journal of Heat Transfer*, vol. 87, no. 4, pp. 477–483, 1965.

[61] J. D. Jackson and W. Hall, “Forced convection heat transfer to fluids at supercritical pressure”, *Turbulent Forced Convection in Channels and Bundles*, vol. 2, pp. 563–611, 1979.

[62] S. Yu, H. Li, X. Lei, Y. Feng, Y. Zhang, H. He, and T. Wang, “Experimental investigation on heat transfer characteristics of supercritical pressure water in a horizontal tube”, *Experimental Thermal and Fluid Science*, vol. 50, pp. 213–221, 2013.

[63] M. Lazova, S. Lecompte, and M. De Paepe, “Determining the Heat Transfer Characteristics of R125 at Supercritical Pressures”, in *Proceedings of the 5th International Seminar on ORC Power Systems*, 2019.

[64] S. Bobbo, G. D. Nicola, C. Zilio, J. S. Brown, and L. Fedele, “Low GWP halocarbon refrigerants: A review of thermophysical properties”, *International Journal of Refrigeration*, vol. 90, pp. 181–201, 2018.

[65] H. Chen, D. Y. Goswami, M. M. Rahman, and E. K. Stefanakos, “A supercritical Rankine cycle using zeotropic mixture working fluids for the conversion of low-grade heat into power”, *Energy*, vol. 36, no. 1, pp. 549–555, 2011.

[66] F. Moloney, E. Almatrafi, and D. Y. Goswami, “Working fluid parametric analysis for regenerative supercritical organic Rankine cycles for medium geothermal reservoir temperatures”, *Energy Procedia*, vol. 129, pp. 599–606, 2017.

[67] V. L. Le, M. Feidt, A. Kheiri, and S. Pelloux-Prayer, “Performance optimization of low-temperature power generation by supercritical ORCs (organic Rankine cycles) using low GWP (global warming potential) working fluids”, *Energy*, vol. 67, pp. 513–526, 2014.

Appendix A

Measurement procedure

Operating the iSCORE setup in a safe way requires following the steps presented in this appendix. It takes the malfunctioning measurement equipment into account.

1. Starting cooling loop.
   - Open the valves leading to the setup in the cooling loop circuit. If needed, close valves to other setups.
   - Check the temperature indicated at the buffer vessel, adapt it using the controller if needed.
   - Start the cooling loop circulation pump by plugging it in.
2. Starting working fluid loop.
   - Plug in the power supply of the pump and electric preheater controls.
   - Check if the Keithley and CompactRIO are switched on. Start the LabVIEW program and perform a test measurement to check if measurements are saved in the right way.
   - Activate emergency stop.
   - Open the shut-off valve.
   - Open expansion valve over 50% and close bypass valve.
   - Enable the pump drive and start pump remote.
   - Start the pump at a frequency of 10 Hz and check for any irregularities.
   - Close the expansion valve until a reliable refrigerant mass flow rate is measured.
   - Check the different temperatures and pressures on the monitoring screen. They should be within the operating limits which is generally no problem at this stage.
   - Fully open the mixing valve of the cooling loop.
3. Starting heating loop.
   - Start the thermal oil unit in circulation mode. Adapt the heating loop mixing valve position such that the desired oil mass flow rate is reached.

- Stop the thermal oil unit.
- Start the electric preheater and enter the desired refrigerant inlet temperature.
- Enter the desired oil inlet temperature on the thermal oil unit.
- Start the thermal oil unit in heating mode.

4. Reaching desired operating conditions.

   - Check the temperatures and pressures on the monitoring screen. Adapt the pump frequency to reach the desired mass flow rate and change the expansion valve position to reach the desired pressure in the test section.
   - Wait until steady-state operation is reached. Continue to check all parameters on the monitoring screen.
   - If the electric preheater is not able to reach the desired refrigerant temperature at the inlet of the test section, make use of one or both of the preheaters.

5. Performing measurements.

   - Start the measurements in the LabVIEW program by activating the *Start cRIO* and *Start Keithley* buttons.
   - Wait until a sufficient amount of samples is collected.
   - Stop and save the measurements by activating the *Stop & save cRIO* and *Stop & save Keithley* buttons.
   - Deactivate the *Start* buttons only after the *Stop & save* buttons are deactivated automatically.

6. Changing operating point.

   - Change the operating pressures and mass flow rates by adapting the pump frequency and expansion valve position. Continue to check the temperatures and pressures on the monitoring screen.
   - Change the temperature setpoint of the thermal oil unit. This can be done when it is operating in heating mode.
   - Change the temperature setpoint of the electric preheater.
   - Perform measurements as described above.

7. Shutting down the setup.

   - Stop the electric preheater. The main switch does not need to be unplugged.
   - Stop the thermal oil unit in heating mode and start it in circulation mode.
   - Monitor the pressures and temperatures on-screen. They should all decrease.
   - When the refrigerant temperature is below 35°C the thermal oil unit can be switched off. The main switch does not need to be unplugged.
   - Open expansion valve. Make sure the pressure at the inlet of the pump is never above 35 bar.
   - When the refrigerant temperature is below 30°C the pump frequency can be set to 10 Hz. The measured pressures should be between 16 and 18 bar.

- After two minutes of circulation at 10 Hz the electric preheater can be switched off.
- Close the mixing valves of the heating and cooling loops.
- Close the expansion valve.
- Shut off the circulation pump in the cooling loop circuit.
- Disable the pump drive and stop pump remote in the LabVIEW program.
- Close the shut-off valve.
- Deactivate emergency stop.
- Close LabVIEW program.
- Unplug the power supply of the pump and electric preheater controls.

Appendix B

Comparisons of measurements

The figures displayed in this appendix compare the measured heat transfer coefficients between different operating conditions. The vertical dotted lines represent the pseudocritical temperatures of the measurements of the same colour. The error bars are sometimes omitted for clarity reasons.

B.1 Influence of pressure

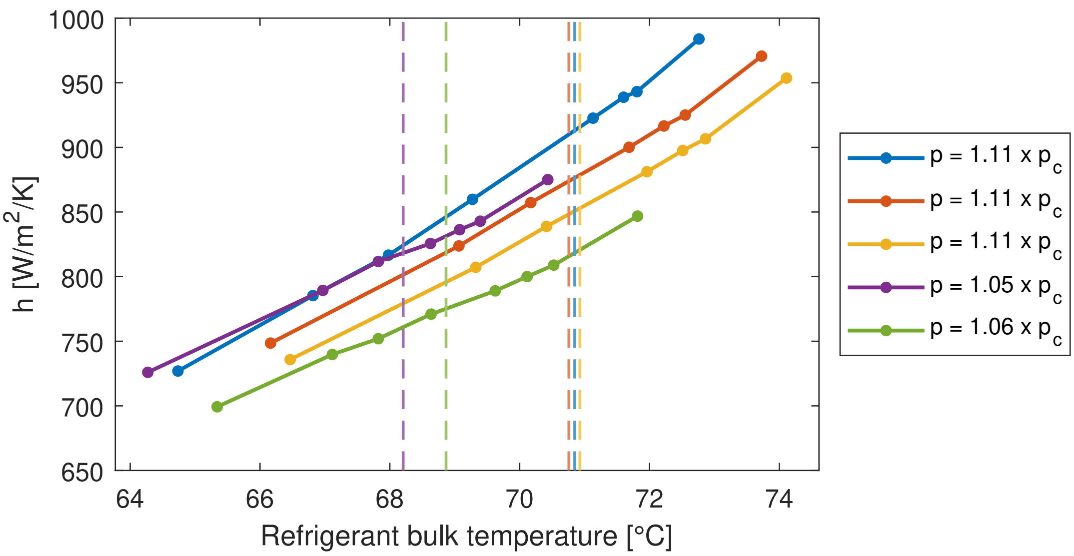

Figure B.1: Influence of pressure at G_{wf}=320 kg/s/m^2 and $\dot{q}_{wf}$=20 kW/m^2

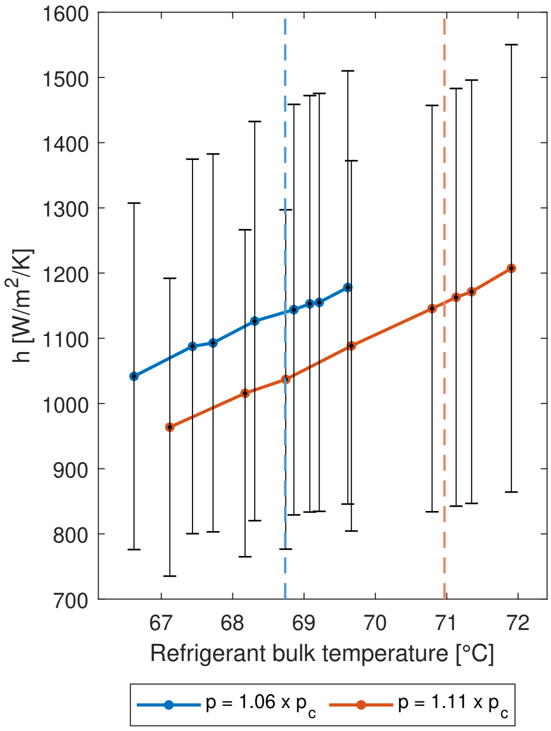

Figure B.2: Influence of pressure at G_{wf}=430 kg/s/m^2 and $\dot{q}_{wf}$=18 kW/m^2

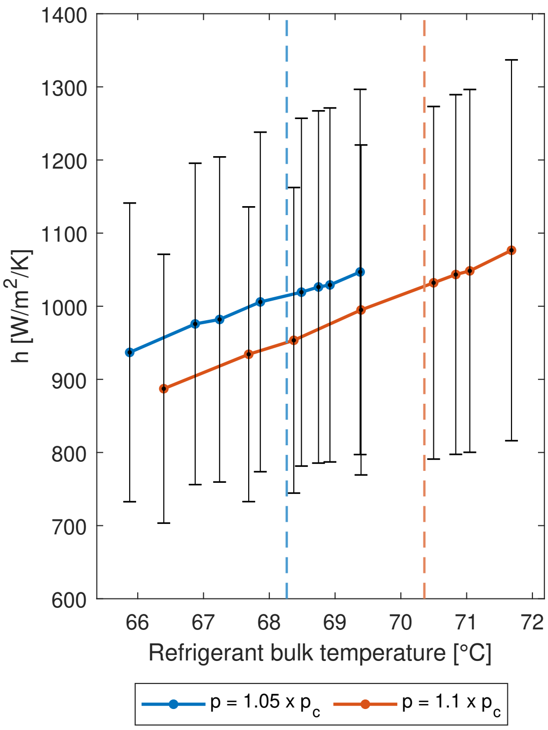

Figure B.3: Influence of pressure at G_{wf}=430 kg/s/m^2 and $\dot{q}_{wf}$=20 kW/m^2

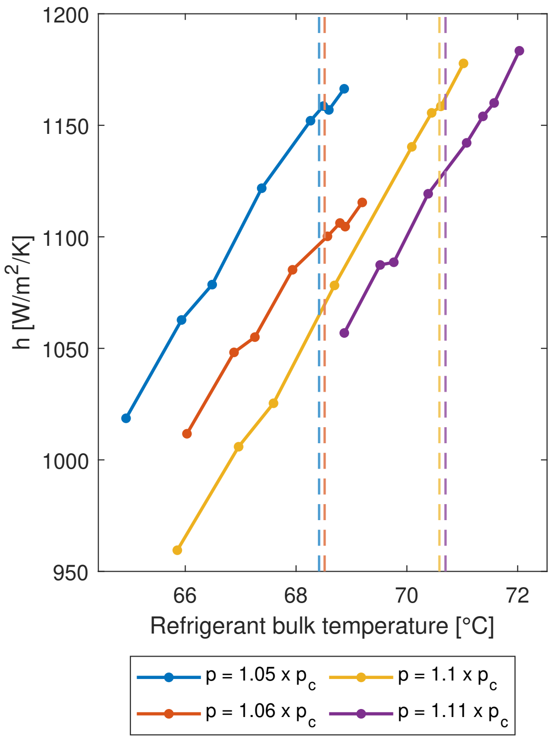

Figure B.4: Influence of pressure at G_{wf}=510 kg/s/m^2 and $\dot{q}_{wf}$=20 kW/m^2

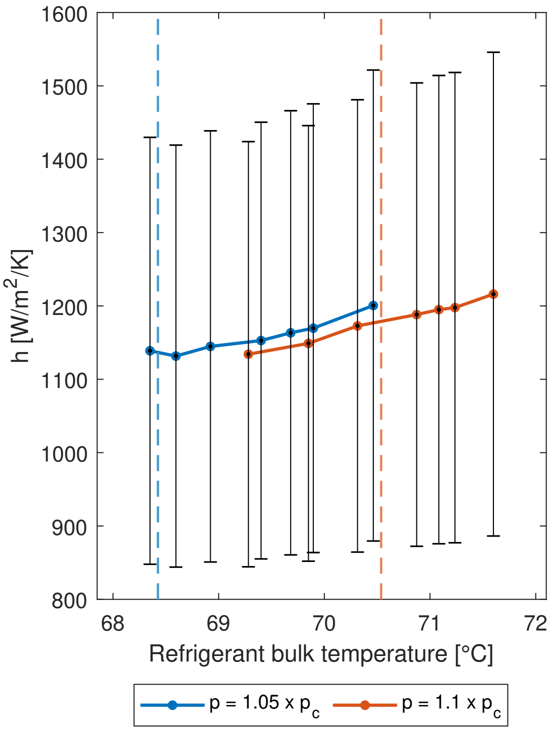

Figure B.5: Influence of pressure at G_{wf}=600 kg/s/m^2 and $\dot{q}_{wf}$=20 kW/m^2

B.2 Influence of mass flux

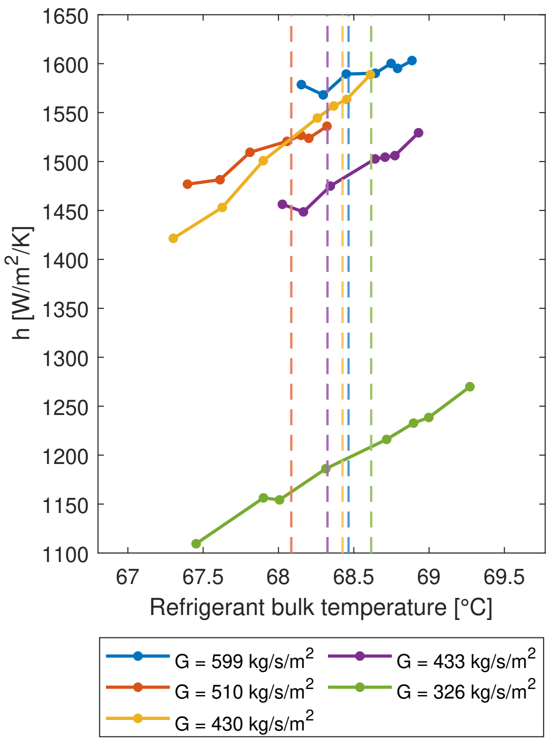

Figure B.6: Influence of mass flux at p_{wf}=1.05·p$_c$ and $\dot{q}_{wf}$=10 kW/m^2

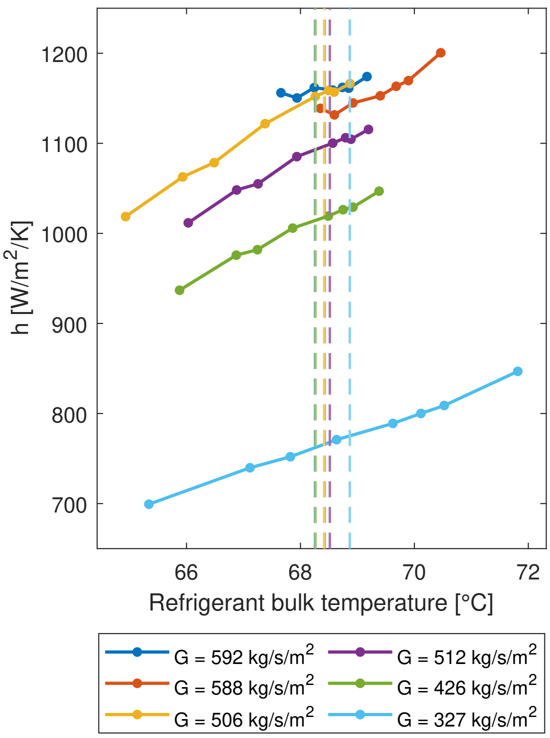

Figure B.7: Influence of mass flux at p_{wf}=1.05·p$_c$ and $\dot{q}_{wf}$=20 kW/m^2

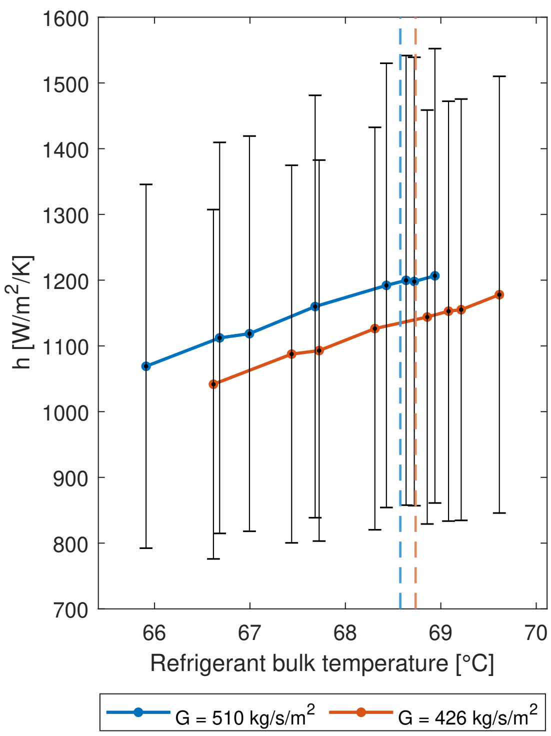

Figure B.8: Influence of mass flux at p_{wf}=1.05·p$_c$ and $\dot{q}_{wf}$=18 kW/m^2

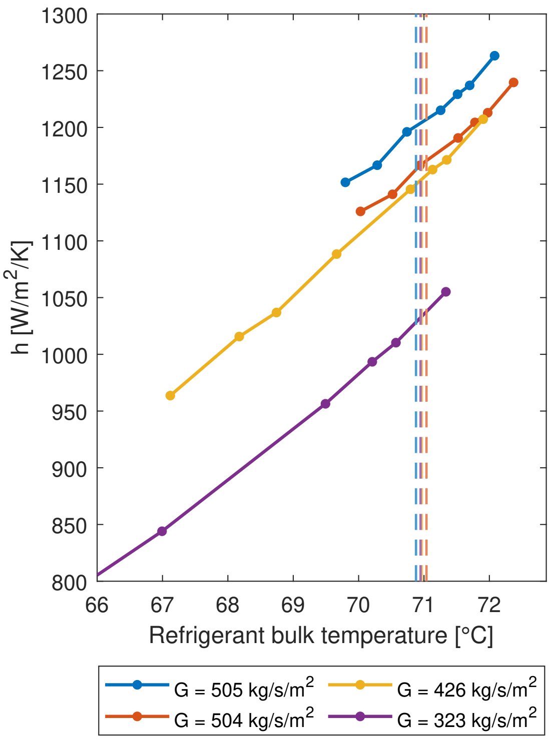

Figure B.9: Influence of mass flux at p_{wf}=1.10·p$_c$ and $\dot{q}_{wf}$=18 kW/m^2

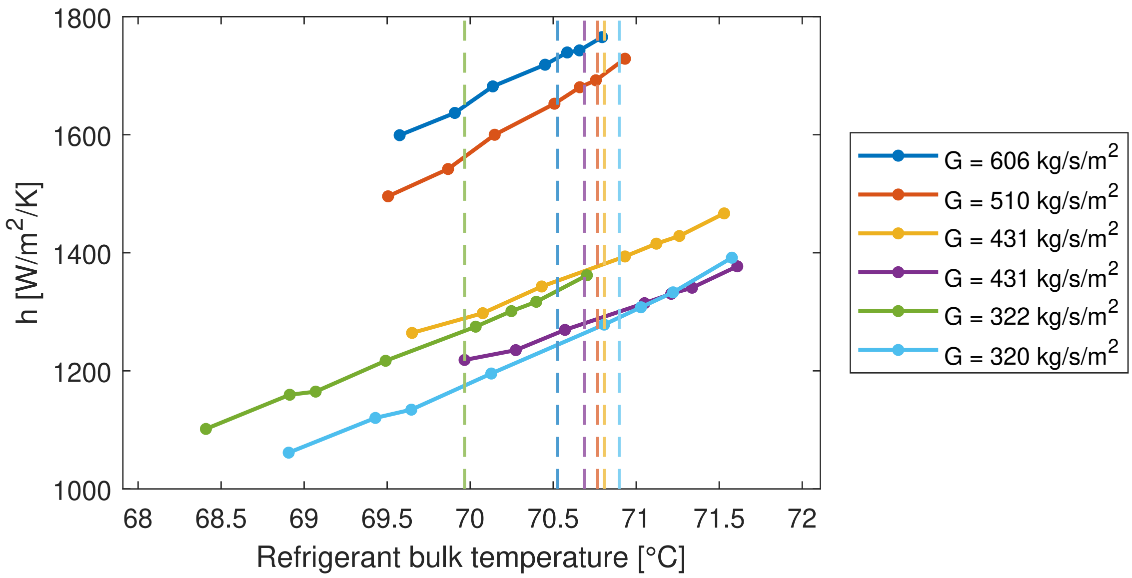

Figure B.10: Influence of mass flux at p_{wf}=1.10·p$_c$ and $\dot{q}_{wf}$=10 kW/m^2

B.3 Influence of heat flux

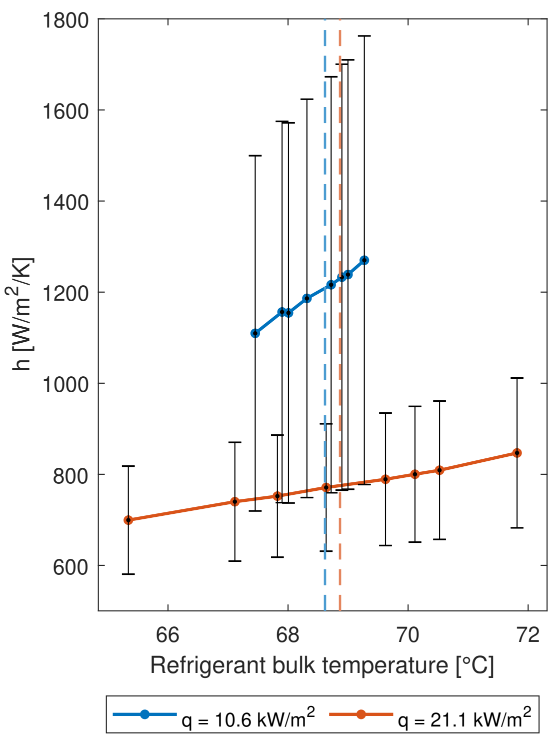

Figure B.11: Influence of heat flux at p_{wf}=1.05·p$_c$ and G_{wf}=320 kg/s/m^2

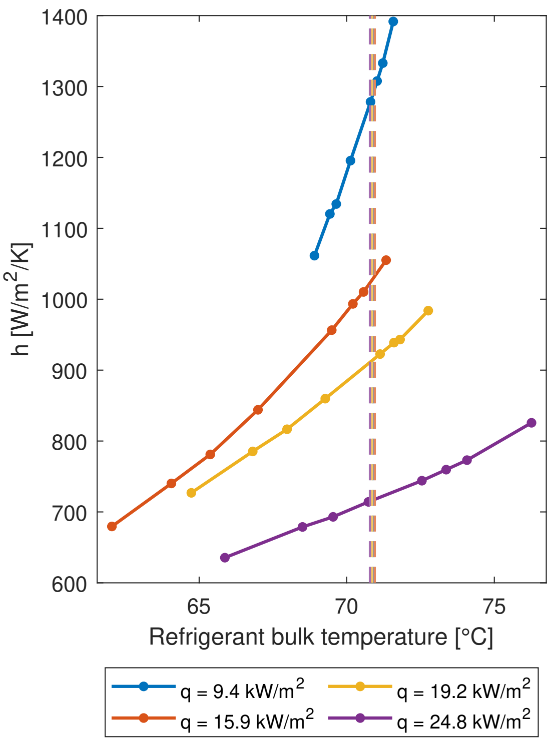

Figure B.12: Influence of heat flux at p_{wf}=1.10·p$_c$ and G_{wf}=320 kg/s/m^2

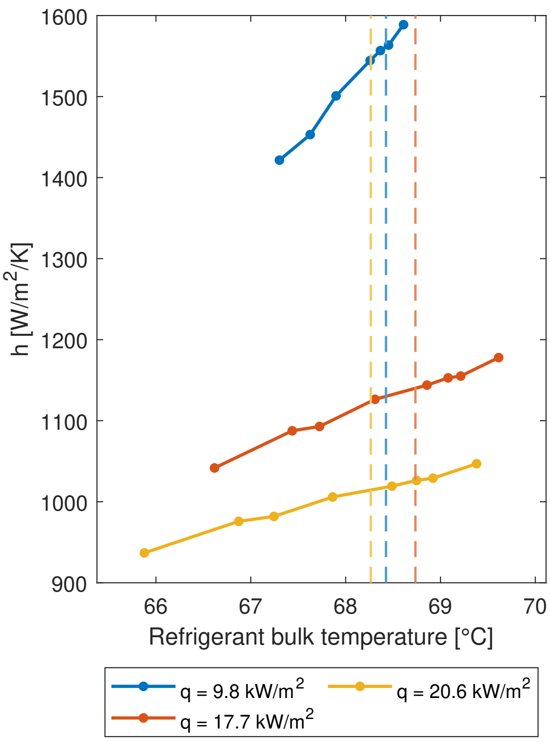

Figure B.13: Influence of heat flux at p_{wf}=1.05·p_c and G_{wf}=430 kg/s/m^2

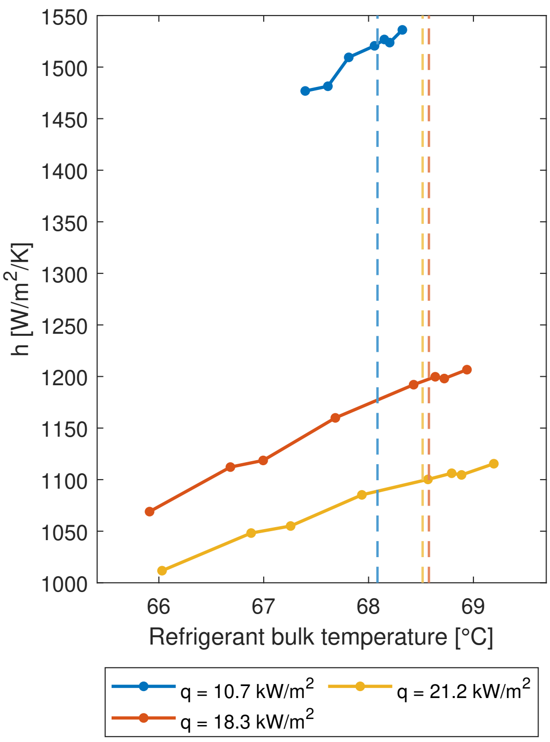

Figure B.14: Influence of heat flux at p_{wf}=1.05·p_c and G_{wf}=510 kg/s/m^2

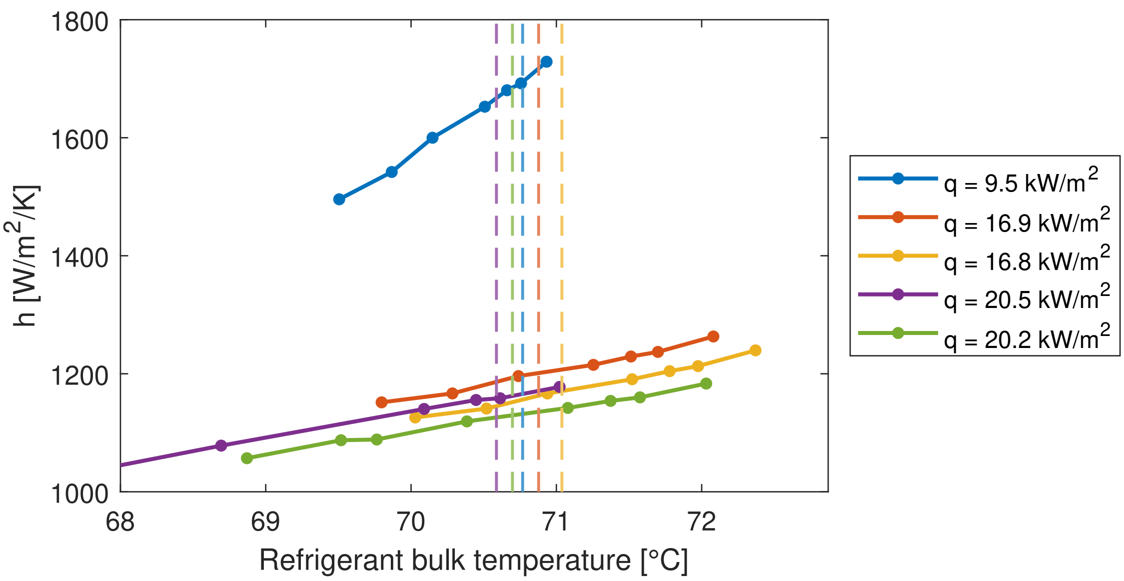

Figure B.15: Influence of heat flux at p_{wf}=1.10·p_c and G_{wf}=510 kg/s/m^2

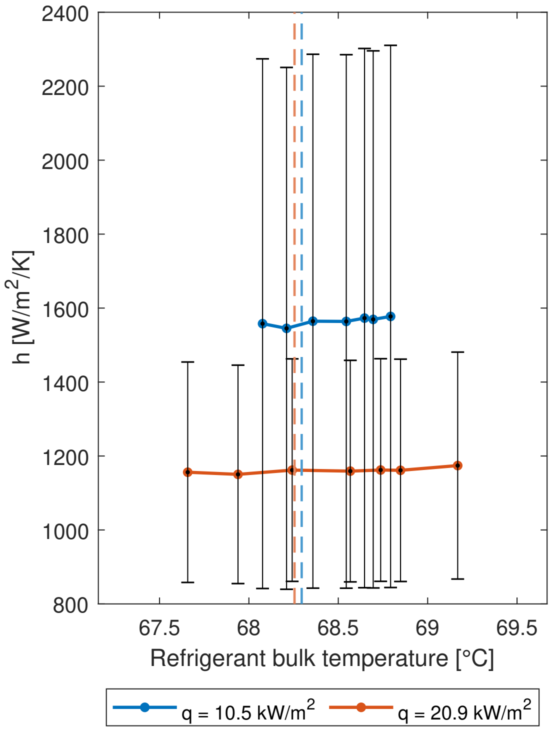

Figure B.16: Influence of heat flux at p_{wf}=1.05·p$_c$ and G_{wf}=600 kg/s/m^2

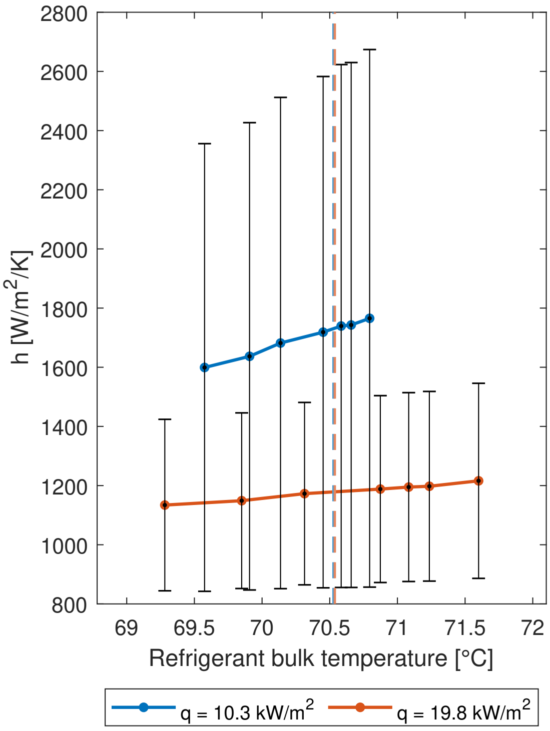

Figure B.17: Influence of heat flux at p_{wf}=1.10·p$_c$ and G_{wf}=600 kg/s/m^2

Appendix C

Experimental data

Table C.1 shows all performed measurements. For each measurement, the refrigerant mass flux G_{wf}, heat flux $\dot{q}_{wf}$ and refrigerant pressure p_{wf} are given. In addition, the used parameters for the expansion valve position (EV), electric preheater setpoint (EPH), number of preheaters used (PH), thermal oil inlet temperature setpoint ($\mathrm{T_{hf,in}}$) and pump frequency ($\mathrm{f_{pump}}$) are shown.

Table C.2 shows the measured bulk refrigerant temperatures $T_{wf,b}$ of all these measurements, the corresponding heat transfer coefficients h_{wf} and the uncertainties δh_{wf}.

Table C.1: Overview of performed measurements

Nr	G_{wf} [kg/s/m^2]	$\dot{q}_{wf}$ [kW/m^2]	p_{wf} [$\cdot p_c$]	EV [%]	EPH [°C]	PH [-]	$T_{\mathrm{hf,in}}$ [°C]	f_{pump} [Hz]
1.1	321	24.78	1.11	35	65	/	125	11
1.2	651	33.72	1.11	43	70	/	125	25
2.1	323	15.93	1.11	35	/	1x	100	11
2.2	510	18.26	1.06	46	65	1x	100	18
2.3	504	16.43	1.11	45	68	1x	100	18
3.1	327	21.13	1.06	36	/	1x	114.5	11
3.2	512	21.16	1.06	43	67	1x	107	18
3.3	326	10.58	1.06	36	/	2x	87	11
3.4	506	20.21	1.11	41	67	1x	106	18
4.1	326	9.86	1.09	38	/	2x	87	11
4.3	327	19.25	1.11	37	/	1x	108	11
4.4	510	9.53	1.11	44	71	1x	85	18
4.5	510	10.72	1.05	47	70	2x	85	18
5.1	320	9.43	1.11	37	/	2x	87	11
5.2	322	9.85	1.09	38	/	2x	87	11
5.3	506	21.51	1.05	45	70	1x	106	18
5.4	504	20.52	1.10	43	70	1x	106.5	18
5.5	426	20.58	1.05	43	70	1x	106	15
5.6	426	20.66	1.10	41	70	1x	108	15
5.7	430	9.77	1.05	43	70	2x	84	15
6.1	426	8.42	1.05	34	/	2x	79	15
6.2	426	8.21	1.06	34	/	2x	79	15
6.3	426	17.89	1.11	37	66	1x	102	15
6.4	426	17.69	1.06	40	66	1x	100	15
6.5	425	17.92	1.04	41	66	1x	100	15
7.1	433	9.71	1.05	45	66	2x	84	15
7.2	431	11.25	1.10	43	67	2x	91	15
7.3	431	10.64	1.11	43	67	2x	89	15
7.4	606	10.26	1.10	48	67	2x	86	22
7.5	602	9.69	1.05	55	67	2x	84	22
7.6	593	19.81	1.10	49	66	1x	105	22
7.7	592	20.95	1.05	53	66	1x	105	22
7.8	602	10.94	1.06	51	66	2x	85	22
7.9	599	10.52	1.05	55	67	2x	85	22
7.10	599	10.52	1.05	53	67	2x	85	22
7.11	588	20.40	1.05	57	66	1x	105	22
8.1	326	21.05	1.05	38	/	1x	112	11
8.2	325	20.80	1.11	36	/	1x	112	11
8.3	325	20.76	1.11	36	/	1x	113	11
8.4	431	11.13	1.11	39	68	2x	89	15
8.5	431	11.14	1.11	43	68	2x	89	15
8.6	506	16.56	1.12	42	68	1x	100	18
8.7	505	16.93	1.11	43	68	1x	100	18
8.8	431	10.94	1.11	43	68	2x	89	15
8.9	504	16.79	1.11	43	68	1x	100	18

Table C.2: Results of data reduction

1.1	$T_{wf,b}$	65.9	68.5	69.5	70.7	72.5	73.4	74.1	76.3	°C
	h_{wf}	636	679	693	714	744	760	773	826	W/m^2/K
	δh_{wf}	92	103	106	112	120	125	128	144	W/m^2/K
1.2	$T_{wf,b}$	59.8	62.3	63.1	65.4	69.1	70.1	70.5	71.0	°C
	h_{wf}	893	951	964	1024	1135	1165	1174	1188	W/m^2/K
	δh_{wf}	154	174	178	200	243	256	259	265	W/m^2/K
2.1	$T_{wf,b}$	62.0	64.1	65.4	67.0	69.5	70.2	70.6	71.3	°C
	h_{wf}	680	740	781	844	956	993	1010	1055	W/m^2/K
	δh_{wf}	134	154	169	192	238	254	261,9	283	W/m^2/K
2.2	$T_{wf,b}$	65.9	66.7	67.0	67.7	68.4	68.6	68.7	68.9	°C
	h_{wf}	1069	1112	1119	1160	1192	1200	1198	1207	W/m^2/K
	δh_{wf}	277	297	301	321	338	342	341	346	W/m^2/K
2.3	$T_{wf,b}$	69.8	70.2	70.2	70.7	71.2	71.4	71.6	72.0	°C
	h_{wf}	1079	1103	1092	1120	1136	1148	1153	1176	W/m^2/K
	δh_{wf}	291	302	297	311	319	325	328	340	W/m^2/K
3.1	$T_{wf,b}$	65.3	67.1	67.8	68.6	69.6	70.1	70.5	71.8	°C
	h_{wf}	699	740	752	771	789	800	809	847	W/m^2/K
	δh_{wf}	119	130	134	140	146	149	152	164	W/m^2/K
3.2	$T_{wf,b}$	66.0	66.9	67.3	67.9	68.6	68.8	68.9	69.2	°C
	h_{wf}	1012	1048	1055	1085	1100	1106	1105	1115	W/m^2/K
	δh_{wf}	232	248	251	264	271	274	273	278	W/m^2/K
3.3	$T_{wf,b}$	67.5	67.9	68.0	68.3	68.7	68.9	69.0	69.3	°C
	h_{wf}	1110	1156	1154	1186	1216	1233	1239	1270	W/m^2/K
	δh_{wf}	390	419	417	437	457	468	471	493	W/m^2/K
3.4	$T_{wf,b}$	68.9	69.5	69.8	70.4	71.1	71.4	71.6	72.0	°C
	h_{wf}	1057	1087	1089	1119	1142	1154	1160	1183	W/m^2/K
	δh_{wf}	252	265	265	279	290	295	298	309	W/m^2/K
4.1	$T_{wf,b}$	68.1	68.7	68.9	69.4	70.0	70.2	70.3	70.7	°C
	h_{wf}	1038	1094	1105	1158	1220	1244	1259	1304	W/m^2/K
	δh_{wf}	362	396	402	436	477	494	504	536	W/m^2/K
4.3	$T_{wf,b}$	64.7	66.8	68.0	69.3	71.1	71.6	71.8	72.8	°C
	h_{wf}	727	785	817	860	923	939	943	984	W/m^2/K
	δh_{wf}	134	152	163	178	201	208	209	226	W/m^2/K
4.4	$T_{wf,b}$	69.5	69.9	70.1	70.5	70.7	70.8	70.9		°C
	h_{wf}	1496	1542	1600	1653	1680	1692	1729		W/m^2/K
	δh_{wf}	697	736	787	835	861	873	908		W/m^2/K
4.5	$T_{wf,b}$	67.4	67.6	67.8	68.1	68.2	68.2	68.3		°C
	h_{wf}	1477	1481	1509	1521	1527	1524	1536		W/m^2/K
	δh_{wf}	644	648	670	680	685	682	693		W/m^2/K
5.1	$T_{wf,b}$	68.9	69.4	69.6	70.1	70.8	71.0	71.2	71.6	°C
	h_{wf}	1061	1120	1134	1195	1278	1308	1333	1392	W/m^2/K
	δh_{wf}	387	423	432	473	531	552	571	616	W/m^2/K
5.2	$T_{wf,b}$	68.4	68.9	69.1	69.5	70.0	70.2	70.4	70.7	°C
	h_{wf}	1102	1160	1165	1217	1275	1301	1317	1362	W/m^2/K
	δh_{wf}	401	438	441	476	516	535	547	580	W/m^2/K
5.3	$T_{wf,b}$	64.9	65.9	66.5	67.4	68.3	68.5	68.6	68.9	°C
	h_{wf}	1019	1063	1079	1122	1152	1159	1157	1166	W/m^2/K
	δh_{wf}	236	255	263	282	297	300	299	304	W/m^2/K

5.4	$T_{wf,b}$	65.9	67.0	67.6	68.7	70.1	70.4	70.6	71.0	°C
	h_{wf}	959	1006	1025	1078	1140	1156	1159	1178	W/m^2/K
	δh_{wf}	214	234	242	265	294	301	303	312	W/m^2/K
5.5	$T_{wf,b}$	65.9	66.9	67.2	67.9	68.5	68.7	68.9	69.4	°C
	h_{wf}	937	976	982	1006	1019	1026	1029	1047	W/m^2/K
	δh_{wf}	204	220	222	232	238	241	242	250	W/m^2/K
5.6	$T_{wf,b}$	66.4	67.7	68.4	69.4	70.5	70.8	71.0	71.7	°C
	h_{wf}	887	934	953	995	1032	1043	1048	1076	W/m^2/K
	δh_{wf}	184	201	209	226	241	246	248	260	W/m^2/K
5.7	$T_{wf,b}$	67.3	67.6	67.9	68.3	68.4	68.5	68.6		°C
	h_{wf}	1422	1453	1501	1544	1557	1563	1589		W/m^2/K
	δh_{wf}	632	657	697	734	745	751	773		W/m^2/K
6.1	$T_{wf,b}$	60.7	61.6	61.9	62.8	64.1	64.6	64.9	65.6	°C
	h_{wf}	837	922	942	1032	1216	1290	1350	1503	W/m^2/K
	δh_{wf}	290	338	349	406	537	595	644	780	W/m^2/K
6.2	$T_{wf,b}$	60.6	61.6	61.9	62.7	64.1	64.6	64.9	65.6	°C
	h_{wf}	807	891	910	995	1172	1242	1304	1448	W/m^2/K
	δh_{wf}	278	325	336	388	511	565	616	741	W/m^2/K
6.3	$T_{wf,b}$	67.1	68.2	68.7	69.7	70.8	71.1	71.3	71.9	°C
	h_{wf}	964	1016	1037	1088	1146	1163	1171	1207	W/m^2/K
	δh_{wf}	228	251	260	284	312	320	325	343	W/m^2/K
6.4	$T_{wf,b}$	66.6	67.4	67.7	68.3	68.9	69.1	69.2	69.6	°C
	h_{wf}	1042	1088	1093	1126	1144	1153	1155	1178	W/m^2/K
	δh_{wf}	266	287	290	306	315	319	320	332	W/m^2/K
6.5	$T_{wf,b}$	66.6	67.2	67.4	67.7	68.2	68.4	68.5	68.8	°C
	h_{wf}	1044	1075	1070	1087	1095	1102	1102	1120	W/m^2/K
	δh_{wf}	265	280	277	285	289	292	293	301	W/m^2/K
7.1	$T_{wf,b}$	68.0	68.2	68.3	68.6	68.7	68.8	68.9		°C
	h_{wf}	1456	1449	1475	1503	1504	1506	1529		W/m^2/K
	δh_{wf}	661	655	677	700	701	703	723		W/m^2/K
7.2	$T_{wf,b}$	70.1	70.4	70.6	71.2	71.3	71.4	71.7		°C
	h_{wf}	1148	1157	1185	1224	1236	1244	1278		W/m^2/K
	δh_{wf}	392	398	415	439	446	452	474		W/m^2/K
7.3	$T_{wf,b}$	70.0	70.3	70.6	71.1	71.2	71.3	71.6		°C
	h_{wf}	1218	1235	1269	1315	1331	1341	1377		W/m^2/K
	δh_{wf}	450	461	484	515	526	534	560		W/m^2/K
7.4	$T_{wf,b}$	69.6	69.9	70.1	70.5	70.6	70.7	70.8		°C
	h_{wf}	1599	1637	1682	1719	1739	1743	1765		W/m^2/K
	δh_{wf}	757	790	830	864	884	887	909		W/m^2/K
7.5	$T_{wf,b}$	68.4	68.6	68.7	68.9	69.0	69.1	69.2		°C
	h_{wf}	1572	1562	1583	1590	1604	1602	1614		W/m^2/K
	δh_{wf}	760	751	771	776	789	788	798		W/m^2/K
7.6	$T_{wf,b}$	69.3	69.8	70.3	70.9	71.1	71.2	71.6		°C
	h_{wf}	1134	1149	1173	1188	1195	1198	1216		W/m^2/K
	δh_{wf}	290	297	308	316	319	321	330		W/m^2/K
7.7	$T_{wf,b}$	67.7	67.9	68.2	68.6	68.7	68.8	69.2		°C
	h_{wf}	1156	1150	1162	1159	1162	1161	1174		W/m^2/K
	δh_{wf}	298	295	301	300	301	301	307		W/m^2/K

7.8	$T_{wf,b}$	67,5	67,8	68,0	68,2	68,3	68,4	68,5	°C
	h_{wf}	1594	1618	1651	1660	1672	1668	1677	W/m^2/K
	δh_{wf}	734	755	784	792	802	799	807	W/m^2/K
7.9	$T_{wf,b}$	68,1	68,2	68,4	68,5	68,6	68,7	68,8	°C
	h_{wf}	1558	1545	1565	1564	1573	1569	1577	W/m^2/K
	δh_{wf}	716	706	722	721	729	726	733	W/m^2/K
7.10	$T_{wf,b}$	68,2	68,3	68,5	68,6	68,7	68,8	68,9	°C
	h_{wf}	1579	1568	1589	1590	1600	1595	1603	W/m^2/K
	δh_{wf}	734	725	743	744	753	749	755	W/m^2/K
7.11	$T_{wf,b}$	68,4	68,6	68,9	69,4	69,7	69,9	70,5	°C
	h_{wf}	1139	1132	1145	1153	1163	1170	1201	W/m^2/K
	δh_{wf}	291	288	294	298	303	306	321	W/m^2/K
8.1	$T_{wf,b}$	64,3	67,0	67,8	68,6	69,1	69,4	70,4	°C
	h_{wf}	726	789	812	826	836	843	875	W/m^2/K
	δh_{wf}	126	146	153	158	161	163	174	W/m^2/K
8.2	$T_{wf,b}$	66,2	69,1	70,2	71,7	72,2	72,6	73,7	°C
	h_{wf}	749	824	857	900	917	925	971	W/m^2/K
	δh_{wf}	133	157	169	184	190	193	210	W/m^2/K
8.3	$T_{wf,b}$	66,5	69,3	70,4	72,0	72,5	72,9	74,1	°C
	h_{wf}	736	807	839	881	898	907	954	W/m^2/K
	δh_{wf}	129	152	162	177	183	186	203	W/m^2/K
8.4	$T_{wf,b}$	69,6	70,0	70,4	70,9	71,1	71,2	71,5	°C
	h_{wf}	1269	1302	1347	1399	1421	1434	1472	W/m^2/K
	δh_{wf}	473	495	526	563	579	588	617	W/m^2/K
8.5	$T_{wf,b}$	69,6	70,1	70,4	70,9	71,1	71,3	71,5	°C
	h_{wf}	1264	1298	1343	1394	1415	1428	1467	W/m^2/K
	δh_{wf}	469	491	522	558	574	584	613	W/m^2/K
8.6	$T_{wf,b}$	69,8	70,4	71,0	71,6	71,8	72,0	72,4	°C
	h_{wf}	1105	1130	1164	1189	1204	1211	1235	W/m^2/K
	δh_{wf}	299	311	328	341	349	353	366	W/m^2/K
8.7	$T_{wf,b}$	69,8	70,3	70,7	71,3	71,5	71,7	72,1	°C
	h_{wf}	1152	1167	1196	1215	1229	1237	1263	W/m^2/K
	δh_{wf}	319	327	342	352	360	364	378	W/m^2/K
8.8	$T_{wf,b}$	69,7	70,1	70,4	70,9	71,1	71,2	71,5	°C
	h_{wf}	1255	1286	1329	1379	1401	1414	1451	W/m^2/K
	δh_{wf}	468	488	518	553	569	578	606	W/m^2/K
8.9	$T_{wf,b}$	70,0	70,5	70,9	71,5	71,8	72,0	72,4	°C
	h_{wf}	1126	1141	1167	1191	1204	1213	1240	W/m^2/K
	δh_{wf}	307	315	327	340	347	352	366	W/m^2/K